12-2015

Epitaxial Growth of Si-Ge-Sn Alloys for Optoelectronic Device Application

Aboozar Mosleh
University of Arkansas, Fayetteville

Epitaxial Growth of Si-Ge-Sn Alloys for Optoelectronic Device Applications

A dissertation submitted in partial fulfillment
of the requirements for the degree of
Doctor of Philosophy in Microelectronics-Photonics

by

Aboozar Mosleh
University of Isfahan
Bachelor of Science in Physics, 2004
Shahid Bahonar University of Kerman
Master of Science in Photonics, 2008
University of Arkansas
Master of Science in Electrical Engineering, 2015

December 2015
University of Arkansas

This dissertation is approved for recommendation to the Graduate Council.

Dr. Hameed A. Naseem Dissertation Director	Dr. Shui-Qing Yu Committee Member
Dr. Simon S. Ang Committee Member	Dr. Gregory J. Salamo Committee Member
Dr. Rick Wise Ex-Officio Member	

The following signatories attest that all software used in this dissertation was legally licensed for use by Aboozar Mosleh for research purposes and publication.

_____	_____
Aboozar Mosleh, Student	Dr. Hameed A. Naseem, Dissertation Director

This dissertation was submitted to http://www.turnitin.com for plagiarism review by the TurnItIn company's software. The signatories have examined the report on this dissertation that was returned by TurnItIn and attest that, in their opinion, the items highlighted by the software are incidental to common usage and are not plagiarized material.

_____	_____
Dr. Rick Wise, Program Director	Dr. Hameed A. Naseem, Dissertation Director

Abstract

Microelectronics industry has experienced a tremendous change over the last few decades and has shown that Moore's law has been followed by doubling the number of transistors on the chip every 18 months. However, continuous scaling down of the transistors size is reaching the physical limits and data transfer through metal interconnects will not be able to catch up with the increasing data processing speed in the future. Therefore, optical data transfer between chips and on-chip has been widely investigated. Silicon based optoelectronics has received phenomenal attention since Si has been the core material on which microelectronic industry has been built. However, due to the indirect bandgap nature of Si, its optical characteristics fall short compared to similar III-IV semiconductors. The efforts in III-V incorporation on Si substrate have not been successful due to the incompatibility of the growth with complementary metal oxide semiconductor processing. Germanium has been studied in order to develop a Si compatible technology and it has been shown that a direct bandgap material is achievable by alloying Sn in Ge. Further investigations on Si-Ge-Sn material system showed its viability as a technology that can be used for fabrication of Si-compatible light source and detectors.

The work presented in this dissertation is focused on the low temperature growth of Si-Ge-Sn alloys. High quality crystalline homoepitaxial silicon films were deposited at 250 °C using a plasma-enhanced chemical vapor deposition (PECVD) system. Strain-relaxed Ge and SiGe films were also grown on Si substrate at 350-550 °C in a reduced pressure CVD system. Commercial precursors of silane and germane were used to grow the films at different chamber pressures. Germanium-tin and silicon-germanium-tin alloys were grown by a cold-wall chemical vapor deposition system at low temperatures (300-450 °C) directly on Si substrates.

Two different delivery systems were adopted for the delivery of stannic chloride and deuterated stannane as Sn precursors along with silane and germane. Crystallinity and growth quality of the films were investigated through material characterization methods including X-ray diffraction, scanning electron microscopy and transmission electron microscopy. Elemental characterization of the films was done using Rutherford backscattering measurement and energy-dispersive X-ray spectroscopy. Moreover, optical characterizations were performed using Raman spectroscopy and photoluminescence on the samples to investigate Sn incorporation in the films.

Additionally, compressively strained (<1%) GeSn films on Ge buffer layers that were grown using a commercial CVD reactor were studied. Material and optical characterization was performed on the films to investigate the film quality and Sn incorporation. Investigation of the defects at the GeSn/Ge interface showed formation of symmetrical and asymmetrical Lomer misfit dislocations which stops propagation of defects parallel to the growth direction. Cyclic annealing of the samples showed strain relaxation and enhancement of the quality of the films.

Acknowledgements

Firstly, I would like to express my sincere gratitude to my advisor, Dr. Hameed Naseem, for the continuous support of my Ph.D. study, for his patience, motivation, and immense knowledge. His guidance helped me in the research and writing of this dissertation. I could not have imagined having a better advisor and mentor for my Ph.D. study. His advice on research as well as on my life has been priceless. My gratitude extends to Dr. Fisher Yu for his support and guidance that was also available to me at all times. I would like to thank him for encouraging my research and for allowing me to grow as a research scientist.

I would like to thank the rest of my dissertation committee: Dr. Greg Salamo, Dr. Simon Ang, and Dr. Rick Wise, for serving as my committee members and for their insightful comments and encouragement. My sincere thank goes to Prof. Ken Vickers who provided me an opportunity to join microEP and for all the lessons I learned from him on how to have leadership in research. Without his precious support and advice it would not be possible to make so much progress in my academic career.

I want to express my deep appreciation to Dr. Murtadha Alher for his priceless help in the lab work and the sleepless nights we were working together before deadlines, and for all the fun we have had in the last three years. I would like to acknowledge Dr. Wei Du for his great help in reviewing my papers and insightful comments. I also want to acknowledge the University of Arkansas Institute for Nanoscience and Engineering for material characterization of the samples and thank Dr. Mourad Benamara for being so helpful especially with the TEM.

I would like to thank Dr. Husam Abusafe for his help to get me started in the lab work and his continuous help during my research. I would like to thank Dr. Zafar Waqar, Mike

Steger, Ben Conley, Larry Cousar and other labmates who helped in building the UHV-PECVD system and running the experiments. My special thanks extend to Seyed Amir Ghetmiri and Sattarr Al-Kabi for being such great and helpful friends and all other labmates in the characterization lab who helped me characterizing my samples.

Chapter 3, 4, 5, 6 and 7 are largely reproduced from publications in the Electrochemical Society transaction papers, Journal of Frontiers in Materials, Journal of Electronic Materials, and IEEE Photonics Society Summer Topical proceedings.

Parts of Chapter 3 were originally published as:

1) "Investigation of Growth Mechanism and Role of H_2 in Very Low Temperature Si Epitaxy," A. Mosleh, S. A. Ghetmiri, B. R. Conley, H. Abu-safe, M. Benamara, Z. Waqar, S.-Q. Yu, H. A. Naseem, ECS Transactions, 64 (6), 967-975, 2014.

2) "CMOS Compatible Growth of High Quality Ge, SiGe and SiGeSn for Photonic Device Applications," M. Alher, A. Mosleh, L. Cousar, W. Dou, P. C. Grant, S.A. Ghetmiri, S. Al-Kabi, W. Du, M. Benamara, B. Li, M. Mortazavi, S.-Q. Yu, H. A. Naseem, ECS Transactions, 2015. (in press)

Parts of Chapter 4 were originally published or submitted to be published as:

1) "Direct growth of $Ge_{1-x}Sn_x$ films on Si using a cold-wall ultra-high vacuum chemical vapor deposition system," A. Mosleh, M. A. Alher, L. Cousar, W. Du, S.A. Ghetmiri, T. Pham, G. Sun, R.A. Soref, B. Li, , H.A. Naseem, S. Yu, , Frontiers in Materials, 2, 30, 2015.

2) "$Si_yGe_{1-x-y}Sn_x$ films grown on Si using a cold-wall ultra-high-vacuum chemical-vapor-deposition system," A. Mosleh, M. Alher, W. Du, L. C. Cousar, S. A. Ghetmiri, S. Al-Kabi, W. Dou, P. C. Grant, G. Sun, R. A. Soref, B. Li, H. A. Naseem, S.-Q. Yu, submitted to Journal of Vacuum Science and Technology B, 2015.

3) "Enhancement of Material Quality of (Si)GeSn Films Grown By $SnCl_4$ Precursor," A. Mosleh, M. Alher, L. Cousar, H. Abu-safe, W. Dou, P. C. Grant, S. Al-Kabi, S.A. Ghetmiri, B. Alharthi, H. Tran, W. Du, M. Benamara, B. Lid, M. Mortazavi, S.-Q. Yu, H. Naseem, ECS Transactions, 2015. (in press)

Part of Chapter 5 has been submitted to be published as:

4) "Buffer-free GeSn and SiGeSn growth on Si substrate using in-situ SnD_4 gas mixing," A. Mosleh, M. Alher, W. Du, L. C. Cousar, S. A. Ghetmiri, S. Al-Kabi, W. Dou, P. C. Grant,

G. Sun, R. A. Soref, B. Li, H. A. Naseem, S.-Q. Yu, submitted to Journal of Electronic Materials, 2015.

Parts of Chapter 6 were originally published as:

1) "Material characterization of $Ge_{1-x}Sn_x$ alloys using a commercial CVD system for Optoelectronic Device Applications," A. Mosleh, S. A. Ghetmiri, B. R. Conley, M. Hawkridge, M. Benamara, A. Nazzal, J. Tolle, S.-Q. (Fisher) Yu, H. A. Naseem, Conference on Lasers and electro-optics, J. Electronic Materials, 43.4 (2014): 938-946.

2) "Investigation on Formation and Propagation of Defects in Ge_{1-x} Sn_x Thin Films," A. Mosleh, M. Benamara, S. A. Ghetmiri, B. R. Conley, M. A. Alher, W. Du, G. Sun, R. A. Soref, J. Margetis, J. Tolle, S.-Q. Yu, and H. A. Naseem, ECS Transactions. 64, 895-901, 2014.

3) "Strain Relaxation and Material Quality Improvement of Compressively Strained GeSn Epitaxial Films through a Cyclic Rapid Thermal Annealing Process,"A. Mosleh, S. A. Ghetmiri, B. R. Conley, W. Du; S.-Q. Yu, H. A. Naseem, R. A. Soref, G. Sun, J. Tolle, J. Margetis, Photonics Society Summer Topical Meeting Series, 2014 IEEE , vol., no., pp.221,222, 14-16 July 2014.

Part of Appendix G was originally published as:

"Nucleation-step study of silicon homoepitaxy for low-temperature fabrication of solar cells," A. Mosleh, Z. Waqar, S.-Q. (Fisher) Yu, H. Abu-safe, S. A. Ghetmiri, B. R. Conley, M. Benamara, H. A. Naseem, Photovoltaic Specialists Conference (PVSC), pp.2646,2650, 16-21 June 2013.

This work was funded in part by the National Science Foundation award# EPS-1003970. Research possible through the use of the High Density Electronics Center at the University of Arkansas. Additionally, I would like to thank ASM America Inc. for the collaboration in accomplishment of this research by producing GeSn samples with their CVD reactors.

Last but not the least, I would like to thank my family: my parents, my brother, Iman and my sisters, Somayyeh and Leila, for supporting me spiritually throughout writing this dissertation and my life in general. Your prayer for me was what sustained me thus far. At the end I would like express appreciation to my beloved wife, Fahimeh, who spent sleepless nights

with me and was always my support in the moments when there was no one to answer my queries. I would like to thank my son, Eliyah, who was always considerate about me being busy with my work despite his young age.

Dedication

To my parents, my wife, and my son.

آنانکه محیط فضل و آداب شدند　　در جمع علوم شمع اصحاب شدند

ره زین شب تاریک نبردند بروز　　گفتند فسانه ای و در خواب شدند

حکیم عمر خیام

Scientists are like the candles of the way,

They light the path for the travelers on the way,

Yet, could never light the night like a day,

They just tell a story and pass away.

Omar Khayyam

The great Persian scientist, philosopher and poet,

(AD 1048 –1131)

Table of Contents

List of Figures

List of Tables

Chapter 1. Introduction

1.1. Motivation

Integrated circuit (IC) technology has been based on silicon due to its exceptional material characteristics such as abundance on the earth (low cost), capability to be easily doped (high electron/hole mobility), high oxide quality (suitable for IC fabrication processes). Although there are other materials available to compete with Si in one or two of the mentioned properties, no material has been able to compete in all aspects. Therefore, Si technology has been adopted by industry for fabrication of microelectronic devices since 1970s. The number of transistors on the chip has doubled every 1.5 years as predicted by Moore reaching the current minimum feature size of 14 nm by Intel®. Scaling down the transistors allows higher data processing speed while the delay (RC) for data transfer on the chip does not decrease at the same rate. If the number of transistors on a chip doubles, the length of the top most metallic interconnects stays the same which causes the delay in data transfer rate to stay the same while the data processing speed has doubled [1-3]. In addition, optical interconnects are able to transfer more data through modulation of different sets of data. This causes reduction in number of required wire connections. Therefore, changing the chip interconnects from electrical to optical could be an approach to keep Moore's law on the path.

The main advantages in using optical interconnects are: extremely low loss for data transfer over long distances, low operation power [4] and easy clock and signal timing [5]. However, a complete set of photonic devices is needed in order to bring data communication on the chip. These devices are light emitters [6-8], amplifiers, modulators, couplers, waveguides, switches and photodetectors. Aside from the optical interconnects, Si optoelectronics provides

a variety of applications for production of cheap sensors and detectors for medical imaging and gas sensing.

Indirect bandgap of Si, Ge, and their alloys have led researchers to take different approaches to monolithically grow these devices on Si such as: growth of direct bandgap III-V materials on Si [9], Ge bandgap engineering through strained growth or heavy n-doping [10], and doping Si with rare earth elements [11]. The main challenge of these methods is incompatibility of growth to complementary metal oxide semiconductor (CMOS) processing. For the growth of highly strained Ge on Si, high temperatures are needed to attain tensile strain; and, for the growth of III-Vs on Si, the possibility of auto-doping of the materials increases the complexity of such incorporation to Si technology. Therefore, development of a Si-compatible optoelectronic system that could utilize the infrastructures of Si technology is highly demanded.

1.2. Silicon-germanium-tin technology

Si photonics has taken a different route since all group IV materials have been investigated for achieving direct bandgap material. Crystallizing in diamond structure and having a wide range of band gaps from 5.4 eV in diamond to -0.41 eV for semi-metal α-Sn were promising for alloying and forming a variety of different bandgap materials. Silicon germanium alloys were widely explored for enhancing the electrical properties of Si but other alloys were not explored due to high lattice mismatch and low solid solubility. The theoretical calculations for achieving direct bandgap material in GeSn alloys date back to 1991 [12]; however, high quality GeSn alloys were not achieved until recently [8]. Adding Si makes the Si-Ge-Sn system unique in terms of tuning the lattice constant and bandgap engineering by varying the compositions of Si, Ge, and Sn. These remarkable theoretical and experimental findings have resulted in an increased interest in studying GeSn and SiGeSn materials by different groups

around the world. Figure 1 shows the trend of publications on GeSn and SiGeSn per year from 2000 to August 2015. The number of publications shows a sudden increase from 2005 and increases every year since 2008. Currently, the research is 65% on material studies and 35% on devices.

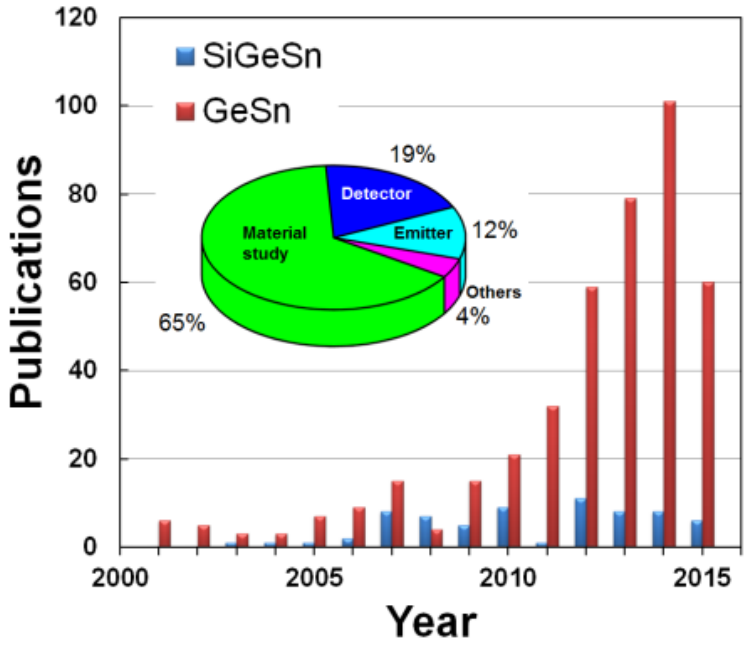

Figure 1. GeSn and SiGeSn publications from year 2000 to August 2015. The data is generated from Web of Science Thompson Reuters website.

1.2.1. Si-Ge-Sn band structure

Germanium is a pseudo-direct bandgap material with only 0.14 eV difference between conduction band edges at the L and Γ valleys at room temperature. Incorporation of Sn into Ge to form an alloy lowers the Γ band edge at a rate faster than that of the L decrease which results in an indirect-to-direct transition in the bandgap of the $Ge_{1-x}Sn_x$ alloys [13]. Since this cross-over is below 0.6 eV, the GeSn devices can only cover the mid-infrared range [14]. Addition of Si with a bandgap energy of 3.2 eV at its Γ valley would enable the GeSn technology to achieve higher bandgap energies. Such an increase in the ternary alloy bandgap enables fabrication of

photonic devices for a wider infrared range (0.8 eV - 1.1 eV) [15]. Figure 2 shows the schematic of the bandgap diagram of Si, Ge, and Sn and their alloys of GeSn and SiGeSn. The Γ bandgap edge is the direct transition while L and X depict the indirect transitions. It is illustrated that in GeSn, Sn incorporation in Ge lowers the Γ valley faster than the L one. Silicon-germanium alloy has a higher bandgap due to the incorporation of Si in Ge and it is still indirect bandgap as both Si and Ge are indirect band gap. Incorporation of Sn in SiGe decreases the band gap like GeSn to achieve direct bandgap at higher bandgap energies.

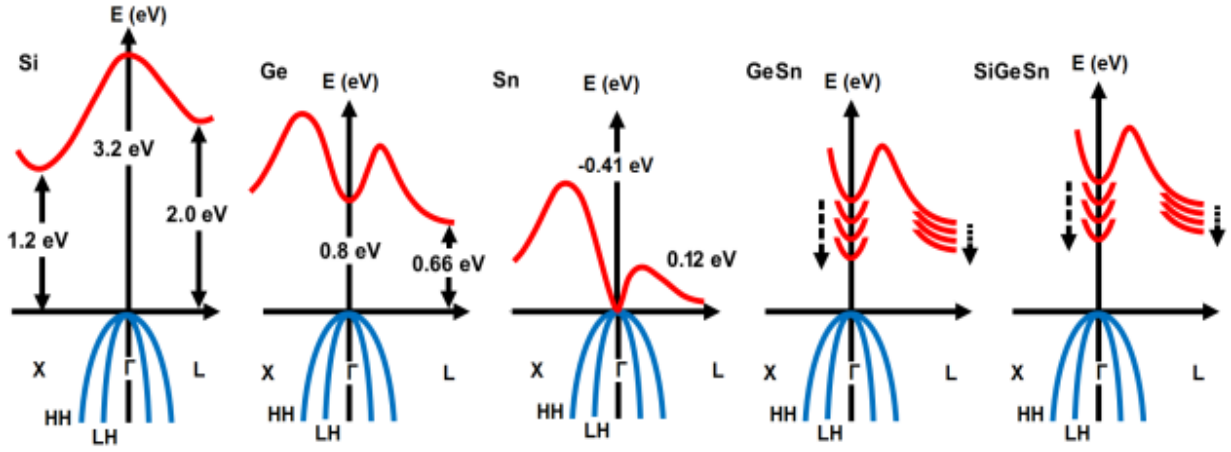

Figure 2. Schematics of electronic band structures of Si, Ge, Sn, GeSn and SiGeSn.

Bandgap calculations of GeSn and SiGeSn the bandgap for all highly symmetric points (Γ, L and X) could be achieved using the Vegard's law. Equation 1 shows the calculation of change in the Γ point energy as a function of Si, Ge, and Sn mole fraction (y, 1-x-y, x, respectively) in SiGeSn material:

$$E_{g\Gamma}^{Si_yGe_{1-x-y}Sn_x} = yE_{g\Gamma}^{Si} + (1\text{-}x\text{-}y)E_{g\Gamma}^{Ge} + x\,E_{g\Gamma}^{Sn} - y(1-x-y)b^{SiGe} - x(1-x-y)b^{GeSn} - xyb^{SiSn} \quad \text{(Equation 1)}$$

The bowing parameters of SiGe, GeSn and SiSn are taken as b^{SiGe}= 2.49 eV, b^{GeSn}= 0.21 eV nm and b^{SiSn}=3.915 eV, respectively [16]. Figure 3 (a) shows the change in the Γ and

L bandgap of GeSn and SiGeSn for different as a result of increase in the Sn incorporation. The bandgap calculation for the SiGeSn was done considering 10% Si in the lattice. Incorporation of Sn in Ge or SiGe changes the lattice size as well. Equation 2 shows Vegard's law for calculation of lattice constant depending on the different Si, Ge and Sn mole fractions and Figure 3b is the plot of the lattice constant vs. bandgap of the Si-Ge-Sn alloys.

$$a_0^{Si_yGe_{1-x-y}Sn_x} = y\, a_0^{\mathrm{Si}} + (1-x-y)a_0^{\mathrm{Ge}} + x\, a_0^{\mathrm{Sn}} - y(1-x-y)b^{SiGe} - x(1-x-y)b^{GeSn} - xyb^{SiSn} \quad \text{(Equation 2)}$$

Lattice constants of the elements are a_0^{Si}=5.431 Å, a_0^{Ge}=5.658 Å, and a_0^{Sn} =6.491 Å. The bowing parameters of SiGe, GeSn and SiSn are taken as b^{SiGe}= 0.026 nm, b^{GeSn}= 0.166 nm, and b^{SiSn} =0, respectively [16]. Engineering the bandgap and lattice constant could be used for the growth of lattice matched films with different energy gaps. Such GeSn/SiGeSn layers have been used for the design of double-heterostructure [17] and multiple quantum well [18] group IV laser diodes.

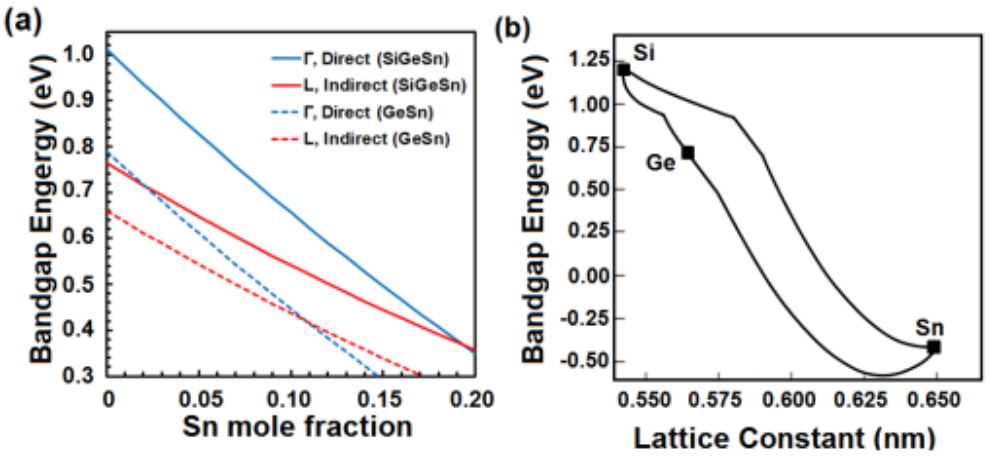

Figure 3. The change in the bandgap edge and lattice constant of Si-Ge-Sn alloys. (a) The change in the direct and indirect bandgap edge of GeSn and SiGeSn as a result of Sn incorporation. (b) Bandgap diagram of Si-Ge-Sn alloys vs. lattice constant.

1.2.2. Si-Ge-Sn growth technique

The main challenges in the growth of SiGeSn materials are the large lattice mismatch between Si, Ge, and α-Sn as well as low solid solubility of Sn in Si and Ge. The solid solubility limit of Sn in Ge is 0.5% at room temperature while that of Sn in Si is less than 0.5% [19]. Additionally, the diamond structure of Sn (α-Sn) is unstable above 13 °C and transforms into tetragonal structure (β-Sn). Because of low solid solubility and instability of α-Sn structure, Sn is apt to precipitate from the Ge or SiGe lattice during growth or thermal processing. Consequently, growth of Sn content alloys is only possible away from the thermal equilibrium conditions. Moreover, bond strength in germane (GeH_4) is approximately 20% weaker than that of silane (SiH_4) which results in lower growth temperature of GeSn alloys [20]. Therefore, growth of the GeSn alloy is not as challenging as SiGeSn growth because the GeSn films can be grown at lower temperatures which causes less Sn precipitation. Whereas, SiGeSn growth needs higher growth temperature to break Si-H bonds which promotes Sn precipitation from the lattice. Therefore, not only is the incorporation of Sn in Ge difficult but also it is even more difficult to incorporate Si at that low temperature.

Several methods of growth, such as molecular beam epitaxy (MBE) [21] , sputtering [22], solid phase epitaxy [23], recrystallization [24], and chemical vapor deposition (CVD), have been employed to grow GeSn [25]. The highest material quality is reported from molecular beam MBE [21] and CVD systems [26]. For the MBE method, both gas source and solid source MBE have been used by different groups to grow GeSn films [27-37] .

Kouvetakis' group at Arizona State University (ASU) has established a hot-wall ultra-high vacuum CVD method with great success in device fabrication [26]. In their reports of growing (Si)GeSn, higher order (di-, tri-, tetra-) silanes (Si_xH_{2x+2}: x= 2-4) and higher order (di-,

tri-, tetra-) germanes (Ge_xH_{2x+2}: x= 2-4) were used [38]. In addition, more compound hetero-nuclear Si-Ge molecules [$(H_3Ge)_xSiH_{4-x}$ or $H_3Si)_xGeH_{4-x}$: x=1-4] were used for the growths when both Si and Ge precursors were needed [25, 39]. The GeSn films were grown with or without a Ge buffer layer and SiGeSn films were grown either on Ge or GeSn buffer layers. Vincent *et al.,* [40] (from IMEC using atmospheric pressure CVD) and Kim *et al.,* [41] [from Applied Materials/Stanford University using reduced pressure CVD (RPCVD)] have reported successful growth of GeSn by digermane on a Ge buffered Si substrate. In the latest reports, Wirth *et al.* (from Peter Grünberg Institute in Germany) have grown (Si)GeSn films without a buffer layer on Si and Ge substrates using a RPCVD system with showerhead technology [42, 43]. They have used precursors of disilane and digermane for the growth of the films.

High quality GeSn and SiGeSn films grown at low temperatures of 250-400 °C have been reported; however, there are two main issues with using such gases. 1. Commercial and low cost production of these gases are not available and they are either in-situ produced or are purchased at higher costs. 2. Due to the instability of higher order gases such as digermane (Ge_2H_6) and their being explosive, they are diluted in a carrier gas (e.g. H_2, N_2, Ar). This causes the growth to be restricted to only one carrier gas. Additionally, due to safety considerations the amount of available gas could not exceed 15% or 154 grams in one bottle [44]. Therefore, researchers have tried using silane and germane rather than the higher order gases to reduce the safety risks and final product costs in order to commercialize the production of (Si)GeSn technology.

On the other hand, there have not been many options available for the Sn precursor and stannic chloride ($SnCl_4$) and deuterated stannane (SnD_4) have mostly been used for Sn incorporation. The main issue with $SnCl_4$ has been the etching behavior of the gas byproducts

especially when a p-doped film is being deposited using diborane (B_2H_6). Both HCl and BCl_3 cause self-etching of the film and limit the growth rates [44]. Methylation of the $SnCl_4$ precursor [$Sn(CH_3)_xCl_{4-x}$:x=1-4)] has been proposed as the solution for reduction of self-etching; yet, there are not many successful reports available [45]. In spite of instability of SnD_4 in comparison with the other Sn precursors, its robust growth mechanism and high quality material growth has promoted researchers to still use this gas for device quality films. The shelf life of SnD_4 at room temperature is less than a week and the need for low temperature storage is a hurdle to make it usable in large scale [46]. Table I compares different methods of (Si)GeSn growth using different CVD systems.

Table I. Comparison of different CVD methods achieveing (Si)GeSn.

Growth team	Deposition system	Deposition gas precursors			Film	Buffer layer
		Si	Ge	Sn		
Applied Materials [41]	RP-CVD	-	Ge_2H_6	$SnCl_4$	GeSn	Ge
IMEC [40]	AP-CVD	-	Ge_2H_6	$SnCl_4$	GeSn	Ge
ASU [38]	UHV-CVD	Si_4H_{10}	Ge_3H_8, Ge_4H_{10}	SnD_4	(Si)GeSn	Ge
ASU [39]	UHV-CVD	$SiGeH_6$	$SiGeH_6$	SnD_4	SiGeSn	GeSn
PGI-9 [42, 43]	RP-CVD	Si_2H_6	Ge_2H_6	$SnCl_4$	(Si)GeSn	No
This work	UHV-CVD	SiH_4	GeH_4	$SnCl_4$, SnD_4	(Si)GeSn	No

1.3. Organization

The goal of this research was to develop a low temperature growth method of Si-Ge-Sn alloys using commercial precursors of silane and germane via CVD method. In Chapter 2, the chemical vapor deposition systems that were used to grow the materials are explained. The majority of the material growth was done with a system that was designed and built in the

engineering research center at the University of Arkansas. In Chapter 3, plasma enhanced CVD growth of Si and reduced pressure CVD of the Ge and SiGe materials are presented as low temperature growth methods. In Chapter 4, growth and characterization of GeSn and SiGeSn films using stannic chloride are presented. Chapter 5 discusses the growth of GeSn and SiGeSn films using in-situ gas mixing of SnD_4, SiH_4, and GeH_4. In Chapter 6, material characterization of compressively strained GeSn films grown with a mainstream CVD system is presented. The study of defect formation and propagation as well as rapid thermal annealing of the films are discussed. The summary, conclusion and future work of this research are presented in Chapter 7.

Chapter 2. Chemical vapor deposition systems for material growth

Three different deposition systems were used in this research for the growth of Si-Ge-Sn materials. The main system for the growth of Si-Ge-Sn alloys was a cold-wall, ultra-high vacuum, plasma enhanced chemical vapor deposition (UHV-PECVD) system that was designed and built at the University of Arkansas engineering research center (UA ENRC). A multi-chamber chemical vapor deposition system was used for the growth of Si at low temperatures. An ASM Epsilon® reduced pressure chemical vapor deposition (CVD) rector was used for the growth of GeSn films. The details of each system are discussed in the following sections.

2.1. The UHV-PECVD system

2.1.1. The lab design

A cold-wall UHV-PECVD system was designed for the growth of group IV semiconductor alloys. Figure 4 shows the design of the lab that encloses the UHV-PECVD reactor. Due to the usage of toxic gases, highest safety standards were implemented as can be seen in Figure 4. The gases were kept in exhausted gas cabinets in the gas farm with a sprinkler placed in each cabinet as a heat suppressor. The flow of the toxic gases was limited by a restrictive flow orifice and an excessive flow sensor connected to a high pressure valve. The gases were monitored by gas sniffers in the gas farm and in the lab.

The gas lines passed through an exhausted secondary containment (shown by dotted lines in Figure 4) in order to connect the cylinders to the gas manifold. Gases were mixed in the gas manifold prior to entering the process chamber. After film deposition, the exhaust gases passed through the turbo pump and mechanical pump and reached the gas reactor column (GRC) to abate the toxic gases to non-hazardous salts. Eventually, the gases were released to

the air through a burn box. The details of different parts of the system are explained in the following sections.

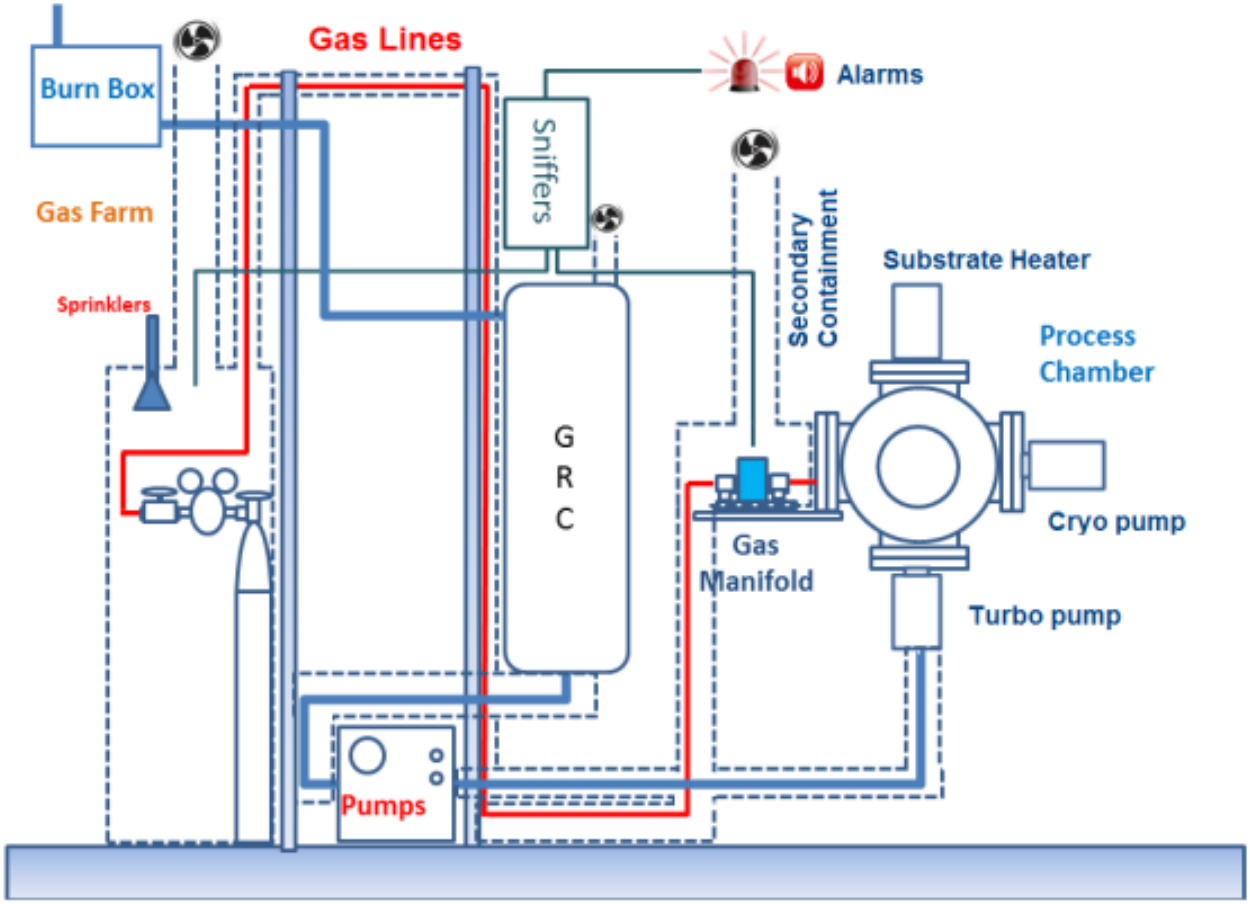

Figure 4. The lab design of the UHV-PECVD system. The lab was divided into three sections: gas farm (gas cylinders), chase (mechanical pump and chiller), and UHV-PECVD reactor lab.

2.1.2. The UHV-PECVD reactor design

Figure 5 depicts the UHV-PECVD reactor design. The reactor was composed of a load-lock chamber and a process chamber that were separated with a gate valve. The load-lock chamber was pumped with a turbo-molecular pump and the process chamber was pumped with turbo-molecular and cryogenic pumps. The turbo-molecular pumps were backed by mechanical pumps. The samples were transferred from the load-lock to the process chamber with a magnetic arm and were held with the substrate heater assembly. The heating assembly was

capable of reaching 1000 °C and had a substrate rotation as high as 80 rpm for uniform film growth. It could also be biased with plasma power as high as 80 W. Additionally, a plasma electrode was facing the substrate holder from the bottom of the process chamber in order to form plasma.

All the precursors except for tin precursors, $SnCl_4$ and SnD_4, were stored in the gas farm. The design for the delivery of Sn in the chamber will be discussed in the following sections. The flow of the gases to the process chamber was controlled with mass flow controllers (MFCs) which were calibrated for each gas.

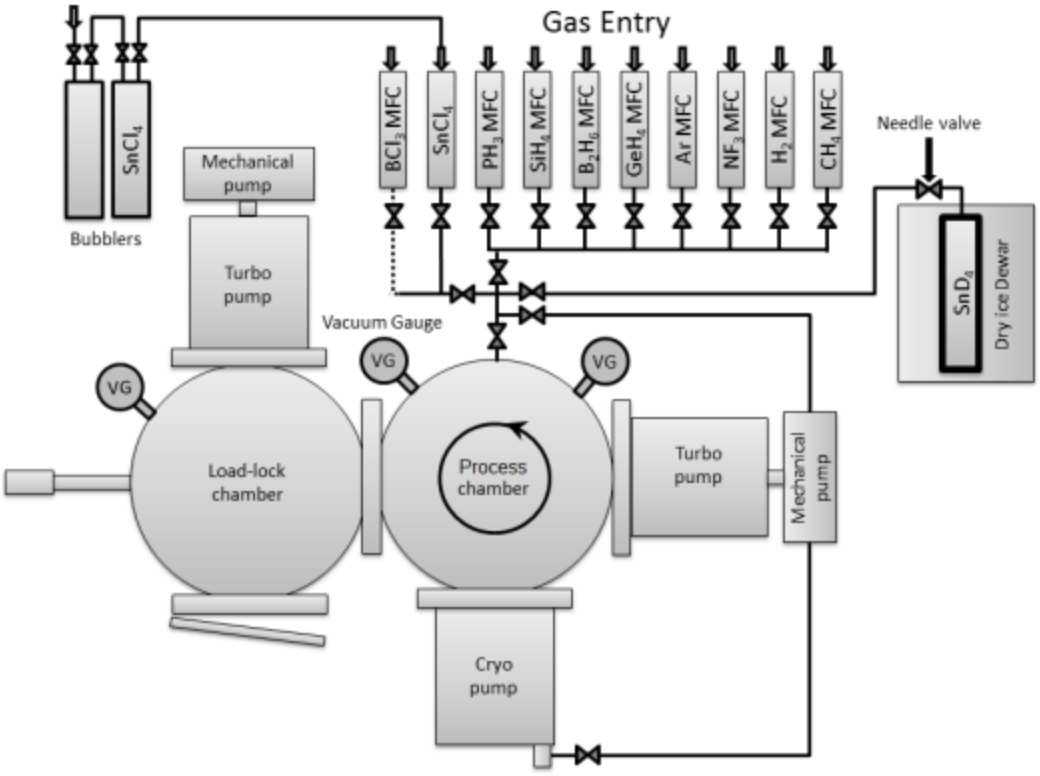

Figure 5. UHV-PE-CVD reactor design.

The details of the system assembly and the different safety criteria that were taken into account for building the system are explained in the following sections.

2.1.3. Process chamber and load-lock chamber assembly

Growth of the materials took place in the process chamber; however, a load-lock chamber was designed so that the samples were loaded and pumped down in order to minimize the transfer of contamination into the process chamber. Figure 6 shows the platform with the two chambers separated by a gate valve. The load-lock chamber was designed to reach a minimum pressure of 10^{-8} torr. The process chamber was pumped down to 10^{-10} torr after transferring the sample.

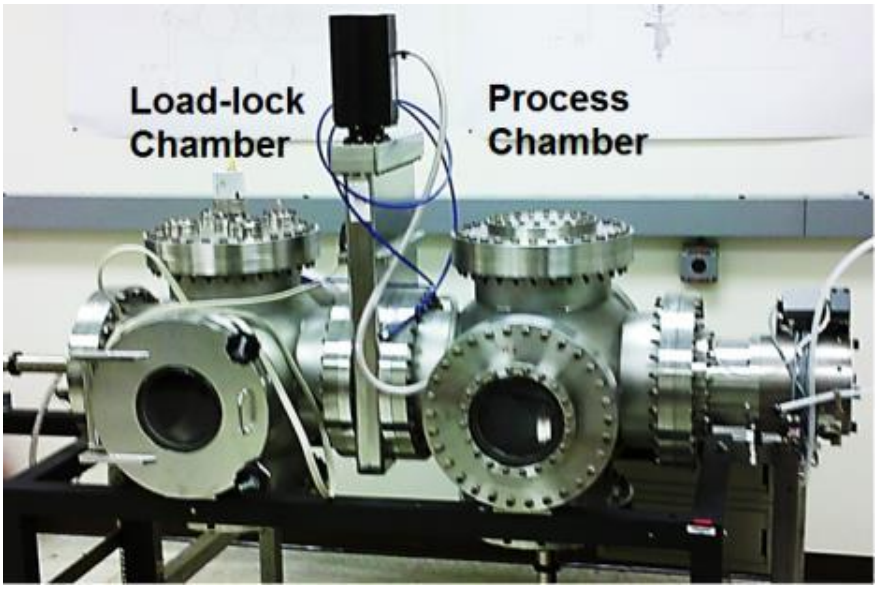

Figure 6. The starting platform containing a load-lock chamber and a process chamber.

2.1.4. Vacuum ranges, pumps, and pressure measurement

Vacuum ranges

In order to achieve ultra-high vacuum, the chamber was pumped with different pumps for different vacuum ranges. The vacuum ranges were categorized based on the mean free path of the gases in the chamber. The mean free path (λ) is the distance a molecule travels before hitting another one and it is calculated using Equation 3:

$$\lambda = \frac{RT}{\sqrt{2}d^2 N_A P} \quad \text{(Equation 3)}$$

where R is the universal gas constant and N_A is the Avogadro's number. Mean free path depends on the pressure (P), temperature (T), and diameter of the molecule (d) [47]. Table II shows the number density and mean-free path for different ranges of pressure, calculated for nitrogen (d = 3.8×10^{-8} cm). The flow regime for each pressure range, the proper pumps and the vacuum gauges are also listed in Table II.

Table II. Different pressure ranges, their properties, and required gauges and pumps.

Pressure range	Pressure (Torr)	Molecular density (cm^{-3})	Mean free path (cm)	Flow regime	Vacuum gauge	Pump type
Atmosphere	760	2.7×10^{19}	7×10^{-6}	Viscous	Pirani	Mechanical
Rough vacuum	10^{-3}	3.5×10^{13}	5	Transition	Capacitance monameter	Mechanical
High vacuum	10^{-6}	3.5×10^{10}	5×10^{3}	Molecular	Cold Cathode	Turbo-molecular
Very high vacuum	10^{-9}	3.5×10^{7}	5×10^{6}	Molecular	Cold Cathode	Turbo-molecular
Ultra high vacuum	10^{-12}	3.5×10^{4}	5×10^{9}	Molecular	Cold Cathode	Cryogenic

Pumps and gauges

A mechanical pump was used to pump the chamber from atmospheric pressure to rough vacuum (10^{-3} torr). The mean-free-path of molecules at this pressure range is around 5 cm which causes the gases to behave as a fluid and flow in the viscous regime [48]. In this regime, the gas can cool down a hot filament as it passes by. This is the idea behind a Pirani gauge which is made of a Wheatstone bridge with two heated elements. The convectron gauge was also used for the same range. It works based on keeping the filament temperature constant as it

is affected by the gas convection at different pressures. Figure 7 shows the corrosion resistant and the non-corrosion resistant mechanical pumps that were used for the process chamber and the load-lock chamber, respectively. Figure 7c depicts the convectron gauge used in in the load-lock pump line.

To reach the next stage of vacuum, a turbomolecular pump was used which can pump down the chamber from rough vacuum (10^{-3} torr) to very high vacuum (10^{-9} torr). Increase of mean-free-path down to 5×10^{6} cm, which is larger than the size of the chamber, changes the flow regime to molecular flow [48]. The turbomolcular pumps need to be backed by a mechanical pump at all times to keep the pressure difference between both sides. Due to the presence of corrosive gases in the process chamber, the pumps were chosen to be corrosion resistant. Figure 8 shows the corrosion resistant turbo-pump on the process chamber and the non-corrosion resistant turbo-pump on the load-lock chamber. The turbo pumps were isolated from the chamber by a gate valve. In order to control the pressure in the process chamber, a throttle valve was used before the turbo pump to reduce the pumping rate of the turbo (Figure 8). This was mainly done to maintain the pressure for the deposition.

The pressure measurement in the range of rough vacuum and high vacuum was performed using a capacitance manometer which works based on the changes of the capacitance. A movable diaphragm placed in front of a fixed sensor causes a change in the capacitance as the diaphragm changes position at different pressures. As the sensor is not exposed to the gas, it is a suitable gauge for process gases. A cold cathode gauge was used for measuring the pressures below 10^{-4} torr. In a cold cathode gauge, a high voltage ionizes the gases to form plasma and then a magnetic field directs the ions to the other electrode. The pressure is measured by the current produced in the electrode. Cold cathode gauges should be

protected from pressures above 10^{-4} torr. For this purpose, a high vacuum valve was used to isolate the cold cathode gauge. Figure 9 shows the vacuum gauges installed on the process chamber and the load-lock chamber.

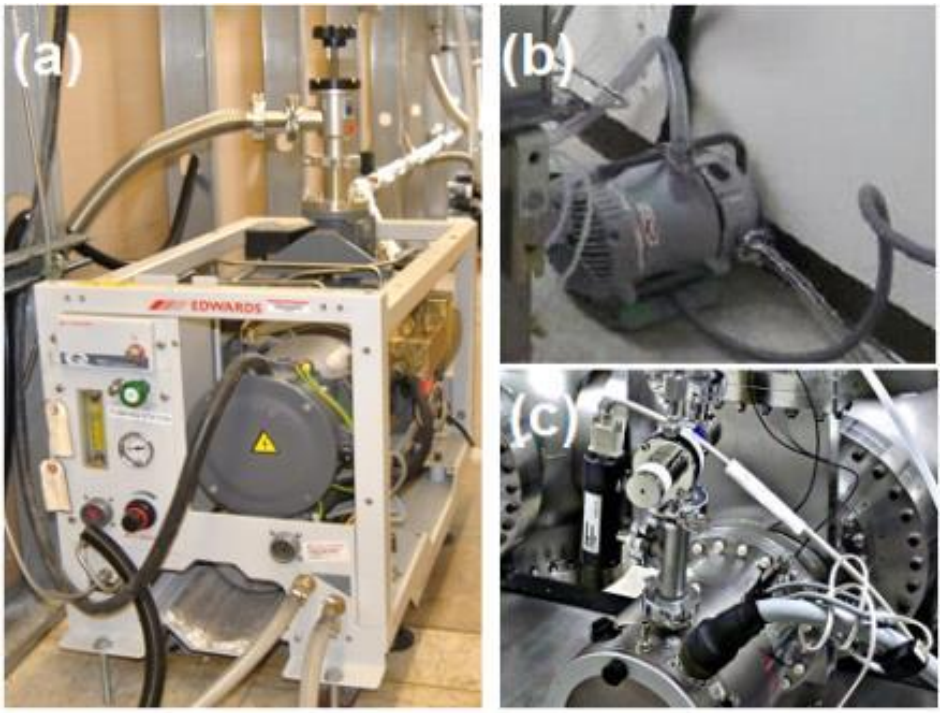

Figure 7. Mechanical pumps and vacuum gauges used for the rough vacuum range. (a) Corrosion resistant mechanical pump (Edwards QDP40), (b) non-corrosion resistant mechanical pump (Edwards XDS10), and (c) Convectron gauge on the load-lock pump line.

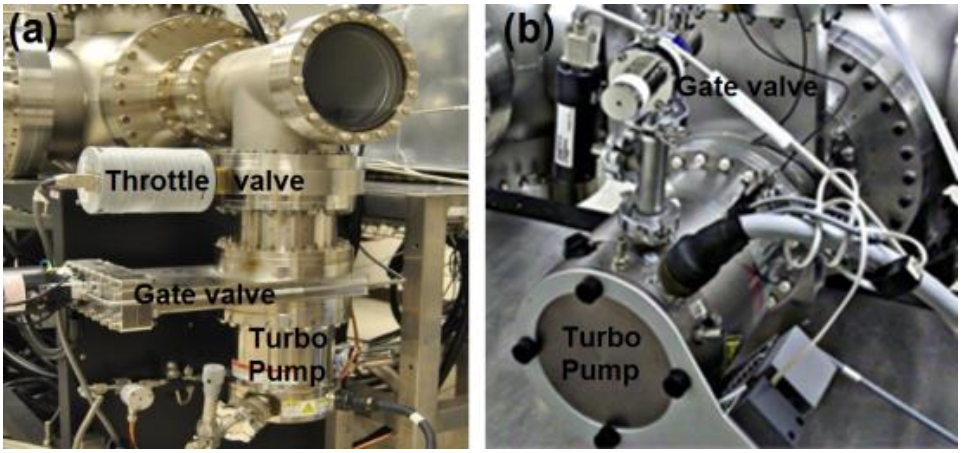

Figure 8. Turbo-pumps used for pumping the chambers down to very high vacuum range. (a) The corrosion resistant turbo-pump (Edwards STP) connected to the process chamber and (b) the non-corrosion resistant turbo-pump connected to the load-lock chamber.

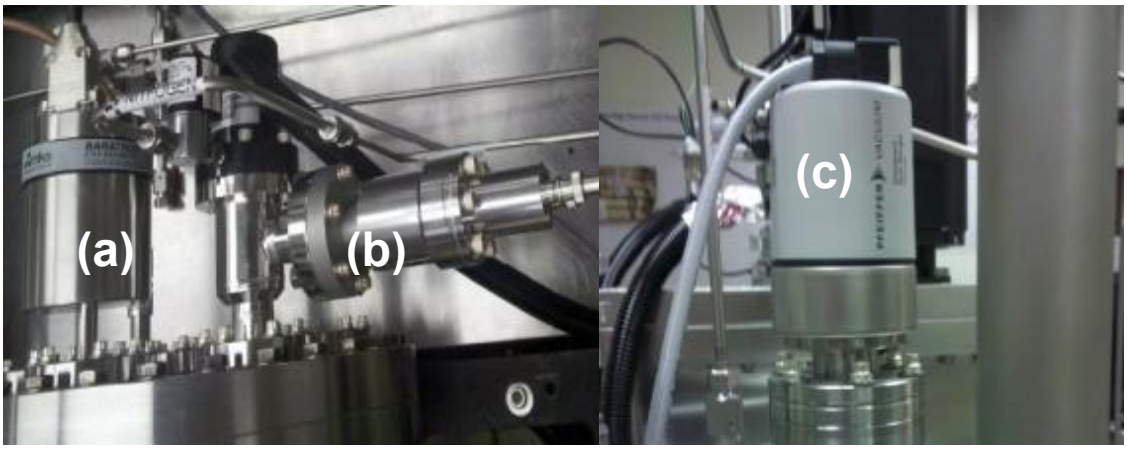

Figure 9. Vacuum gauges used for monitoring the growth pressure. Capacitance monometer gauge (a) and cold cathode gauge (b) installed on the process chamber. (c) Full range gauge including a pirani and a cold cathode gauge installed on the load-lock chamber.

In order to reach ultra-high vacuum in the process chamber, a cryogenic pump was used only after reaching 10^{-8} torr to reduce the pressure down to 10^{-10} torr (Figure 10). A cryogenic pump works based on a cold finger that is cooled down by a closed loop of liquid helium as low as 10 K. At such low temperature, all the gases except for hydrogen, helium and neon are condensed. Therefore, by reaching the ultimate base pressure using the cryogenic pump, the oxygen and water vapor are pumped down more efficiently.

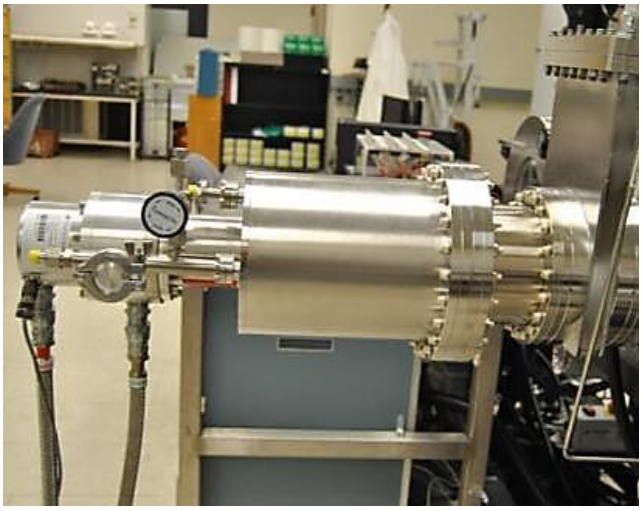

Figure 10. Cryogenic pump isolated from the process chamber by a gate valve.

2.1.5. Substrate heater assembly

The heating assembly consisted of a graphite heater coated with pyrolytic graphite for protection from oxidation. The maximum achievable temperature by the heater assembly was 1000 °C measured by a thermocouple located above the heater. The thermocouple and wafer were at the same distance (12 mm) away from the heater for more accurate reading of substrate temperature. The substrate holder was capable of rotation as high as 80 rpm for uniform film growth. In order to assure that the heater assembly was compatible with the process gases, the materials used in the heater were custom made from molybdenum, stainless steel, and aluminum oxide ceramic. In addition, in order to save the heating element from the etchant gases, an inert gas line was fed through the heater assembly to be used for the time of etch-cleaning the chamber with plasma. The substrate heater was capable of accommodating 80 W of power if it was used as the biased electrode.

Figure 11. Substrate heater assembly used in the process chamber. (a) Inside portion containing the heater and (b) outside portion containing the electric and gas lines.

2.1.6. Plasma electrode assembly

An adjustable position plasma electrode was located below the substrate heater assembly to be able to generate plasma close and far from the substrate. The electrode could achieve a minimum distance of 10 mm and a maximum distance of 121 mm from the substrate heater assembly. The plasma electrode was designed with a dark space shield so that the far field plasma could be ignited with low plasma power without grounding the top substrate heater assembly. Figure 12a shows the design of the electrode, Figure 12b shows the plasma electrode, and Figure 12c the H_2+GeH_4 plasma generated at 0.5 torr pressure and 5 W plasma power.

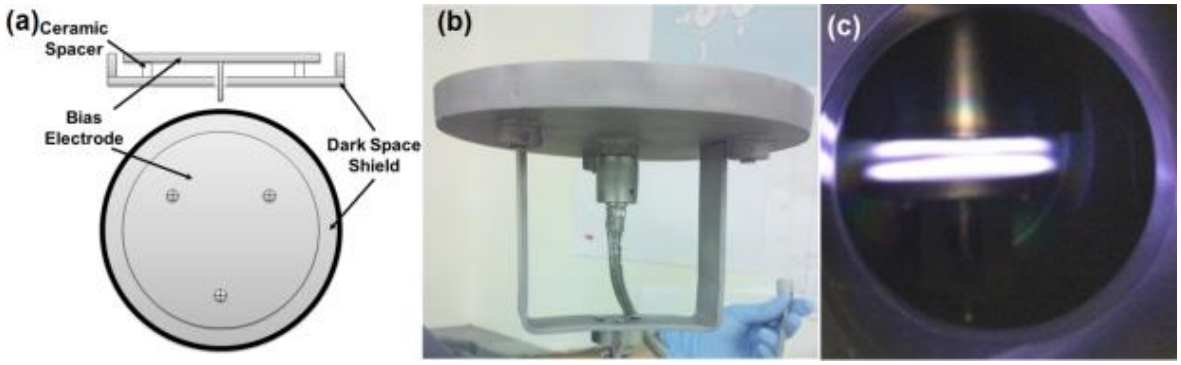

Figure 12. The plasma electrode used for striking plasma in the process chamber. (a) Side view and top view of the plasma electrode design. (b) Side view of the plasma electrode. (c) The H_2+GeH_4 plasma generated inside the chamber.

2.1.7. Safety consideration and design features

Pumps and chamber connections

Turbo pumps and the cryo pump were separated from the chambers by gate valves with the leak rates as low as 10^{-11} torr$\frac{L}{s}$. The chambers and all the connections had ConFlat (CF) flanges with knife edge and Cu gasket which reduced the leak rate to 10^{-11} torr$\frac{L}{s}$. Tempered

glass was used for the view port of the chambers. The load-lock door had a Viton® seal with a leak rate as low as 10^{-9} torr$\frac{L}{s}$. The load-lock and process chambers were bakeable to 250 °C.

The corrosion resistant turbo pump and the corrosion resistant mechanical pumps were both ballasted with nitrogen so that the process gases were diluted as they were being pumped from the chamber. The mechanical pumps were all dry scroll pumps in order to reduce the possibility of chamber contamination. To save the cryo pump from exposure to process gases, an interlock system was designed to disable the gas entry when the cryo gate valve was open. In addition, the cryo gate valve closed if the chamber pressure exceeded 10^{-7} torr.

Gas lines and manifold

The gas lines were made from ¼" electro-polished stainless steel tubes with metal gasket face seal fittings (VCR®). The VCR® connections were used with nickel gaskets in order to keep the leak rates as low as 3×10^{-9} torr$\frac{L}{s}$. All the VCR connections were secured with a lock to reduce the possibility of loosening in case of stress application to the lines. The gas lines and their connections were exhausted with a fan and secondary containment around them (Figure 13).

Figure 13. Secondary containment located above the gas manifold. All the MFCs and VCR connections were exhausted with secondary containment.

Gas cylinders, cabinets, and gas farm

Gas cylinders were all placed in exhausted gas cabinets (Figure 14a). A restrictive flow orifice of 0.01" was placed in the cylinder valve outlet in order to reduce the gas flow. In addition, the gas panels for the toxic gases were equipped with an excessive flow meter that would shut off a high pressure valve if high gas flux was detected in the line. The SiH_4 gas cabinet had an IR detector that would detect if gas leakage occurred. Gas cabinets were located in the gas farm outside the lab except for those used for Sn precursors. Each cabinet was equipped with a sprinkler system that would cool down the cylinders in case of fire.

Hazardous gas monitoring and alarm system

A gas detection and alarm system was installed in order to detect a leak at 10% of the threshold limit value (TLV) for each gas. The detectors would sniff the gases in the gas farm for each cabinet, in the lab over the gas manifold hood, and in the ambient (Figure 14b). The audio and visual alarms would go off in case of leak detection and the University of Arkansas police department would be informed automatically. All the valves would shut off and the flow of all gases would be stopped in this situation.

Hazardous gas abatement

A gas reactor column (GRC) was placed after the corrosion resistant mechanical pump to abate the gases after being processed in the chamber (Figure 14c). The abatement system works on the basis of making non-hazardous salts from hazardous gases. The line that connects the mechanical pump to the GRC was heated to prevent deposition of phosphorus if phosphine (PH_3) was used in the process. The GRC cartridge that abates the gases was heated as high as 550 °C and the temperature was monitored at all times. An alarm system would notify the building personnel if the temperature dropped.

2.1.8. Tin precursor delivery

Stannic chloride and deuterated stannane were used as Sn precursors for the growth of GeSn and SiGeSn films. Stannic chloride is a liquid and deuterated stannane is an unstable gas; therefore, two different delivery systems were designed and made for this purpose. In the next subsections these two delivery systems are explained.

Figure 14. Safety features implemented inside and outside the lab. (a) Exhausted gas cabinet in the gas farm, (b) gas sniffers that detect inside the lab (top) and in the gas farm (bottom), and (c) gas reactor column.

Stannic chloride delivery

Stannic chloride is a liquid that boils at 112 °C and has a vapor pressure of 18 torr at room temperature. In order to deliver $SnCl_4$, a bubbler system was designed so that a carrier gas could bubble through the liquid and transport $SnCl_4$ to the chamber. Due to fast oxidation of $SnCl_4$ in air, an inert filled hood was used to fill the bubblers. A mass flow controller that was calibrated for the carrier gas was used to control the gas flow due to the low amount of $SnCl_4$ in the carrier gas. Figure 15a shows the design for the bubbler system. Two bubblers were connected in a way that the carrier gas passed through the first bubbler, entered the second one, bubbled through $SnCl_4$, and then entered the gas manifold. The reason for using two bubblers was to stop liquid back flow in the gas line. If the pressure on the manifold side was

increased, it would push the $SnCl_4$ liquid toward the second bubbler. Excessive pressure on the gas manifold would not be able to push the liquid back toward the carrier gas bottle even if the second bubbler was filled with all the liquid.

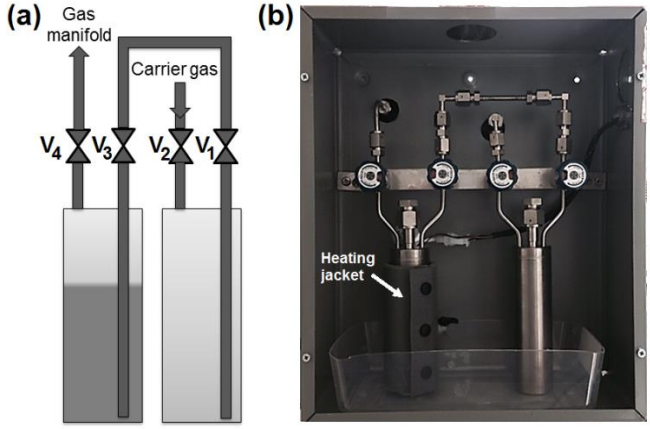

Figure 15. The bubbler system used for deligvering $SnCl_4$ to the process chamber. (a) Schematics of the bubbler system design. (b) The bubbler system with a heating jacket around the bubbler that contains the $SnCl_4$.

The second way of delivering the gas was to isolate the second bubbler by closing valve 3 (V_3) (Figure 15a) and use the vapor pressure of the $SnCl_4$ liquid. The vapor pressure could be increased by heating the bubbler using a heating jacket as shown in Figure 15b. For this case, a low pressure mass flow controller was installed for more accurate control due to the low supply pressure.

Deuterated stannane delivery

Deuterated stannane is an unstable gas and its fast decomposition requires storage at liquid nitrogen temperature (-200 °C). The boiling temperature of SnD_4 is -56 °C and its stability at room temperature is less than one week [46]. In order to deliver the gas to the chamber, it needed to be warmed up but kept at dry ice temperature (-80 °C) to have a longer lifetime. Furthermore, fast decomposition of SnD_4 in the delivery line and MFC walls causes inaccurate flow readings. This is mainly because MFCs work on the basis of measuring the

heat conductance of the gas as it passes through a heated bypass tube and controlling the flow with a needle valve. As SnD_4 is heated, it deposits on the line and causes less gas to pass and also changes the heat conductance of the tubing. Therefore, the reading of MFC would not be accurate and a pressure-based system was adopted rather than using MFC. The operational diagram of a MFC is shown in Figure 16.

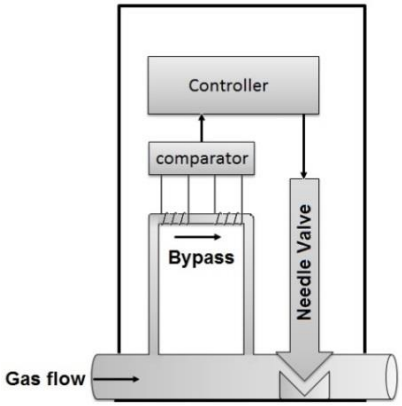

Figure 16. Operational diagram of a MFC.

Introduction of the gases in the chamber resulted in an increase in the pressure of the chamber. The flow rate of the gases were calibrated by measuring the pressure as the flow rate increased. The process chamber pressure was controlled by a throttle valve which was placed before the turbopump. In order to calibrate the flow rates with the deposition pressure in the system, the throttle valve was placed at different opening positions and the flow rates of the gases were changed. For example, at 1% open position of the throttle valve, the flow rate of Ar was changed from 5 to 50 sccm (at 5 sccm steps) and the corresponding pressure was recorded. The same procedure was adopted for germane and silane. The partial pressures of all gases were measured by a capacitance monometer pressure gauge in the process chamber (Figure 5). Figure 17 shows the calibration of the pressure reading of argon and germane for different flow rates at 1 to 3% open position of the throttle valve.

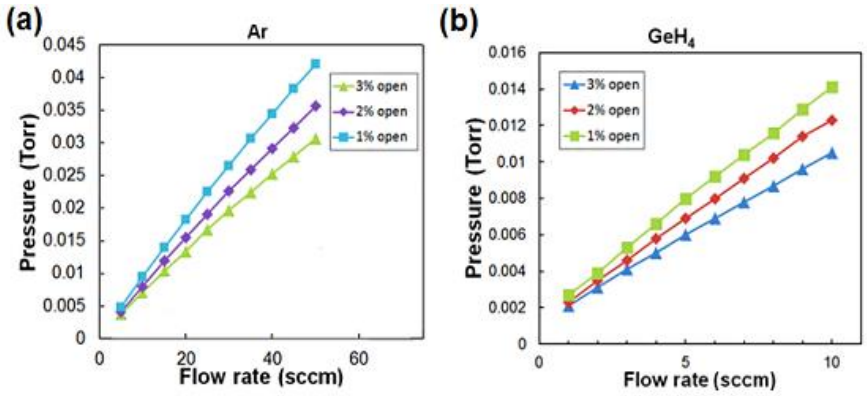

Figure 17. Calibration of pressure reading with the flow rate of gases in the process chamber. (a) Argon and (b) germane for different flow rates at 1 to 3% open position of the throttle valve.

Deuterated stannane is liquid and has a vapor pressure of 17.4 torr at -112 °C and boils at 58 °C; therefore, it was kept in the -60 to -80 °C (using dry ice) temperature range to assure that it was in the liquid form and the vapor pressure of the gas could be used to deliver the gas to the chamber (Figure 18 a). In order to determine the partial pressure of SnD_4, a needle valve was placed on the delivery line to control the gas flow in the chamber (Figure 18b). By opening the needle valve at different positions, the partial pressure of the gas was controlled from 0 to 1.5 mtorr range.

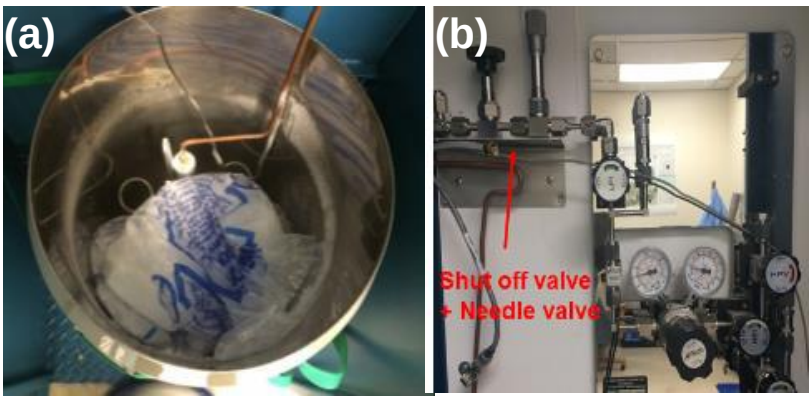

Figure 18. SnD_4 delivery system containing a Dewar and gas panel. (a) The SnD_4 bottle was placed in a Dewar covered with dry ice. The temperature was monitored with a thermocouple placed on the bottle. (b) The needle valve was placed after the gas regulators in order to control the SnD_4 flow.

2.1.9. Final system design

Figure 19 shows the final configuration of the UHV-PECVD system located in Lab 350C at UA ENRC. The system was composed of the CVD reactor, the Sn precursor delivery system, gas manifold, and gas sniffers as explained in the prior sections.

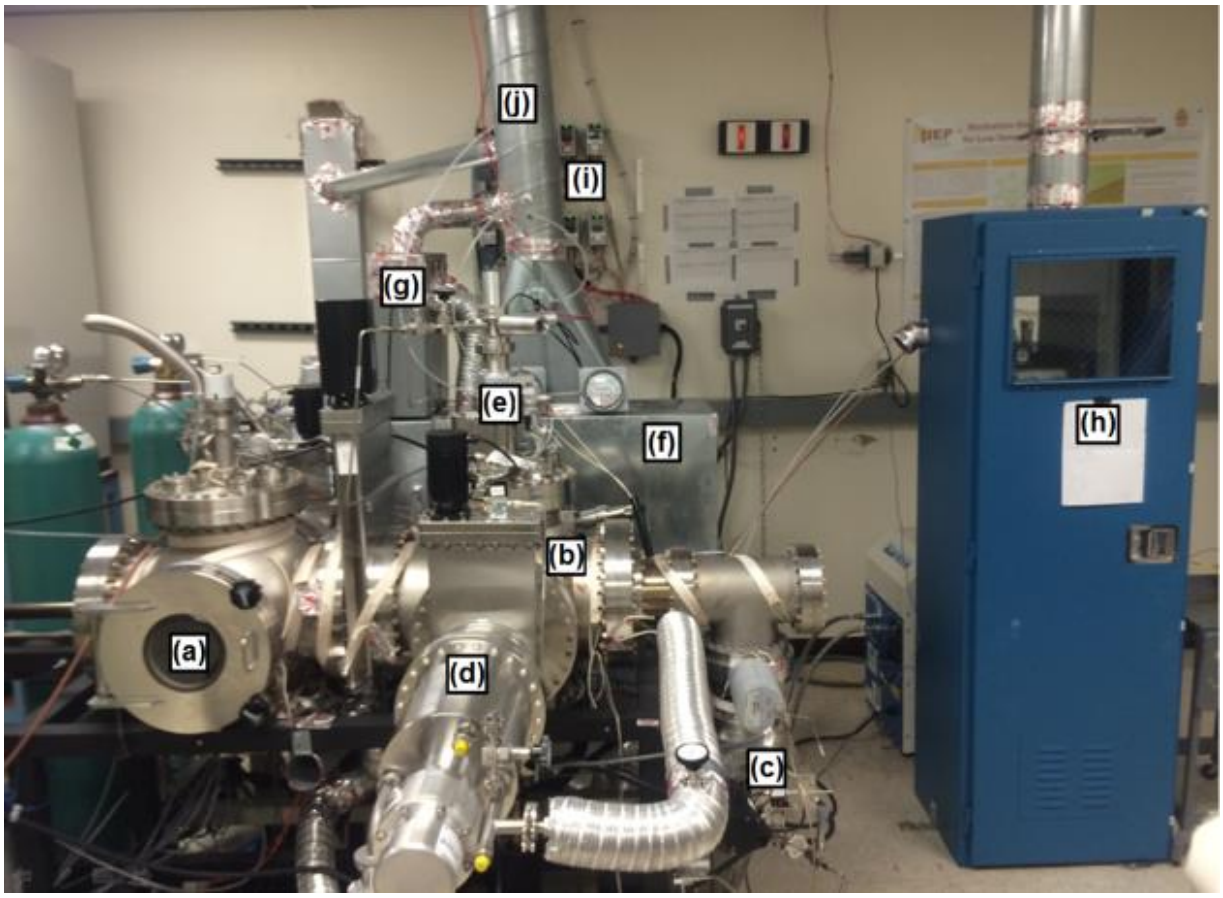

Figure 19. Cold-wall ultra-high vacuum plasma-enhanced chemical vapor deposition system: (a) load-lock chamber, (b) process chamber. (c)turbopump. (d) cryogenic pump, (e) substrate heater assembly, (f) the gas manifold hood, (g) the gas cabinet for stannic chloride bubbler system, (h) gas cabinet for stannane delivery system, (i) gas detector, and (j) exhausted secondary containment.

2.2. Multi-chamber cluster tool

The high vacuum plasma enhanced CVD chamber of a multi chamber cluster tool at UA ENRC Lab 350B was used to grow c-Si epitaxial layers (Figure 20a). The samples were passed

through a load-lock to reach MPZ 1 by using an automatic arm. After loading the sample through the loading station, the load-lock chamber was pumped down to 10^{-3} torr to keep the contaminants away from the process chamber. The samples were transferred to the process chamber using an automatic arm. The process chamber was pumped down to 10^{-8} torr using a turbomolecular pump. Samples were cut in 1"×1" sizes from a 500 μm thick CZ grown Si (100) wafer. They were placed facing down on the grounded top electrode, which was 15 mm away from the bottom powered electrode (Figure 20b).

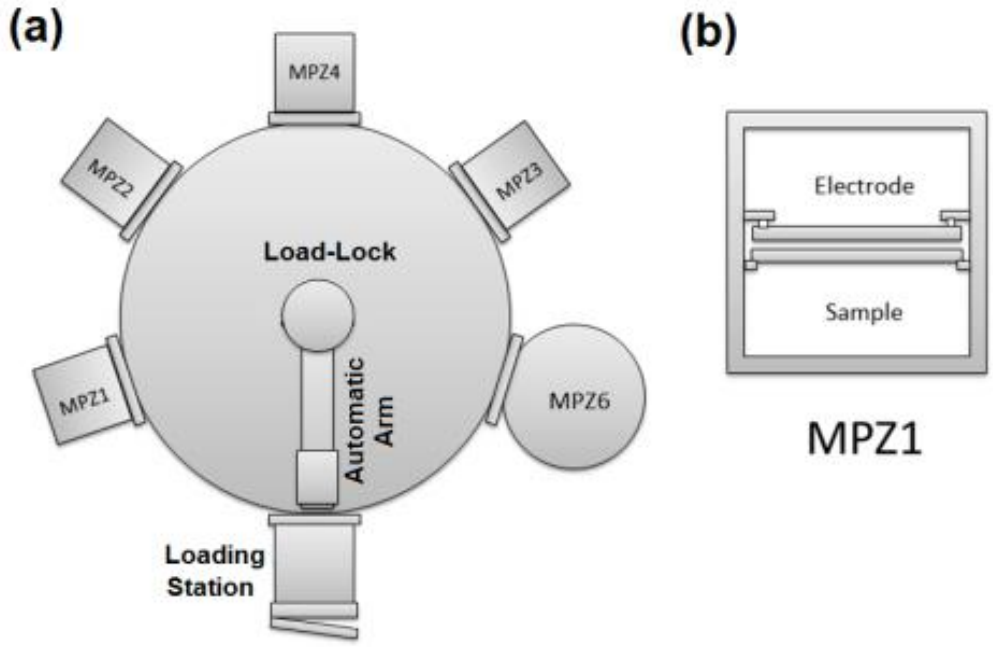

Figure 20. Multi-chamber cluster tool with five vacuum chambers. (a) Top view schematic of the system. (b) Cross-sectional schematic of MPZ1 chamber showing the sample location and plasma electrode.

2.3. Reduced pressure CVD

The GeSn alloy films received from ASM America Inc. were grown using an Epsilon® 2000 Plus reactor which is a single wafer RPCVD epitaxial deposition system (Figure 21). It

was comprised of a load-lock chamber and a process chamber with a cold-wall quartz deposition chamber encasing a silicon carbide coated graphite susceptor heated via an array of halogen lamps controlled by a closed loop feedback system. The system featured a unique non-contact wafer transfer technology called a Bernoulli wand that could transfer the sample without damaging the surface and provided the ability to achieve high throughput film growth.

Figure 21. ASM Epsilon® 2000 Plus RPCVD reactor [49].

Chapter 3. Silicon, Ge, and SiGe epitaxy

All group IV elements (except Pb) form similar diamond crystal structure; therefore, studying the growth mechanism of Si and Ge and their alloys (SiGe) is essential in developing the technology for the growth of other group IV alloys. Silicon and Ge are fully miscible with different compositions and have less lattice mismatch in comparison with other group elements. However, Si is deposited at higher temperatures in comparison with Ge in regular CVD processes. Growing high quality Si films at low temperatures is challenging. In this chapter, low temperature growth of Si using plasma enhancement is discussed. In the following subsections, growth of Ge and SiGe is presented using RPCVD processes.

3.1. Si epitaxy

Low temperature silicon epitaxy has been mainly pursued to achieve abrupt doping profiles in metal–oxide–semiconductor field-effect transistor (MOSFET) channels [50] and thin film crystalline solar cells [51]. Elimination of auto-doping from bulk substrates to the grown film enables use of low cost substrates such as seeded glass and metallurgical grade silicon. The main drawback for such growth regime is reduction of growth rate and film quality; therefore, understanding the growth mechanism would help resolve the film quality issue as well as increasing the growth rate.

Plasma enhanced chemical vapor deposition has been shown to be one of the methods for low temperature Si epitaxy [52]. Highly diluted silane (in hydrogen) plasma produces reactive radicals such as: SiH_3, SiH_2, SiH, Si, H_2 and H as well as other excited states like SiH_x^*, and hydrogen breaks into atomic H or transits to a higher excited state [53]. Atomic hydrogen and SiH_3 give rise to efficient removal of hydrogen from the surface. This leads to

higher hydrogen mobility on the surface and an increase in the diffusion length of Si ad-atoms [54]. These two significant factors enable the Si ad-atoms to find the desired crystal sites resulting in crystalline epi-layer growth. Applying appropriate low plasma power is critical, as bombardment energies above 15-20 eV would introduce defects in the grown film [55]. In this section, the epitaxy mechanism and role of hydrogen in achieving high crystal quality growth are discussed. The samples in this study were grown using the high vacuum PECVD in the multi-chamber cluster tool.

3.1.1. Silicon epitaxy using multi-vacuum system

Experimental parameters were set through a semi-factorial design of experiments in the temperature range of 250-350 °C while deposition pressure was maintained constant at 500 mtorr. Silane flow rate was varied from 2 to 5 sccm with hydrogen flow rate from 95 to 98 sccm to make dilution ratios (DR) of 20, 30 and 50. Total flow was kept constant at 100 sccm. Applied RF power provided sustainable plasma power density (PPD) of 20, 50, 100 mW/cm^2 in the one hour growth time. Films were co-deposited on a Si and a glass sample. Table III shows the details of the experiments.

Table III. Experimental design for different temperatures, ratios, and power densities.

Sample	Temperature (°C)	H_2 (sccm)	SiH_4 (sccm)	DR (H_2:SiH_4)	PPD (mW/cm^2)
A	250	98.0	2.0	50	20
B	250	96.7	3.3	30	50
C	250	95.2	4.8	20	100
D	350	96.7	3.3	30	20
E	350	95.2	4.8	20	100

3.1.2. Raman spectroscopy

Raman characterization of the grown samples shows crystalline and microcrystalline Si (µc-Si) films as can be seen in Figure 22. Except for samples grown at 350 °C (D and E), no characteristic amorphous hump was found around 480 cm^{-1} for samples grown at 250 °C (A, B and C). The typical crystalline Si (c-Si) peak was seen at 520 cm^{-1}. Samples were further investigated by eliminating the high count 520 cm^{-1} peak from the graph in order to search for an amorphous peak at 480 cm^{-1}. No amorphous peak was observed for samples A and B and a barely discernible one was seen for C. Lower intensity of the 520 cm^{-1} peak in sample C also indicates the presence of less crystalline structure in the film. Raman spectroscopy was carried out at different places on the sample (and replicate runs) to ensure the reproducibility, reliability, and uniformity of the peaks; the same results appeared without any traces of amorphous characteristic hump in the samples A and B.

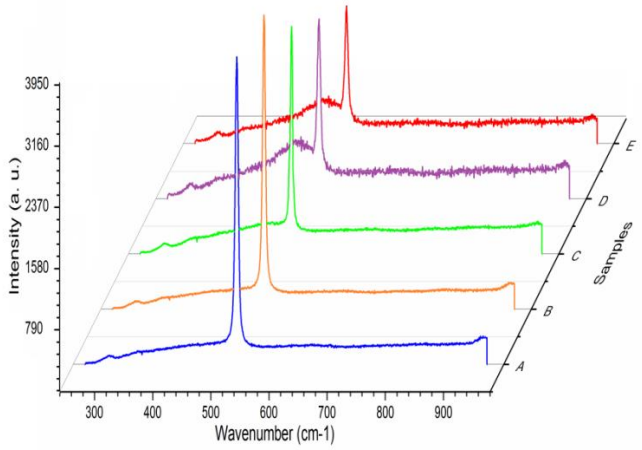

Figure 22. Raman spectra Si samples grown on Si under different conditions.

3.1.3. Transmission electron microscopy (TEM)

A high resolution TEM image of sample A is shown in Figure 23a. Crystal orientation of the atoms can be obviously seen in the substrate as well as the grown film. No amorphous

region is observed in the HR-TEM image. The film surface does not show any trace of stressed growth that can result in a saw-tooth shape. The absence of stress could be ascribed to the smooth nucleation at the film/substrate interface. The HR-TEM does not show any stacking faults and dislocations as the zoomed in image depicts in Figure 23b. The thickness of the grown Si epi-layers was measured to be 15 nm, indicating a growth rate of 0.25 nm/min. The TEM characterization, carried out randomly at different parts of the sample, revealed the same quality epi-layers. Convergent beam electron diffraction (CBED) of the layer was used to confirm the crystallinity and the absence of any possible faults in the film (Figure 23c). CBED is preferred to selective area diffraction due to the small thickness of the epi-layers; otherwise, the diffraction pattern would have had incorporation from the substrate as well. The presence of discs shows perfect crystal growth with no circular amorphous pattern.

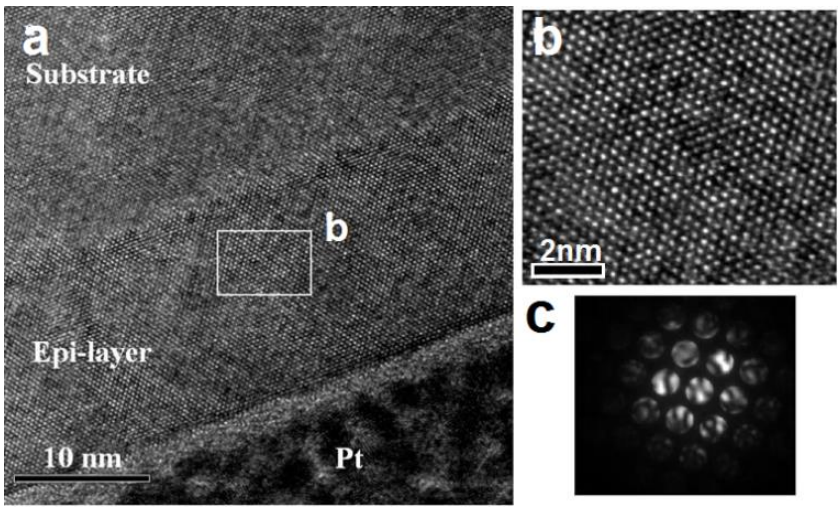

Figure 23. HR-TEM cross-sectional image of sample A, deposited at 250 °C with DR of 50 and PPD of 20 mW/cm^2. (a) Low magnification TEM image showing the Si substrate and the grown film. (b) Higher magnification TEM showing high quality film growth. (c) Convergent beam electron diffraction of the film.

Figure 24a is the HR-TEM image of sample B which was grown at higher PPD and lower DR compared to sample A but at the same temperature. It shows better film quality and

higher growth rate up to 0.34 nm/min reaching 20 nm of thickness. HR-TEM image shows perfect crystal growth of the film with the same crystal orientation of the substrate. The nucleation step at the substrate/film interface was initiated so perfectly that it is very hard to find and discern it (Figure 24b). Therefore, the thickness of the film was estimated by measuring the film thickness on the glass substrate. Smooth nucleation stopped development of stress in the film and the formation of a saw tooth features which result in a crystalline-to-amorphous transition.

The HR-TEM image does not show any stacking faults or dislocations (Figure 24c). Lower DR provided the ambient with more ad-atoms, resulting in higher growth rate, yet more precursor flow rate did not always result in a thicker crystalline film. Higher PPD produces more atomic hydrogen and higher surface mobility of the ad-atoms, which is needed for crystalline growth.

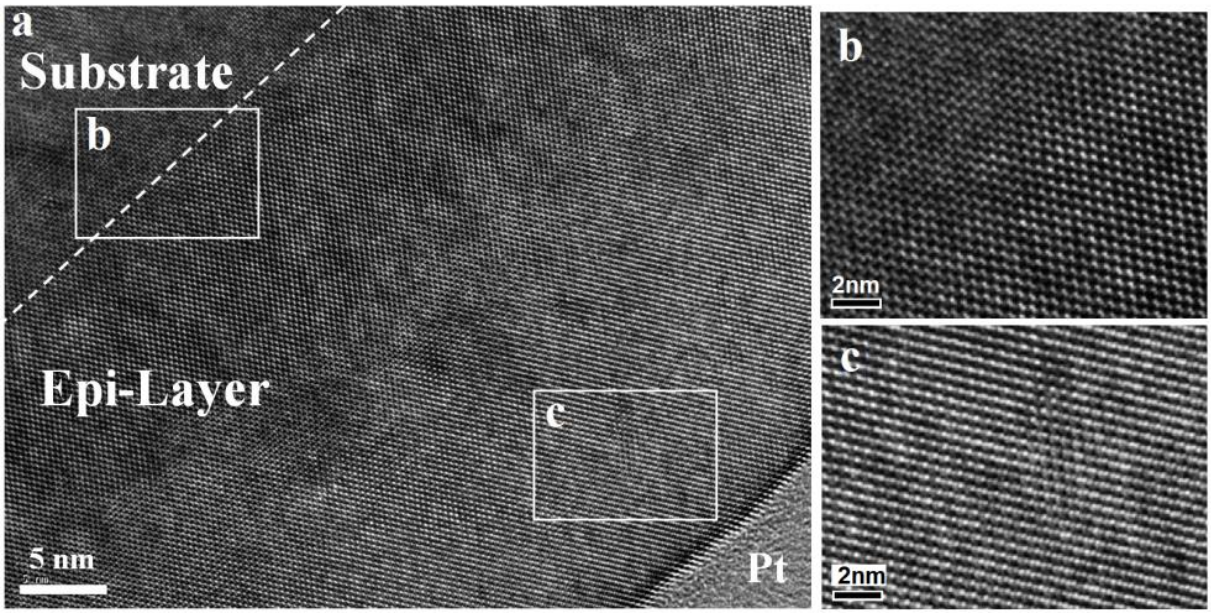

Figure 24. HR-TEM cross-sectional image of sample B, grown at 250 °C with a DR of 30 and PPD of 50 mW/cm^2. (a) Low magnification TEM image showing the Si substrate and the grown film. (b) Higher magnification of the interface. (c) Higher magnification close to the film surface.

Figure 25 shows HR-TEM images of sample C, which was grown at the same temperature as samples A and B but with lower DR (20:1) and higher PPD (100 mW/cm^2). Crystalline growth was started with rough nucleation on the surface (Figure 25c), which caused stress on the epi-layers. The films became non-epitaxial at some parts after 10 nm as a result of stressed growth. Formation of saw-tooth shape defects resulted in transition to amorphous Si (Figure 25 b) and microcrystalline (crystalline and amorphous mixed) film. High density of plasma was the main reason for the deterioration of the film quality; yet, it increased the growth rate to 0.75 nm/min and a thickness of 45 nm was achieved. Lower DR also affected the growth rate; however, low quality of the film cannot be ascribed to lower surface mobility of the ad-atoms.

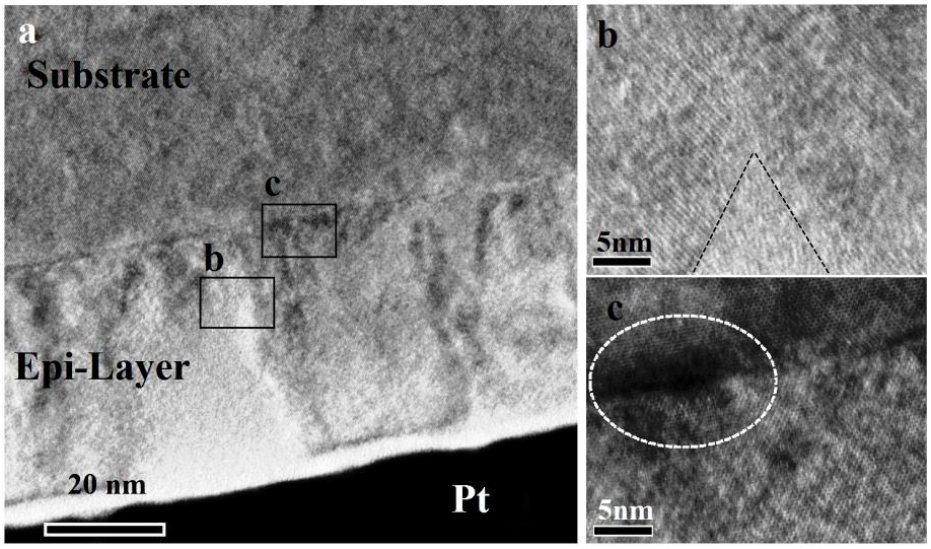

Figure 25. HR-TEM cross-sectional image of sample C, grown at 250 °C with a DR of 20 and a PPD of 100 mW/cm^2. (a) Low magnification TEM image showing the Si substrate and the grown film. (b) Crystalline to amorphous transition is seen between the dotted lines. (c) Rough nucleation is seen at the interface.

The results show that conditions for growing epitaxial Si at low temperatures are very critical and dependent on one another and the amorphous transition happens when plasma power and hydrogen dilution are not in balance. Combination of proper plasma power,

hydrogen dilution, and temperature results in an experimental space where silicon epitaxy is feasible. Presence of hydrogen on the surface is of high importance and can have a constructive or destructive role in epitaxy based on the number of H atoms passivating surface Si dangling bonds. A dihydride surface, which is formed on Si surfaces at temperatures below 407 °C, hinders movement of ad-atoms on the surface by reducing the surface diffusion length [56-58]. On the other hand, dissociation of silane molecules to SiH_x radicals and atomic hydrogen lowers the temperature at which the dihydride surface transitions to monohydride by H abstraction from the surface [59]. Therefore, it is expected that this conversion happens at low temperatures of 250-350 °C where the experiments of this work were done.

Proper adjustment of plasma power results in the production of sufficient abstracting radicals such as $SiH^{\bullet}_3$ and $H^{\bullet}$ while the surface is not bombarded with high energy radicals. Si epitaxy in a highly hydrogen diluted ambient is driven by two critical roles played by hydrogen: 1) surface diffusion length enhancement of the ad-species; and, 2) selective etching of the amorphous and defective films. Parsons et al. have shown low dilution of hydrogen ($H_2/SiH_4<10/1$) leads to a decrease in the diffusion length, but larger hydrogen dilution results in increased diffusion length [54]. On the other hand, selective amorphous etching happens as atomic hydrogen breaks weak Si-Si bonds which leads to amorphous growth and leaves the sites open for crystalline growth [60]. Thereupon, hydrogen atoms etch adsorbed silyl to gas phase unless they are in a crystal site [61].

The obtained results indicate that at fixed temperature, having high hydrogen dilution allows lower plasma power density (sample A) and by decreasing the dilution, plasma power needs to be increased (sample B). This balance is only valid to certain limits as can be seen

from sample C; further decrease in dilution and increase in plasma power density leads to growth of μc-Si. Figure 26 shows the balance parameters needed for higher quality films.

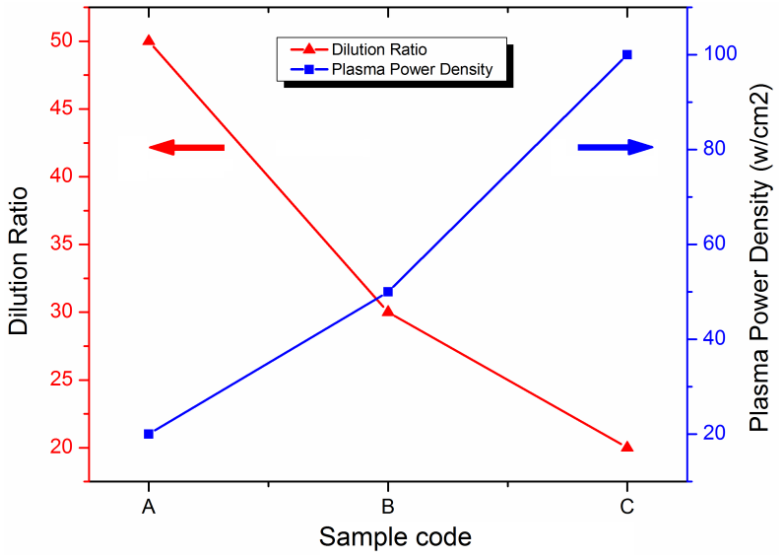

Figure 26. Balanced growth parameters achieved by DOE. Red line shows the increase in plasma power from samples A to C while dilution ratio is reduced from 50 to 20 (blue line).

For A and B sample parameters, enough atomic H and SiH_x radicals are produced while keeping the surface away from damage caused by energetic radicals. Higher plasma density results in higher energy radicals that cause rough surface nucleation and stressed film growth as well as defect introduction [55] as can be seen in sample C (Figure 25). Growth temperature is chosen to be 250-350 °C to ensure surface hydrogen coverage as well as to keep the growth in layer-by-layer mode [62]. Although more than one hydrogen atom passivates surface Si dangling bonds at these temperatures, results of this work show that the number of hydrogen per atom does not affect epitaxial growth as long as appropriate plasma power is applied to produce hydrogen abstracting radicals such as $SiH^{\bullet}_3$ and $H^{\bullet}$ [59]. Higher surface temperature in samples D and E (which were at 350 °C) have less dihydride surface as hydrogen desorbs at higher temperatures [56]; therefore, less plasma power density is more appropriate. Raman spectra of

sample E shows more a-Si:H which can be attributed to high plasma power density while sample D, which was grown at lower plasma density, shows less a-Si:H. The growth rate is determined by the number of reactive species ready to deposit per unit time; therefore, growth rate is low in higher DR and lower plasma densities. This trend can be clearly seen by comparing the growth rates from sample A to C. On the other hand, sample C did not show high quality in comparison to A and B due to the high plasma power. This can be explained by the effect of rough interface nucleation on the growth of epi-layers [22].

3.1.4. Atomic force microscopy

Increase in surface roughness and hydrogen content of the film are the main reasons for the transition of crystalline growth to amorphous at low temperatures [63]. The TEM images show that the films grown at balanced growth conditions have smooth surfaces. The AFM images of surface morphology confirm this claim. The average surface roughness over an area of 1 μm × 1 μm for bare Si substrate, and for samples A and B, were measured to be 0.128 nm, 0.167 nm, and 0.136 nm, respectively (Figure 27). These values show that sample B which had a better film quality has less surface roughness. Surface roughness increase can be attributed to two major phenomena: high energy radical bombardment and atomic hydrogen etching of the surface.

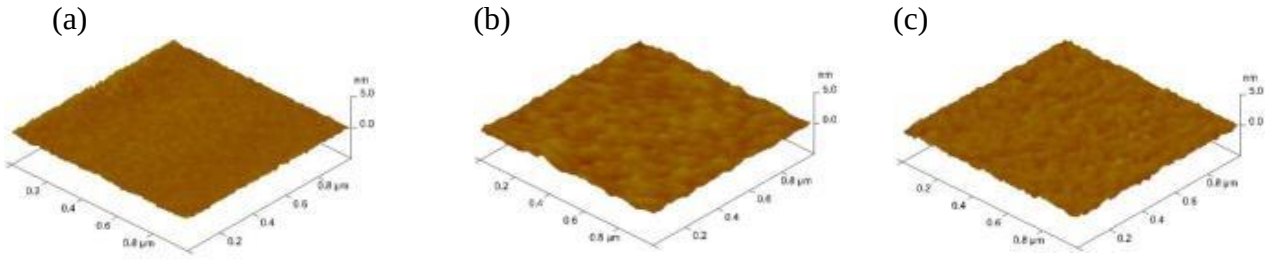

Figure 27. Comparison of AFM images of a epitaxial layers with bare Si over an area of 1μm×1μm. (a) Bare Si substrate, (b) sample B, (c) sample C.

The increase in roughness at higher dilution and lower plasma density is attributed to the etching of the surface by H radicals because deposition rate also decreases at these conditions. On the other hand, surface smoothing at these conditions was due to enhancement of ad-atom mobility on the surface. Therefore, achievement of surface roughness comparable to bare silicon implies the surface diffusion enhancement role of hydrogen surpasses the selective amorphous etching role.

3.1.5. Fourier transform-infrared (FT-IR) spectroscopy

Continuation of growth on a rough surface causes stressed and defective growth which results in accumulation of hydrogen at dislocations. Coulomb repulsion of hydrogen atom buildup could lead to distortion of lattices and finally discontinuation of epitaxial growth [64]. The FT-IR absorption spectra of the samples show the presence of low amounts of hydrogen in the grown films (Figure 28). The peak at 2000 cm^{-1} is attributed to SiH while 2100 cm^{-1} is attributed to SiH_2 or the surface hydrogen mode at dislocations or grain boundaries. Sample E had 1.215% SiH and 0.251% SiH_2 bonds while sample D had 0.619% SiH and 0.696% SiH_2. This indicates more hydrogen passivation in the grain boundaries of sample D. The other samples showed an order of magnitude less hydrogen content. Sample A which was grown crystalline had 0.034% SiH and 0.058% SiH_2 bonds and sample B, with highest film quality, had 0.024% SiH and 0.025% SiH_2 bonds while sample C which had transition to microcrystalline had 0.043% SiH and 0.055% SiH_2. This shows that samples deposited at epitaxial growth conditions show less hydrogen content. It can be inferred that in balanced growth conditions, hydrogen atoms are either pushed to interstitial sites, such as bond center sites [65], or have been gradually diffused out as a perfect c-Si layer leaves no room for bonded

H atoms. Low surface roughness and low hydrogen content in the c-Si films show that thicker films are achievable at balanced growth condition.

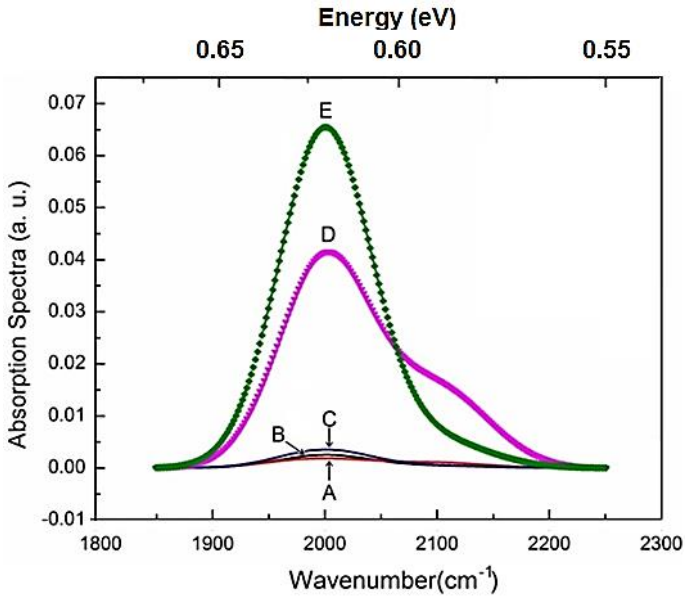

Figure 28. FT-IR absorption spectra of the samples A-E.

3.1.6. Si epitaxy using cold-wall UHV-PECVD system

In the previous sections, epitaxial growth of Si at 250-350 °C was studied using the PECVD chamber of the multi-chamber cluster tool. The parameter space that was taken into account included: 1. plasma power; 2. hydrogen/silane dilution ratio (DR); and, 3. growth temperature. Raman spectroscopy and HR-TEM study of the samples showed achievement of epitaxial growth of intrinsic Si at 250 °C. Successful films were grown at two dilution ratios of 30 and 50, and plasma power densities of 50 and 20 mW/cm^2, respectively. The same technology was transferred to the cold-wall UHV-PECVD system and new sets of runs were performed to enhance the results. In order to increase the growth rate, the role of growth pressure and total flow rate was studied. The results show that doubling the total flow rate from 100 sccm to 200 sccm increased the growth rate by a factor of 5.75.

Figure 29a depicts the Raman spectra of a sample grown at 250 °C with DR of 50 and plasma power density of 20 mW/cm^2. A crystalline Si peak at 520 cm^{-1} is observed without any amorphous peak at 480 cm^{-1}. The crystallinity of the film was confirmed by TEM shown in Figure 29d. Comparison of this sample with the one grown at similar growth conditions in the multi vacuum system shows that increasing the total flow rate from 100 sccm to 200 sccm increased the film thickness from 20 nm to 115 nm. However, it should be taken into account that the growth systems are different. Growth at lower dilution ratios of 30 with higher plasma density also resulted in crystalline films. Figure 29b shows the Raman spectra and Figure 29e depicts the TEM image of the sample.

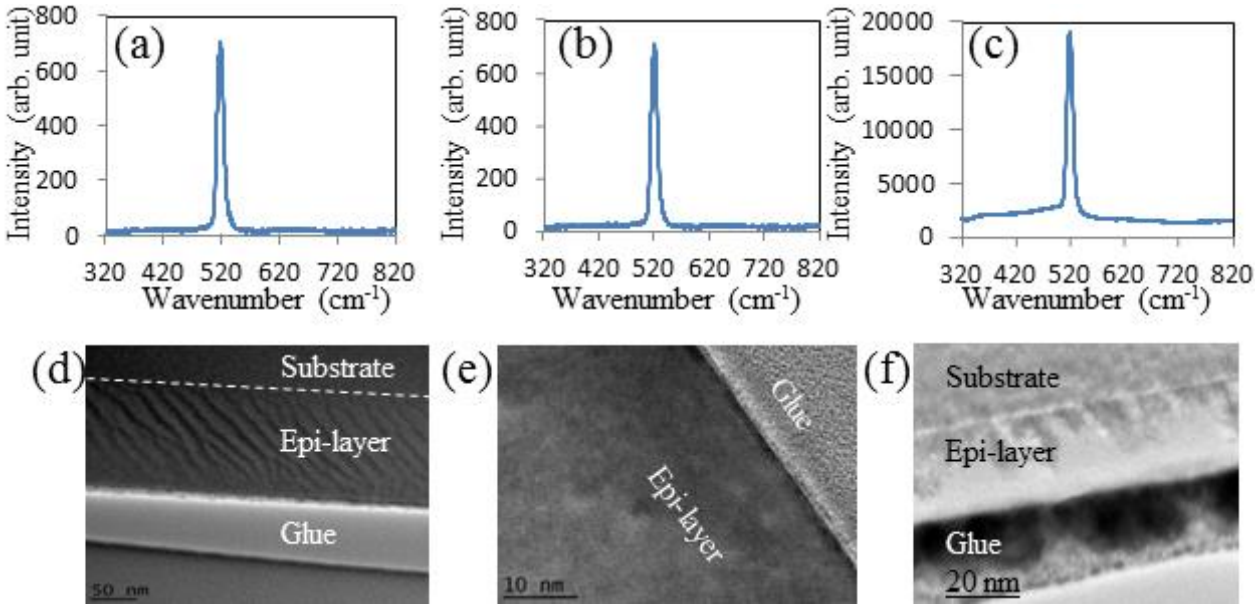

Figure 29. Material characterization results for Si growth at 250 °C and 200 sccm total flow. (a, d) Show the Raman spectra and XTEM image of sample grown at DR:50 and 0.5 torr pressure. Thickness of the layer is 115 nm. (b, e) Show the Raman spectra and XTEM image of sample grown at DR:30 and 0.5 torr pressure. (c, f) Show the Raman spectra and XTEM image of sample grown at DR:30 and 1 torr pressure.

The role of deposition pressure in growth rate was studied by growing the films at different deposition pressures. Change in growth pressure from 0.5 torr to 1 and 2 torr did not

result in fully epitaxial layers. Figure 29c, f shows the result for DR:30, plasma power density 20 mW/cm^{-2}, and deposition pressure of 1 torr. Film thickness was measured to be 40 nm. A decrease in growth rate was observed associated with the role of atomic hydrogen in etching of non-epitaxial films at higher rates than epitaxial ones.

3.2. Germanium and SiGe Epitaxy

Integration of Ge and SiGe active and passive opto-electronic devices in complementary-metal-oxide-semiconductor (CMOS) technology requires a low temperature growth method. Achieving high quality growth at low temperatures is a challenge due to low decomposition rate of silane and germane and lower surface mobility of ad-atoms. Poor crystallinity of the films deteriorates optical efficiency and electronic transport properties of the films. In addition, high lattice mismatch between Si and Ge results in formation of a network of misfit dislocation at the interface and propagation of threading dislocations through the films. Annealing at elevated temperatures has been used to reduce the threading dislocation density (TDD) of the films to ~10^8 cm^{-2}. Furthermore, growth of a sacrificial layer like SiGe or low-temperature (LT) Ge, results in a reduction of threading dislocations through graded lattice change or merging of the defects. High-temperature (HT) Ge growth on top of the sacrificial layer has been shown to achieve TDD on the order of ~10^7 cm^{-2} [66-68].

In this section, a two-step (LT:HT) growth method is adopted for the growth of Ge and the role of pressure and different carrier gases (Ar, N_2, and H_2) is presented. Silicon-germanium films were grown in a single step at 350-450° C and the role of pressure in increasing the material quality and Si incorporation at low temperature growth was studied.

3.2.1. Germanium growth

Figure 30 shows the result of the 2Theta-Omega XRD scan from 004 plane. The peaks located at 69° belong to Si substrate and the peaks observed at 66° belong to Ge epi-layer . All the plots were normalized on the Si peak by dividing the Ge peak intensity by Si peak intensity (Ge/Si peak intensity), so that the Ge peaks could be compared. Comparison of peak intensity and full width at half maximum (FWHM) of the samples grown using H_2 carrier gas show that at 10 sccm H_2 flow rate the FWHM was 0.62°. At flow rates of 25 and 100 sccm, the peaks had lower intensity and higher FWHM, ~2°. Using nitrogen and argon as carrier gas resulted in films with higher intensity and lower FWHM. However, Ge films grown with Ar showed higher intensity in comparison with N_2 and FWHM of 0.1° which was less than half of that of using N_2 carrier gas (0.25°).

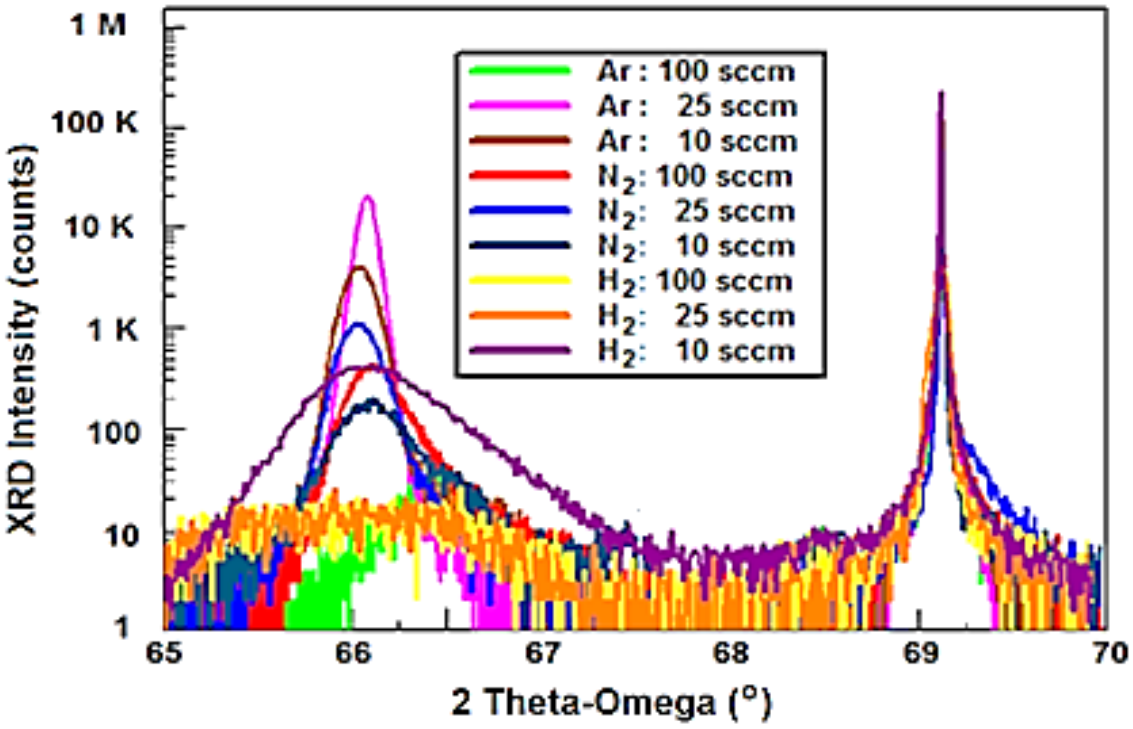

Figure 30. The XRD patterns obtained from (004) plane of the Ge films grown on Si at different flow rates of Ar, H_2, and N_2 carrier gases.

The carrier gases affect the growth by increasing the mobility of Ge ad-atoms on the surface as well as transferring energy through inelastic collision and lowering the activation energy required for decomposition of GeH_4. In addition, carrier gases remove the reaction byproducts and facilitate the growth. The low quality achieved with H_2 could be attributed to the increased partial pressure of H_2 byproduct which pushes back the decomposition reaction for the Ge deposition ($GeH_4 \rightarrow Ge+2H_2$). Higher quality was achieved by Ar and N_2 dilution as compared to the H_2 diluted case, therefore, it may also be attributed to the reduction of H_2 partial pressure on the deposition surface. Due to the weight of Ar (42% greater than N_2), a better surfactant role was observed because increasing the weight led to an increase of momentum and that resulted in increasing the lateral mobility of Ge ad-atoms near the substrate surface. Higher weight of Ar also led to higher transfer of kinetic energy to GeH_4 atoms, which reduced the decomposition activation energy required to break GeH_4. Increased flow rate of Ar and N_2 resulted in poor material quality which was attributed to high dilution of GeH_4 and lack of required Ge ad-atoms.

Figure 31a shows the 2Theta-Omega XRD characterization of the two-step growth (LT:HT) at 0.5 torr. The LT step was kept at 300 °C and the HT step was performed at 500, 550, and 600 °C. Figure 31b and Figure 31c show the change in the FWHM of Ge peaks and normalized Ge peak intensity for different growth pressures (0.1 to 1.0 torr) and HT step temperatures (500 to 600 °C), respectively. The results show that increasing the pressure resulted in higher Ge peak intensity as well as lower FWHM. A large difference was observed between the intensity and FWHM of the growth at 500 °C and the growth at 550 °C and 600 °C at lower pressures. However, the difference was minimized by increasing the pressure to 1.0 torr. Achieving higher Ge intensity and lower FWHM showed that high quality Ge could be

grown at 50 to 100 °C lower temperatures if the pressure was increased from 0.1 to 1.0 torr. The measured thickness of the films grown at 550 °C showed that the film thickness increased from 1188 nm at 0.1 torr pressure to 2734 nm at 1.0. This was mainly due to the increase in the residence time of the precursors in the chamber at higher pressures which led to an increase in the growth rate.

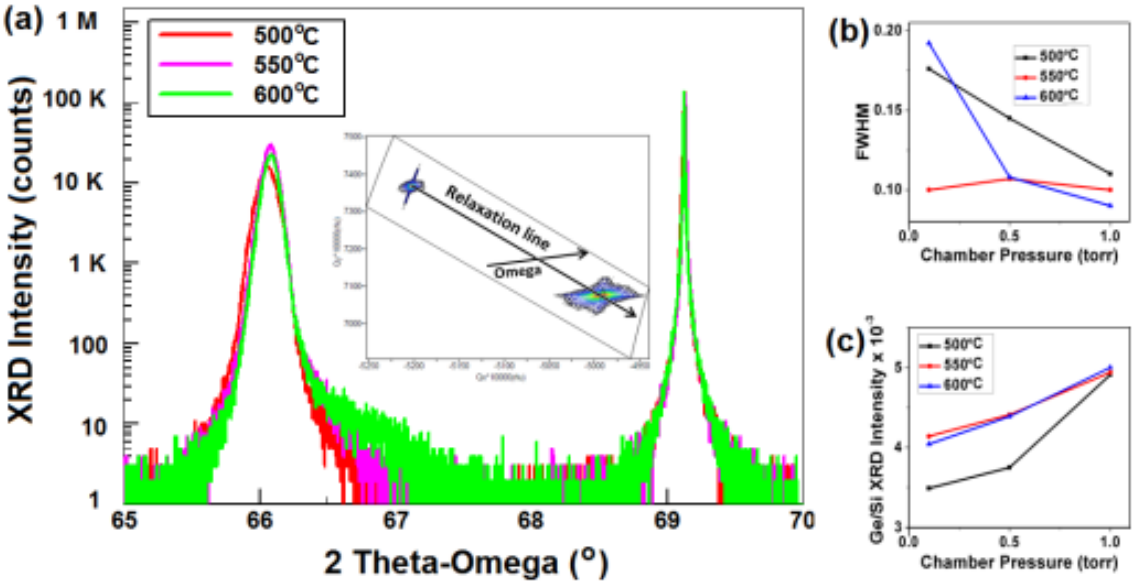

Figure 31. The XRD analysis of Ge films grown in two steps (LT:HT). (a) The XRD patterns of Ge films at fixed GeH_4 and Ar flow rate. RSM of the Ge film grown at 550 °C shows 0.06% tensile strain (inset). (b) FWHM of the peaks was decreased by reduction of temperature and pressure. (c) Ge/Si peak intensity increased by increasing the growth temperature and pressure.

The XRD patterns of the Ge films show that as the growth temperature was increased, the Ge peak position was slightly shifted towards higher angles. Such increase in the reflection angle shows lower out-of-plane lattice constant of the Ge films which indicates that the films were tensile strained. The inset of Figure 31a shows the reciprocal space map (RSM) of the Ge growth at 550 °C indicating 0.06% tensile strain. This was due to 44.8% lower thermal expansion coefficient of Si (2.6×10^{-6} °C^{-1}) in comparison with Ge (5.9×10^{-6} °C^{-1}). When Ge is grown at high temperature the lattice is relaxed on Si at that temperature but when it is cooled

down Si shrinks less than Ge and in-plane lattice constant of Ge remains bigger. Therefore, the Ge layer was tensile strained after it was fully cooled down to room temperature.

3.2.2. Silicon-germanium growth

Figure 32a shows the 2Theta-Omega XRD patterns for SiGe growth at 0.5 torr chamber pressure and from 350 to 450 °C with 1 sccm of SiH_4 flow rate. Increase in the growth temperature resulted in an increase in the normalized SiGe peak intensity and a decrease in its FWHM. Comparison of SiGe FWHM (Figure 32 b) and SiGe counts (Figure 32c) for growth at pressures from 0.1 to 1.0 torr and temperatures of 350 to 450 °C show similar trends for the increase in temperature and pressure. Such similarity indicates that lowering the growth temperature could be compensated by increasing the growth pressure. Figure 32a also shows that the SiGe peak is shifted towards higher angles as the temperature is increased, which indicates that the Si content of the films is increasing.

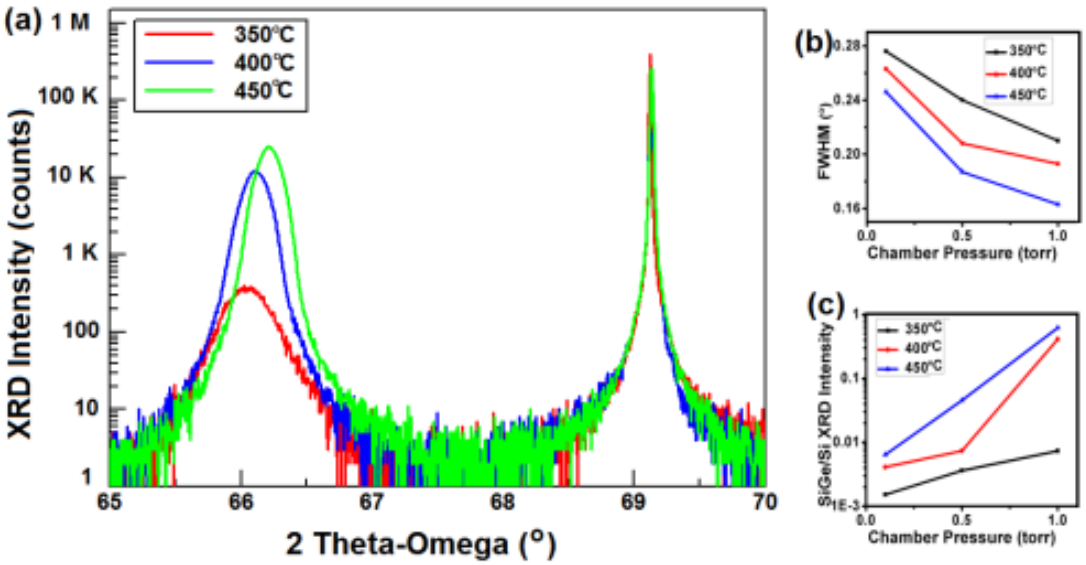

Figure 32. The XRD analysis of SiGe films grown in one step and different temperatures. (a) The XRD patterns of SiGe films at fixed SiH_4 flow rate of 1 sccm (b) FWHM of the peaks was decreased as a result of increase in the temperature and pressure. (c) The intensity of the SiGe/Si peak increased by increasing the growth temperature and pressure.

The mole fraction of Si (x) and Ge $(1-x)$ could be calculated using Vegard's law for binary alloys:

$$a_0^{Si_x Ge_{1-x}} = (1-\mathrm{x})a_0^{\mathrm{Ge}} + a_0^{\mathrm{Si}} - b^{SiGe}\, x(1-x) \qquad \text{(Equation 4)}$$

where $a_0^{Si_x Ge_{1-x}}$, a_0^{Ge}, and a_0^{Si} are the lattice constants of Si_xGe_{1-x}, Ge, and Si, respectively. The bowing parameter of SiGe is taken as b^{SiGe} = 0.026 nm [16]. Silicon composition calculations were performed for different growth pressures and temperatures as shown in Figure 33.

The amount of incorporated Si was found to increase with increasing growth pressure and temperature. Increasing the pressure from 0.1 to 1.0 torr showed that the Si content was almost doubled for all temperature. The increase in low temperature growth (350 °C) is lower than at higher temperatures, which indicates that increasing the Si content needed further increase in growth pressure to compensate the temperature decrease. A similarity in the effect of pressure and temperature in the material quality and Si content of the films was observed. This could be explained as an increase in the residence time at higher pressure causing an increase in SiH_4 decomposition rate.

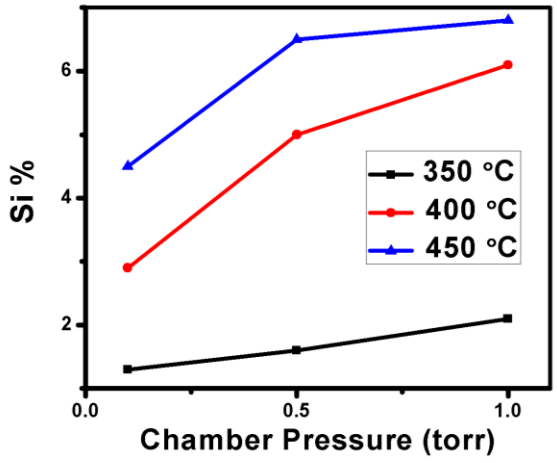

Figure 33. Increase in the Si incorporation in Ge lattice as a result of increase in the growth temperature and pressure at fixed SiH4 flow rate of 1 sccm.

Increasing SiH_4 flow from 1 sccm to 4 sccm resulted in higher Si incorporation while decreasing the normalized SiGe counts as well as increasing FWHM of the peak. Figure 34a shows the XRD patterns for SiGe growth with different SiH_4 flow rates. The RSM of SiGe film in the inset of Figure 34a shows that the film was relaxed. The broadening of the SiGe peak in the omega direction showed lower quality of the film as Si content was increased. Figure 34b shows the changes in SiGe/Si counts as well as the FWHM of the SiGe peak which was consistent with RSM results.

Higher growth temperature was required to keep high quality SiGe growth for higher SiH_4 flow due to higher activation energy for chemisorption of SiH_4 molecules in comparison with GeH_4. In addition, lower surface mobility of Si ad-atoms caused a reduction in the quality of SiGe film.

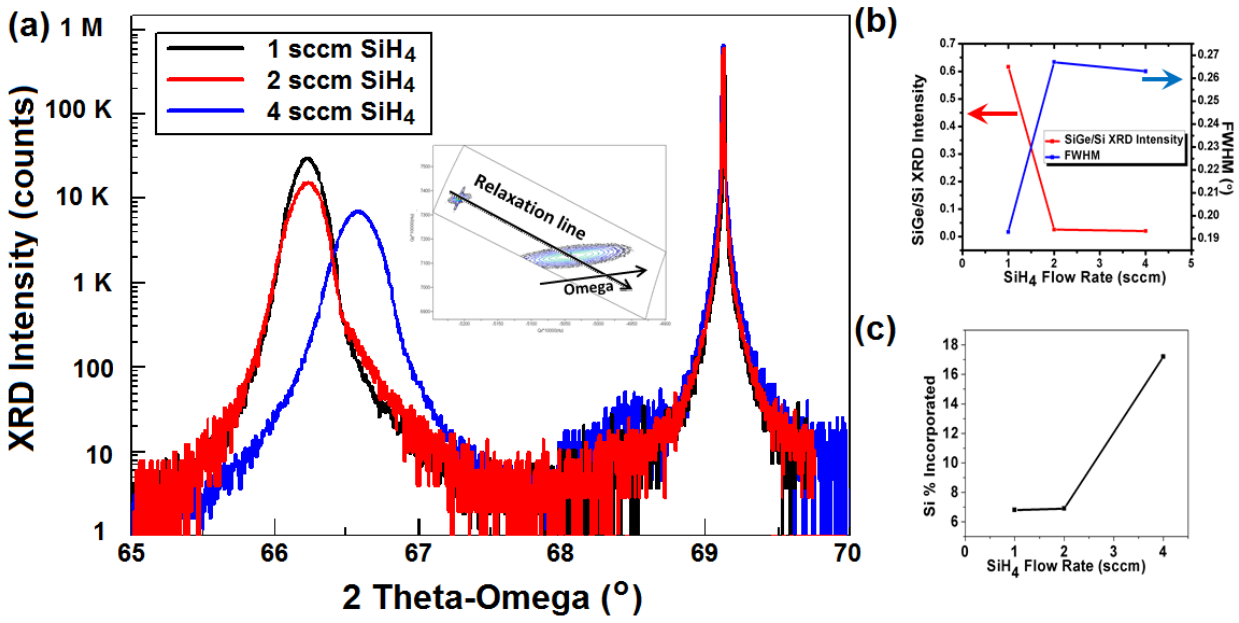

Figure 34. The XRD analysis of SiGe films grown in one step and different flow rates. (a) The XRD patterns SiGe films for different SiH_4 flow rates of 1, 2 and 4 sccm.The inset is the RSM of sample grown with 4 sccm flow rate of SiH_4 (b) An increase in the FWHM and a decrease in the intensity of the peaks was observed as a result of an increase in SiH_4 flow rate. (c) Si incorporation was increased at higher SiH_4 flow rates.

3.2.3. TEM and SEM characterization of Ge and SiGe

Figure 35a displays the TEM characterization results of the Ge films which shows high material quality was achieved in the two-step growth method using Ar carrier gas. In order to compare the effect of a single step growth with a two-step growth, the TEM of a Ge layer that was grown at 550 °C without growing the Ge buffer layer at 300 °C is shown in Figure 35b. In addition, the TEM image of a two-step growth of Ge using H_2 carrier gas is presented in Figure 35c. The threading dislocation density of the two-step Ge growth using Ar was measured to be as low as 1.3×10^7 cm^{-2}. A single step growth increased the TDD to 8.5×10^8 cm^{-2} and the growth using hydrogen also resulted in highly defective film with a TDD average of 5.0×10^8 cm^{-2}.

The TDD of the Ge films was determined using etch pit measurement and compared with the results achieved from TEM measurement. The comparison of TDD using TEM (1.3×10^7 cm^{-2}) and etch pit measurements (1.7×10^7 cm^{-2}) for Ge films confirmed the accuracy of the measurements.

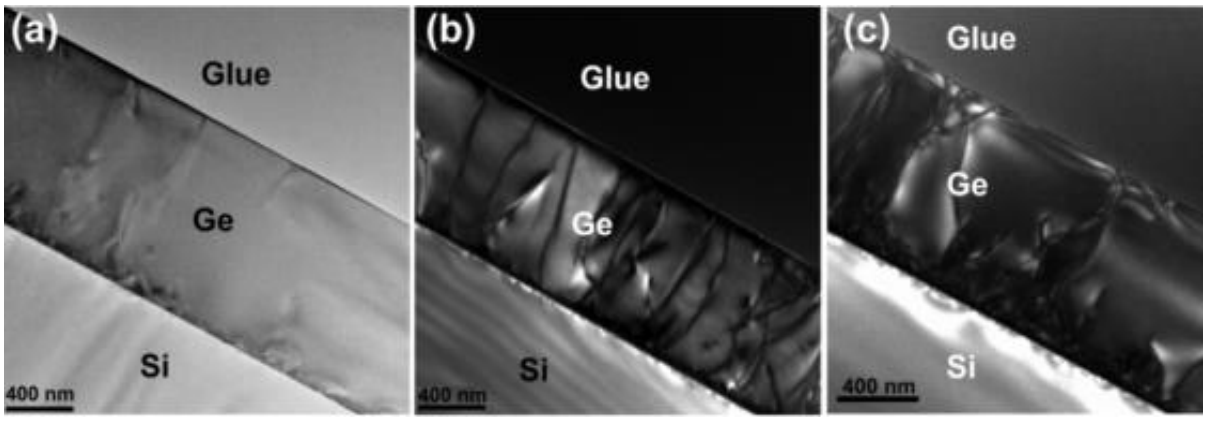

Figure 35. TEM micrograph of the Ge films grown at different growth conditions (a) Two-step (LT: 300 °C, HT:550 °C) growth using Ar carrier gas. b) Single-step growth at 550 °C using Ar carrier gas (c). Two-step (LT:300 °C, HT:550 °C) growth using H_2 carrier gas.

Figure 36 compares the SEM images of Ge and SiGe films with their SEM images after etching in cold Schimmel solution. The solution was prepared by mixing 55% of CrO_3 (0.4 M) and 45% HF (49%) and it was cooled down to 2 °C [69]. Threading dislocations reach the surface and form small edges that have higher surface energy. Therefore, they are etched faster in the solution and leave a pit behind. Threading dislocation density for SiGe was 2.3×10^7 cm^{-2}. The lower TDD for Ge growth is attributed to using two steps for Ge growth (LT and HT growth).

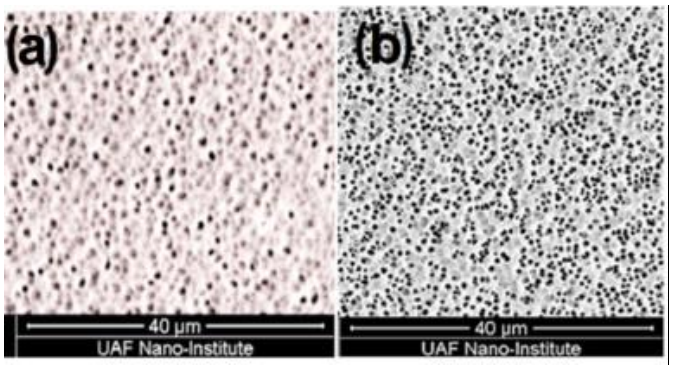

Figure 36. SEM images after decorating the threading dislocation using Schimmel solution. (a) Two-step (LT: 300 °C, HT:550 °C) growth using Ar carrier gas. (b) $Si_{0.17}Ge_{0.83}$ film grown at 450 °C.

3.2.4. Conclusion

In conclusion, Ge films were grown using a two-step (HT:LT) growth method with GeH_4 and different carrier gases (Ar, H_2, and N_2). Higher quality films were achieved using Ar as the carrier gas. Reduction in FWHM and an increase in Ge peak intensity indicated achievement of higher quality films as the temperature in the HT step was increased. A similar trend was observed when a fixed SiH_4 flow rate was introduced to form SiGe alloys. Incorporation of Si was increased at higher temperatures and pressures. Although an increase in the SiH_4 flow rate resulted in higher Si incorporation, lower quality material resulted at fixed

growth temperature. An increase in the growth pressure from 0.1 to 1.0 torr could compensate for the reduction in material quality as a result of ~100 °C lower growth temperature. Analysis of SEM images showed achievement of TDD of 1.7×10^{7} cm^{-2} for a two-step (LT: 300 °C, HT:550 °C) growth using Ar as a carrier gas. Scanning electron micrographs showed similar results as TEM for the measurement of the TDD after placing the samples in cold Schimmel solution. The $Si_{0.17}Ge_{0.83}$ film had a TDD of 2.3×10^{7} cm^{-2}.

Chapter 4. GeSn and SiGeSn growth using $SnCl_4$ precursor

4.1. GeSn growth using $SnCl_4$

Growth of $Ge_{1-x}Sn_x$ films via CVD has been reported by different groups. The early results of CVD growth at ASU showed the ability to grow $Ge_{1-x}Sn_x$ film directly on Si using a hot-wall UHV-CVD system with SnD_4 as the Sn precursor along with different chemistries of germanium precursor [70]. Due to the high cost and instability of SnD_4, other precursors such as stannic chloride have been explored [40, 41]. Films were grown using a high cost Ge precursor (Ge_2H_6) and carrier gases on a Ge buffered Si substrate. Mantl *et al.*, demonstrated direct growth of $Ge_{1-x}Sn_x$ on Si using showerhead [42] technology in a reduced pressure CVD chamber by employing $SnCl_4$ and Ge_2H_6 precursors and carrier gases. In this chapter, direct growth of strain-relaxed $Ge_{1-x}Sn_x$ films on Si substrates is presented. The samples are grown using stannic chloride and germane as low-cost and commercially available precursors.

4.1.1. Growth method

The growth of $Ge_{1-x}Sn_x$ films was achieved without using any carrier gases and buffer layers. The experiments were carried out at reduced pressures of 0.1, 0.3, 0.5, 0.75, 1.0, 1.50, and 2.0 torr and at temperatures as low as 300 °C. Germane and $SnCl_4$ were used as the precursors for $Ge_{1-x}Sn_x$ growth. The gas flow ratio ($GeH_4/SnCl_4$) was set to 5, 3.3, 2.5 and 1.6. Depending on the growth parameters such as gas flow ratio and deposition pressure, a growth rate of 3.3 to 20 nm/min was achieved.

4.1.2. Material characterization

The 2Theta-Omega XRD scan was performed from the symmetric (004) plane to obtain the out-of plane lattice constant of the $Ge_{1-x}Sn_x$ films. Figure 37a shows the peak at 69°

corresponding to a satisfaction of the Bragg condition by Si (001) substrate, and the peaks at lower angles of 66-65° due to larger lattice size of the $Ge_{1-x}Sn_x$ layers. The difference in the position of $Ge_{1-x}Sn_x$ peaks was due to the difference in the Sn mole fractions of $Ge_{1-x}Sn_x$ layers. Different compositions were achieved from 1% to 7% with desirable crystal quality. The $Ge_{1-x}Sn_x$ peaks were broadened due to the presence of mosaicity in the GeSn crystal and formation of defects as a result of strain relaxation. The FWHM of the $Ge_{1-x}Sn_x$ peaks was between 0.28 for 1%-Sn film and 0.36 for 7%-Sn film. However, there was no trend showing that the FWHM of the peaks changed as the Sn composition was increased.

In order to calculate the total lattice constant and the strain in the film, an asymmetric RSM from (-2 -2 4) plane was performed. The RSM scans provided measurement of the in-plane ($a_{||}$) and out-of-plane ($a_{\perp}$) lattice constant of $Ge_{1-x}Sn_x$ alloys. The total lattice constant a_0^{GeSn} was calculated by taking into account the elastic constants of $Ge_{1-x}Sn_x$ [71]. Knowing the total lattice constant, the Sn mole fractions were calculated through Vegard's law with the bowing factor of b = 0.0166 Å [72]. Figure 37b shows the RSM of a 6% Sn sample. The x-axis shows Q_z in reciprocal lattice unit (rlu) which is related to the out-of-plane lattice constant (L); the y-axis shows Q_x which is related to the in-plane lattice constant (H or K). The direction of the spread in the $Ge_{0.94}Sn_{0.06}$ peak does not show a compositional gradient in the sample because it was related to the relaxation of the lattice on Si substrate. Large lattice mismatch between Si and GeSn is the main reason for a large spread in the omega direction. The relaxation line in Figure 37b shows that the film was relaxed; if the peak was above the line it was tensile strained, if it was below the line the films was compressively strained. The $Ge_{0.94}Sn_{0.06}$ peak was observed to be on the relaxation line and the relaxation was measured to be 97%.

Calculation of total strain in other samples showed that all the films were more than 95% relaxed. Table IV shows the lattice constants of the $Ge_{1-x}Sn_x$ alloys, their Sn mole fraction and strain relaxation percentage. $Ge_{1-x}Sn_x$ films were almost fully relaxed mainly due to large lattice mismatch between Si (5.431 Å) and $Ge_{1-x}Sn_x$ (above 5.658 Å) and small critical thickness [73]. The other reason for relaxation of Ge (and similarly $Ge_{1-x}Sn_x$) films on Si is the thermal mismatch between these two materials. High temperature growth (above 500 °C) and rapid cool down has been the main method for achieving tensile strained Ge on Si [74].

The $Ge_{1-x}Sn_x$ samples were grown at 300 °C for 30 minutes and the thermal mismatch between Si and $Ge_{1-x}Sn_x$ may have helped relax the compressive strain. The strain was mainly relieved through formation of misfit dislocations including Lomer misfit dislocations. The cross-sectional TEM image in Figure 37c shows formation of such dislocations at the $Ge_{1-x}Sn_x$/Si interface. In addition, Figure 37b shows that strain relaxation occurred by formation of misfit dislocations at the interface. The TEM image shows that the grown film was fully epitaxial. Film thickness of the samples is listed in Table IV.

The SEM scan/EDX spectra of the samples show surface morphology of the sample as well as Sn incorporation in the Ge matrix. The EDX spectra in Figure 37d show the presence of Ge, Si, and Sn in the $Ge_{.94}Sn_{.06}$ film. Due to the high count collection of secondary electrons from the substrate, the ratio of Sn and Ge cannot exactly reveal the percentage of Sn in Ge. The presence of carbon and oxygen in the EDX spectra was mainly due to the contamination and oxidation of the film after exposure to ambient air. The EDX maps for Ge (Figure 37e) and Sn (Figure 37f) display uniform incorporation of Sn. The SEM image shows continuous growth of $Ge_{1-x}Sn_x$ without observation of locally crystalline patches. No segregation and precipitation of Sn was observed on the films which indicated robust and stable growth of the films.

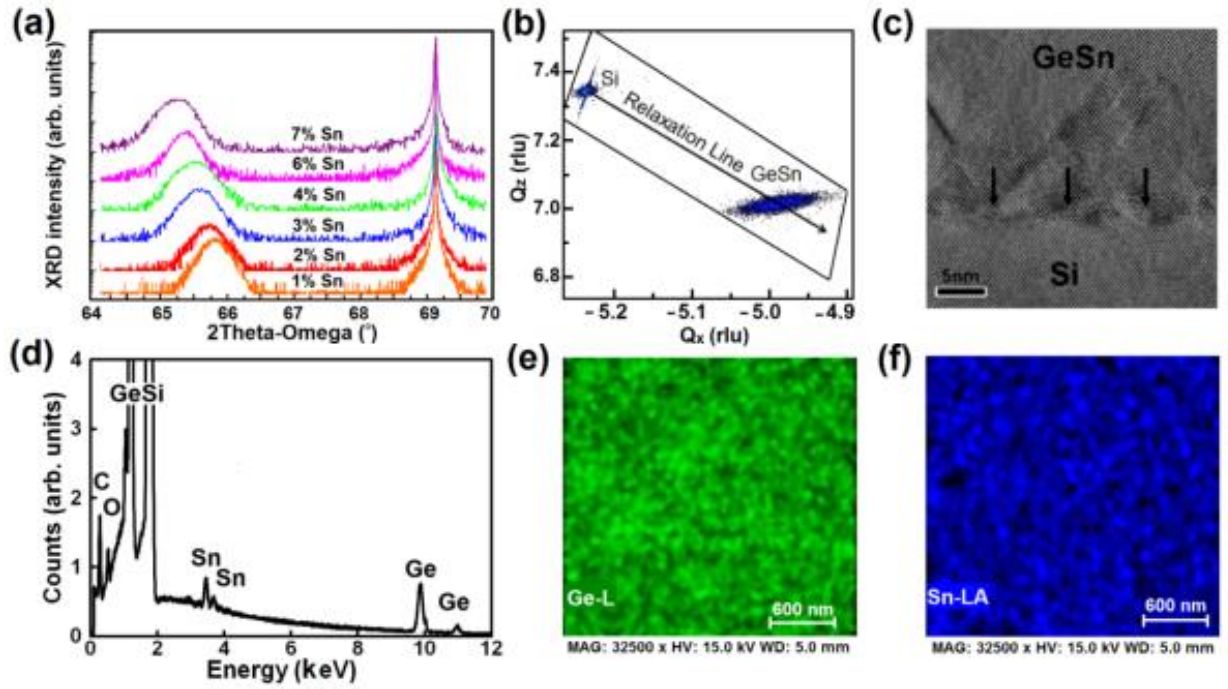

Figure 37. Material characterization of $Ge_{1-x}Sn_x$ films on Si. (a) The XRD pattern of $Ge_{1-x}Sn_x$ films on a Si substrate. (b) The RSM from asymetrical plane (-2 -2 4) for $Ge_{0.94}Sn_{0.06}$. (c) The TEM image of $Ge_{.94}Sn_{.06}$ film. (d) The EDX spectrum of Si/$Ge_{.94}Sn_{.06}$ film. (e) The EDX surface maps of Ge and (f) Sn taken from scanning electron micrographs of $Ge_{.94}Sn_{.06}$ film.

Table IV. Tin mole fraction, lattice constant and relaxation percentage of GeSn films.

Sample #	Sn%	$a_{\parallel}$ (nm)	$a_{\perp}$ (nm)	a (nm)	Relaxation %	Thickness (nm)
1	1.2	5.666	5.671	5.668	98%	615
2	2.1	5.673	5.679	5.676	98%	423
3	2.9	5.678	5.687	5.682	97%	295
4	4.2	5.689	5.695	5.692	98%	207
5	5.8	5.699	5.712	5.706	97%	108
6	7.0	5.715	5.719	5.717	99%	532

4.1.3. Growth mechanism

Growth of $Ge_{1-x}Sn_x$ on a Si substrate requires understanding the reactions and their byproducts. Stannic chloride has a tendency to etch Ge due to the presence of chlorine. The byproduct of GeH_4+$SnCl_4$ reaction is HCl which is an etchant gas for germanium and silicon [75]. The following reactions show different mechanisms of film deposition as well as HCl production in the chamber:

$$GeH_4 \rightarrow Ge + 2H_2 \quad \text{(Equation 5)}$$

$$2H_2 + SnCl_4 \rightarrow Sn + 4HCl \quad \text{(Equation 6)}$$

$$GeH_4 + SnCl_4 \rightarrow Ge + Sn + 4HCl \quad \text{(Equation 7)}$$

Higher substrate temperature results in a higher density of depositing ad-atoms (Ge and Sn); however, it will also result in production of HCl at a higher rate. In addition, a higher flow rate of $SnCl_4$ increases the production rate of HCl as well. Controlling the temperature and flow rate of the gases could control the process so that growth is the dominant process in the chamber. The Ge/Sn film will be etched by HCl through the following reactions:

$$4HCl + Ge \rightarrow GeH_4 + 2Cl_2 \quad \text{(Equation 8)}$$

$$4HCl + Sn \rightarrow SnCl_4 + 2H_2 \quad \text{(Equation 9)}$$

Predominance of etching over growth is the main mechanism that prevents direct growth of $Ge_{1-x}Sn_x$ on Si. By controlling the flow through the MFCs, we have grown $Ge_{1-x}Sn_x$ films on Si at different pressures with a fixed flow ratio of $GeH_4/SnCl_4$ = 1.6. Growth was observed at 0.1 torr of deposition pressure and continued until the deposition pressure increased to 1.0 torr. Figure 38a shows the thickness of $Ge_{1-x}Sn_x$ films versus deposition pressure of the chamber as

well as Sn incorporation percentage. Incorporation of Sn in the Ge lattice was increased by raising the pressure due to the higher residence time of the precursors in the chamber. The residence time of the gases increased from 2 s at 0.1 torr to 19 s at 1.0 torr. Meanwhile, HCl etched more of the $Ge_{1-x}Sn_x$ films during deposition at higher pressures. This trend continued to 1.0 torr and no growth was observed at 1.5 and 2.0 torr. The increase in Sn composition from 1% to 6% was accompanied with a reduction in the thickness from 615 nm to 108 nm. Films that were expected to have higher than 6% Sn content were not even deposited. Therefore, in order to grow higher Sn content films, the growth mechanism under fixed pressure and changing $SnCl_4$ flow was studied. Higher film thickness and higher Sn incorporation was achieved as a result of the predominance of growth over etching. Figure 38b shows Sn incorporation in $Ge_{1-x}Sn_x$ films versus $SnCl_4$ flow rate at 0.75 torr deposition pressure. The secondary axis of Figure 38b shows film thicknesses of the samples. Due to the predominance of etching for higher $SnCl_4$ flow rate, the films were mostly etched and the film thickness was less than 100 nm.

Introduction of carrier gases has different effects on the growth of $Ge_{1-x}Sn_x$ films. Hydrogen changes the balance in the reaction to produce more HCl. Consequently, the $GeH_4/SnCl_4$ ratio at which the $Ge_{1-x}Sn_x$ films were depositing did not result in growth when hydrogen was introduced in the chamber. In addition, introduction of nitrogen and argon as carrier gases reduced the activation energy of the growth [42]. Although reduction of activation energy enabled easier breakdown of the molecules on the surface and enhanced the growth quality and growth rate, it prepared the conditions for easier etch due to the presence of an etchant agent. Therefore, the presence of carrier gases pushed the competition between growth and etching towards etching, resulting in no film growth at even low flow rates of carrier gases.

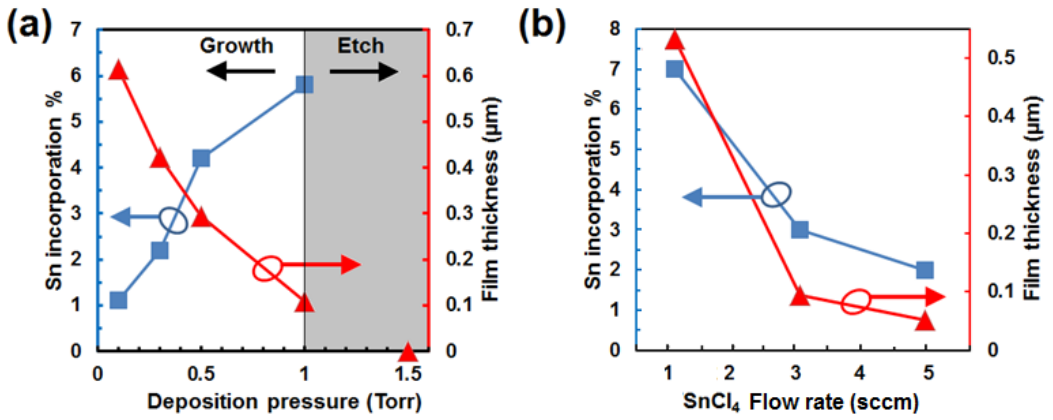

Figure 38. Growth mechanism of GeSn films on Si at different growth pressures and flow rates. (a) Variation of Sn incorporation percentage versus deposition pressure. Films were etched away for deposition pressures higher than 1 torr. The secondary axis on the right shows the reduction of film thickness as a result of increase in the deposition pressure. (b) Tin incorporation and film thickness of the samples grown at 0.75 torr growth pressure versus $SnCl_4$ flow ratio.

4.1.4. Raman spectroscopy

The $Ge_{1-x}Sn_x$ films were further investigated by Raman spectroscopy in order to analyze the crystal structure. Room temperature Raman spectra of the grown samples as well as a Ge reference sample are plotted in Figure 39a. The measurement was done using a green laser (wavelength: 532 nm). The Ge-Ge longitudinal optical (LO) peak was observed at 300 cm^{-1} for the Ge reference sample while the Ge-Ge peak in the $Ge_{1-x}Sn_x$ films was shifted to lower wavenumbers due to the change in bond energy of Ge-Ge by incorporation of Sn atoms. The intensity of the Ge-Ge LO peak at 300 cm^{-1} is normalized for all the samples for comparison of the peak positions. In addition to the main Ge-Ge peak, the Raman spectra of $Ge_{1-x}Sn_x$ films show other peaks that were induced as a result of Sn incorporation. The Ge-Sn LO peaks for different Sn mole fractions were observed at 250-260 cm^{-1} in the films. A second peak of Ge-Sn was observed at 285 cm^{-1}, which can be seen as a shoulder of Ge-Ge main peak.

The peak positions were obtained by Lorentzian fitting to find the exact position for further analysis. The shift in the Ge-Ge LO peak position depends on both strain and Sn composition of the films. Theoretical calculations for the change in Ge-Ge peak position ($\Delta\omega$) are different for relaxed films and strained films for different Sn (x) content ($\Delta\omega_{Ge-Ge}(x) = bx\ cm^{-1}$). The Ge-Ge peak is expected to shift by a factor of b = -30.30 for a strained alloy while this factor varies to b = -83.10 for a strain relaxed film [76]. Figure 39b shows the experimental data obtained for Ge-Ge and Ge-Sn Raman shift from the sample compared with the theoretical calculations. The peak shifts match well with the theoretical calculations for strain relaxed films.

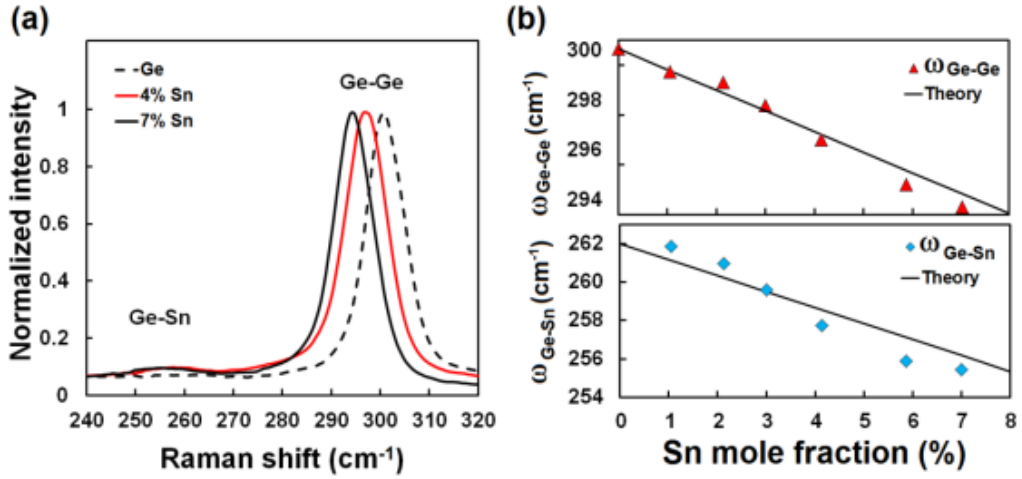

Figure 39. Optical charactrization of the $Ge_{1-x}Sn_x$ samples using Raman spectroscopy. (a) Raman spectra of the $Ge_{1-x}Sn_x$ film grown on a Si substrate. (b) Ge-Ge and Ge-Sn peak shifts vs. Sn mole fraction. The solid symbols are experimental data and the lines are theoretical predictions for relaxed films.

4.1.5. Photoluminescence (PL)

A 690 nm Ti-Sapphire high power femtosecond laser and a PbS detector were used for PL measurement of the samples. The PL measurements on $Ge_{1-x}Sn_x$ samples allow determination of the bandgap edge for various Sn compositions. Figure 40 depicts room

temperature PL intensity spectra for as-grown $Ge_{1-x}Sn_x$ films with 2%, 4%, 6% and 7% Sn mole fractions. As indicated in Figure 40a, an increase of the Sn mole fraction resulted in a bandgap reduction. Both direct and indirect PL peaks exhibited red-shift with Sn composition increases from 2% to 7%. A Gaussian fitting function was employed to extract the PL peak positions of both direct and indirect transitions as described in reference 14. In $Ge_{0.94}Sn_{0.06}$ and $Ge_{0.93}Sn_{0.07}$ samples, the energy differences between direct and indirect transitions are very small; therefore, the PL emissions from these indirect and direct transitions could not be identified. The PL peaks from the samples with 2%, 4%, 6%, and 7% Sn compositions are shown in Figure 40b as solid symbols. The solid and the dashed lines show the direct and indirect bandgap energies, respectively, based on bowed Vegard's law for the relaxed $Ge_{1-x}Sn_x$ alloy [14]. Since the $Ge_{1-x}Sn_x$ films were almost strain-free, as confirmed by XRD measurements, the experimental results closely followed the predicted values from Vegard's law.

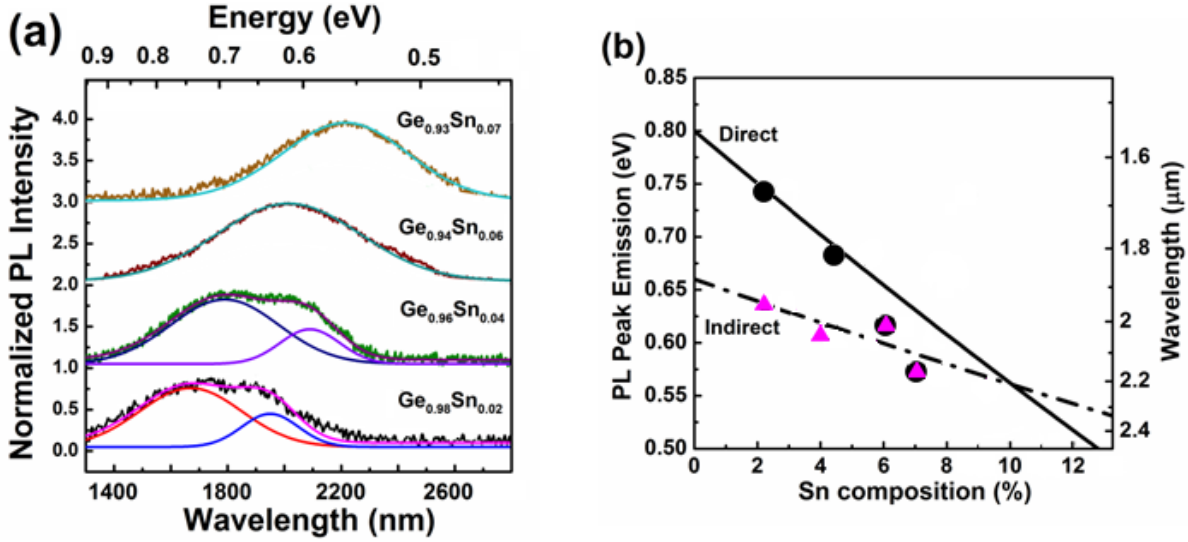

Figure 40. Optical charactrization of the $Ge_{1-x}Sn_x$ samples using photoluminescence spectroscopy. (a) The PL specra of the $Ge_{1-x}Sn_x$ films with 2, 4, 6, and 7% Sn mole fraction showing a red shift in the bandgap of the films. (b) The experimental data along with the theoretical calculations of direct (solid line) and indirect bandgap (dash line) of $Ge_{1-x}Sn_x$ alloy for different Sn compositions.

4.2. Enhancement of material quality of GeSn films using Ar

Growth of GeSn films using $SnCl_4$ is greatly affected by the role of reaction byproducts during deposition of the films. Etching of the Si substrate with the production of HCl in the GeH_4+$SnCl_4$ reaction has been the one of the main reasons for the growth of a Ge buffer layer prior to the GeSn growth. In the reported GeSn growth using $SnCl_4$ on Ge buffered substrate, H_2 and N_2 have been used as carrier gases [42, 77]. Elimination of carrier gas has enabled direct growth of GeSn material on Si substrate as discussed in Section 4.1; nonetheless, enhancement of film quality requires introduction of the carrier gas or increase in the growth temperature. In this section, the effect of carrier gases on improving the material quality and optical properties of the films grown at different temperatures and pressures is presented.

4.2.1. Growth method

The GeSn films were grown with Ar carrier gas at various chamber pressures of 0.1, 0.5, and 1 torr and substrate temperatures of 300, 350, and 400 °C. Germane and Ar flow rates were fixed at 10 and 25 sccm, respectively.

4.2.2. Growth mechanism

The main challenge in using $SnCl_4$ as the Sn precursor is the etching behavior of $SnCl_4$ due to formation of HCl in the chamber as was shown in Section 4.1.3. In the growth without the buffer layer (Section 4.1), $SnCl_4$ flow rates above 5 sccm (GeH_4 =10 sccm) resulted in no film growth. An increase in the growth temperature above 300 °C or introducing gases (Ar or N_2) led to no film growth which was interpreted as achieving equal growth and etching rates. Etching rate in H_2 ambient is greater as H_2 promotes formation of HCl indicated in Equation 6. In a separate run, a Ge layer of 1 μm thickness was etched at a rate of ~100 nm/min at 300 °C

with $H_2/SnCl_4$ ratio of 20. In order to suppress the etching and increase the material quality using a carrier gas, lower flow rates (0.3 to 0.5 sccm) of $SnCl_4$ and higher growth temperature were used. Argon was used as the carrier gas to reduce the partial pressure of hydrogen on the surface thereby reducing film etching.

4.2.3. Material characterization

Figure 41a shows the XRD pattern from (004) plane of GeSn films with and without Ar carrier gas. After normalizing the Si peaks, the GeSn peaks were compared. The intensity of the GeSn peak showed an increase by approximately one order of magnitude after adding Ar as the carrier. In addition, FWHM of the GeSn peaks decreased from 0.31 to 0.24 degrees. Figure 41b and c compares the typical TEM of GeSn samples grown without and with Ar carrier gas, respectively. The enhancement in the quality of material is observed by comparing the two figures. A higher density of threading dislocations and stacking faults was observed in the growth without Ar carrier gas. The asymmetrical RSM scan of the samples from (-2-24) plane show that samples were strain relaxed but the GeSn peak in the growth without Ar carrier gas had lower intensity. The spread observed in the omega direction was due to the mosaicity of the film as a result of strain relaxation. The comparison between the RSMs of samples without (Figure 41d) and with (Figure 41e) Ar carrier gas showed larger mosaic spread for the growth without Ar carrier gas.

4.2.4. Optical characterization

Photoluminescence

A 690 nm Ti:sapphire laser was used for excitation and a liquid-nitrogen-cooled extended InGaAs detector (cutoff at 2.3 μm) was used for light detection. Figure 42 shows PL characterization of the GeSn samples grown with and without Ar at 300 °C and 350 °C. The

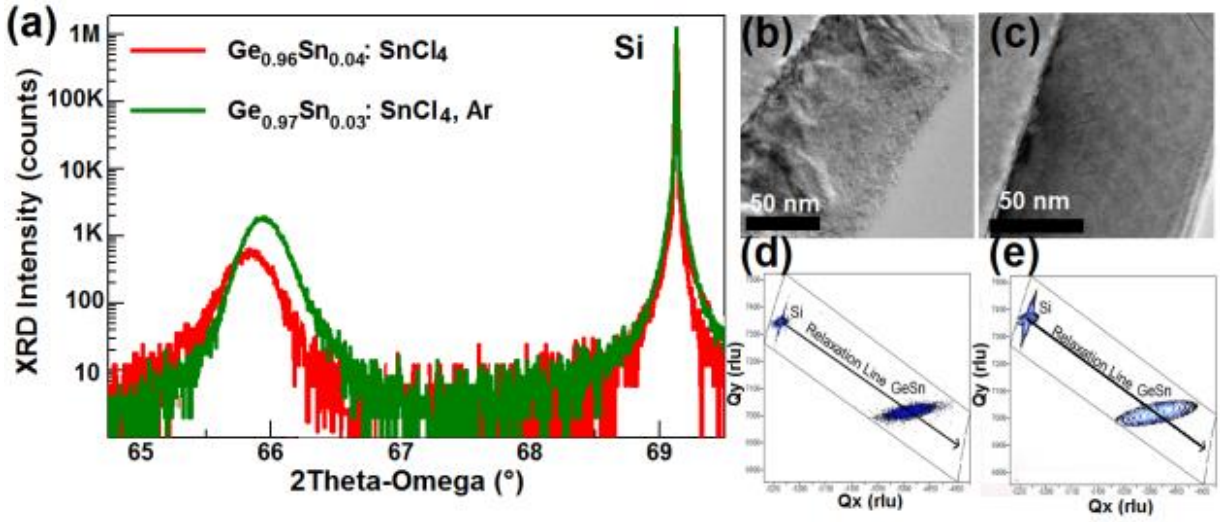

Figure 41. Material characterization of GeSn films grown with and without Ar carrier gas. (a) 2Theta-Omega XRD scan of the GeSn samples. (b) Cross sectional TEM image of GeSn film grown without and (c) with Ar carrier gas. (d) The RSM scan of GeSn film grown without and (e) with Ar carrier gas.

growth pressure was kept at 0.5 torr for all samples. The PL intensity of the material grown at 300 °C without a carrier gas showed higher intensity than the one grown with Ar. However, no growth was observed above 300 °C without Ar carrier gas. For GeSn growth at 350 °C with Ar carrier gas, approximately three times higher intensity was observed which indicates higher quality of the grown material. This increase in the material quality could be attributed to higher mobility of Ge ad-species at higher temperatures and the role of Ar carrier gas to act as a surfactant to further increase the surface mobility due to its large atomic size. The PL peak positions of all samples were shifted from the Ge characteristic indirect peak at 1550 nm towards longer wavelengths. This shift indicated incorporation of Sn in Ge lattice.

The comprehensive study on the growth at different temperatures and pressures showed that GeSn material growth using Ar as carrier gas was possible at temperatures higher than 300 °C. Figure 43a shows the PL measurement of the $Ge_{0.98}Sn_{0.02}$ films a at growth pressure of 0.5 torr. The integrated PL intensity and peak position of the growth at different pressures and

temperature are shown in Figure 43b and c, respectively. Due to the low intensity PL spectra for the growth at 300 °C, the peak position was not taken into account for comparison.

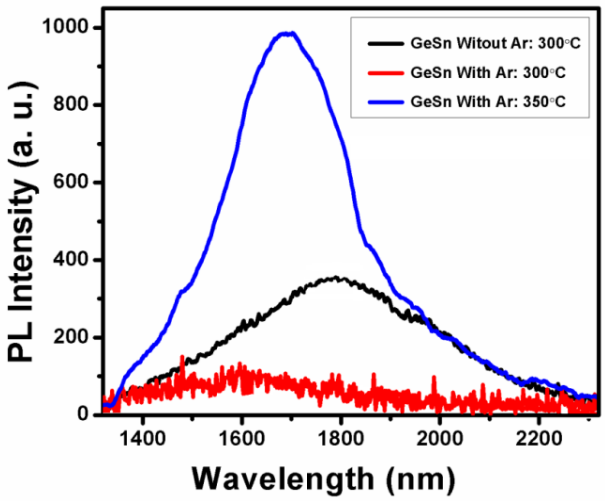

Figure 42. Comparison of PL emission from samples grown with and without Ar carrier gas.

Figure 43 b shows an increase in the PL intensity as the growth temperature was increased from 300 to 400 °C. This could be attributed to higher mobility of Ge ad-species on the surface at higher temperatures. It also shows that the PL intensity increased as the growth pressure was increased from 0.1 to 0.5 torr. However, the intensity decreased at 1 torr growth pressure. Comparison of the PL peak positions shows that the peak position was increased by increasing the growth pressure from 0.1 to 0.5 torr. The PL peak position neither increased (nor decreased) significantly by further increasing of the growth pressure to 1 torr.

The peak shift in the PL spectra was due to the incorporation of Sn in the Ge lattice. Higher Sn incorporation resulted in larger shift in the peak towards the higher emission wavelengths. The position of the peaks could also be shifted by the film strain but the XRD measurement of the films showed that samples were more than 95% strain relaxed. Therefore, the shift in the peak position was only due to Sn incorporation in the films. An increase in the

growth pressure caused a reduction in the PL intensity while the Sn incorporation was kept unchanged. On the other hand, it was observed that an increase in the growth temperature from 300 to 400 °C had directly affected the material quality. Higher growth temperature led to higher Ge material quality; however, due to instability of Sn in the Ge lattice, growth temperatures beyond 400 °C are not recommended [78]. Increase in the growth pressure resulted in higher Sn incorporation as higher pressure increased the collision frequency and residence time of the molecules. Increased molecular collision led to higher momentum transfer between the atoms and easier decomposition of GeH_4 and $SnCl_4$. Due to lower bond energy of $SnCl_4$ molecule than GeH_4, more of the $SnCl_4$ decomposed and higher Sn could be incorporated in the film [20]. This phenomenon could explain the increase in the peak shift of the GeSn films at higher pressures. Increase in $SnCl_4$ decomposition resulted in production of more HCl which is a film etchant and could lower the material quality and cause a reduction in PL peak intensity.

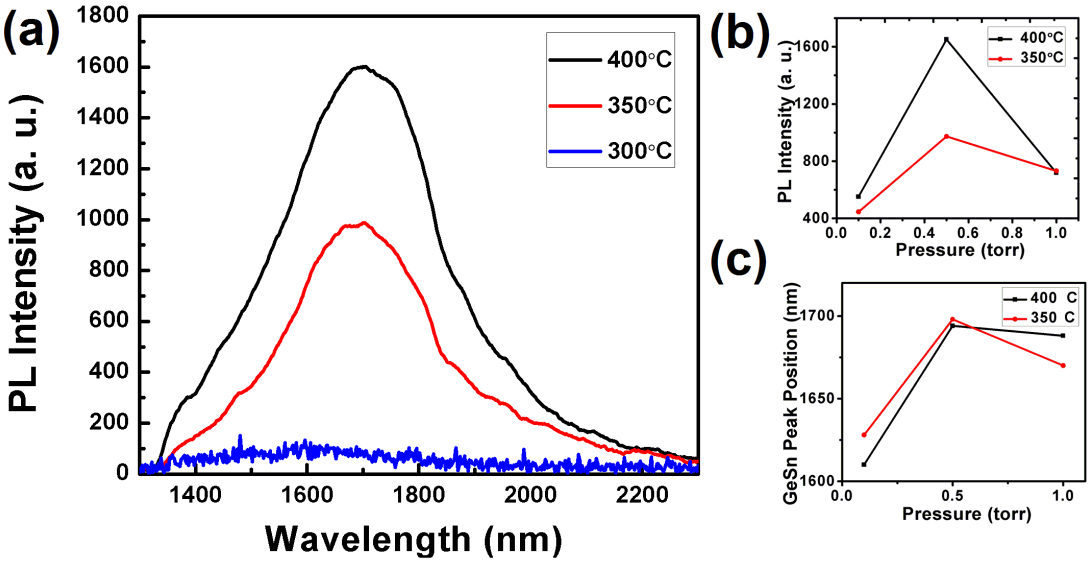

Figure 43. Optical charactrization of the GeSn samples using PL spectroscopy. (a) The PL emission of the samples grown with Ar carrier gas at 300 to 400 °C. Change in PL intensity (b) and PL peak position (c) by increasing the pressure from 0.1 to 1 torr.

Ellipsometry

The spectroscopic ellipsometry characterization tool was used to measure the refractive index (n), absorption coefficient (α), and thickness of the samples. The n and α are compositional dependent and the characteristic of the samples changed with different Sn incorporation in the Ge lattice. Data analysis of the samples showed a change in these optical properties for different samples. In order to compare the changes in the optical properties of GeSn, the optical properties of a bulk Ge sample were also measured.

Figure 44a shows the measured refractive index and absorption coefficient for a $Ge_{0.98}Sn_{0.02}$ sample grown at 350 °C, $SnCl_4$ flow of 0.5 sccm, and growth pressure of 1 torr. The characterization result is compared to Ge bulk characteristic from 1000 to 2400 nm wavelength. The bandgap edge of the $Ge_{0.98}Sn_{0.02}$ sample resulted in a shift in the characteristic curve of the GeSn sample towards longer wavelength in comparison with Ge. Due to the increase in the absorption coefficient towards longer infrared wavelengths, the GeSn devices can operate at longer wavelengths.

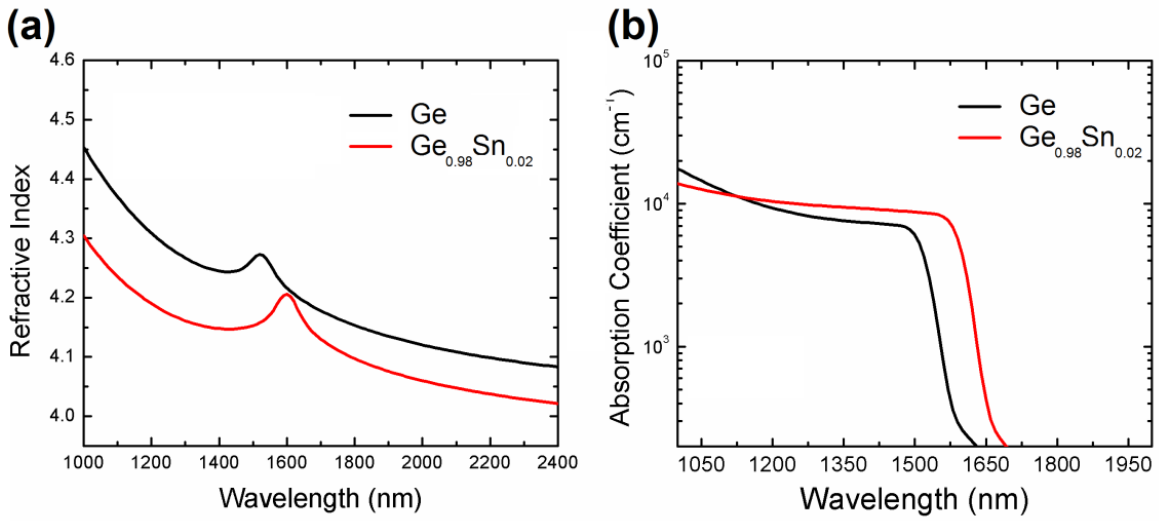

Figure 44. Optical charactrization of the $Ge_{1-x}Sn_x$ samples using spectroscopic ellipspmetry. (a) Refractive index and (b) absorption coefficient of bulk Ge and $Ge_{0.98}Sn_{0.02}$ sample grown at 350 °C temperature and 1 torr chamber.

Measurement of film thickness using spectroscopic ellipsometry technique was performed to understand the growth mechanism of the films at different conditions. Figure 45a shows the thickness measurement of the samples grown at 350 °C and 0.5 torr with flow rates of $SnCl_4$ from 0.3 to 0.5 sccm. The film thickness for all samples showed an increase from 0.1 torr to 0.5 torr but the thickness decreased above 0.5 torr. The increase in the film thickness at higher pressures was the result of higher residence times of ad-species. However, as discussed in the PL section, increased pressure resulted in a higher decomposition rate of $SnCl_4$ with respect to GeH_4 due to lower bond energy of the molecules [20]. Such higher decomposition rate resulted in higher production rate of HCl according to a previously discussed reaction (Equation 6). High pressure results in more GeH_4 etching because $SnCl_4$ decomposition produces four HCl molecules which can etch four Ge atoms from crystal sites. Dominance of etching results in lower film thickness and lower material quality which results in lower PL intensity as can be seen in Figure 45b. A similar phenomenon in decreasing the film thickness as a result of increase in the pressure was observed for higher growth pressure of GeSn films without carrier gas as discussed in Section 4.1.

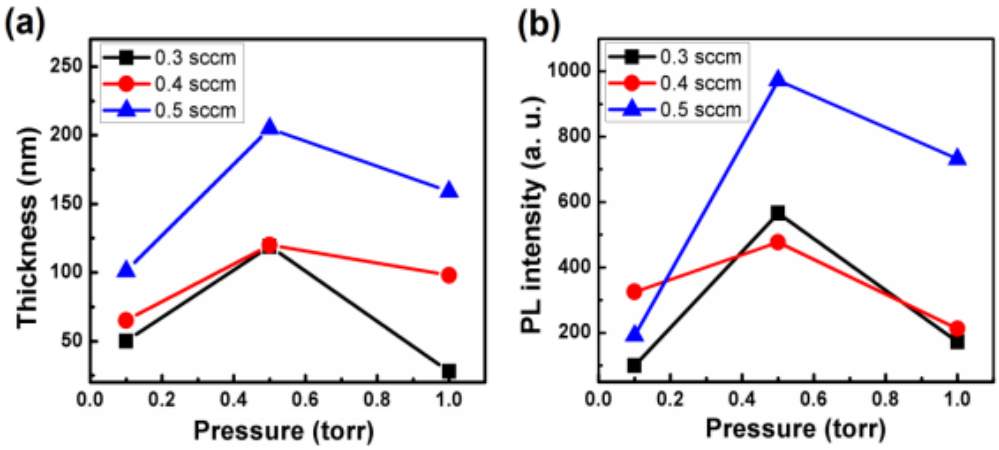

Figure 45. Film thickness and PL intensity of GeSn films as a result of deposition pressure change. (a) Change in the thickness and (b) PL intensity of the GeSn samples grown for different flow rates of $SnCl_4$ at growth pressures of 0.1 to 1 torr at 350 °C growth temperature.

4.3. SiGeSn growth using $SnCl_4$

Development of ternary alloy of SiGeSn is very important due to the ability of engineering the bandgap and lattice constant separately. A wider bandgap SiGeSn layer could be grown lattice-matched to a GeSn to serve as a barrier layer for confinement of electrons and holes simultaneously. Such GeSn/SiGeSn quantum well structures have been used to design semiconductor lasers [18]. However, growth of SiGeSn film is more challenging than GeSn due to lower decompostition rates of Si at the required growth temperature of the alloys. Since Bauer *et al.* reported the first SiGeSn growth on a GeSn buffer layer using $SiGeH_6$ and SnD_4 [39], only a few groups have successfully demonstated the SiGeSn growth [38, 43]. In all the growth methods, higher order silanes and germanes or silogermanes have been used for the growth. In this section, the direct growth of SiGeSn films on Si substrate using a cold-wall UHV-CVD system is presented. Stannic chloride, germane and silane have been used as low cost precursors for Sn, Ge, and Si, respectively.

4.3.1. Growth method

The growth of SiGeSn films was carried out on p-type 4" Si (100) substrates having a resistivity of 10-20 Ω-cm. Deposition pressure was varied from 0.1 to 1.5 torr at a substrate temperature of 300 °C. The flow rate of gas precursors was controlled from 1 to 10 sccm. The study of growth mechanism was performed in terms of the gas flow rate and pressure, as listed in Table V.

Table V. Mechanism study of SiGeSn growth.

Parameters	SiH_4 (sccm)	GeH_4 (sccm)	$SnCl_4$ (sccm)	Pressure (torr)	Temperature (°C)
Flow rate	From 1 to 10	10	From 1 to 2	0.1	300
Pressure	2	10	1	From 0.1 to 1.5	300

4.3.2. Material characterization

Rutherford backscattering (RBS)

The as-grown SiGeSn samples were characterized using RBS to determine the amount of Sn and Si incorporation in the Ge lattice. Figure 46 shows the random and [001] aligned RBS data from a SiGeSn film with 3.1% Si and 1.9% Sn incorporation. The thickness of the sample was measured to be 8 nm. Comparison of the random and aligned spectra of this sample shows Si and Sn were substitutionally incorporated in the Ge lattice, however, in some samples the incorporation of Sn was shown to be not substitutional and the films were grown mostly amorphous. Further investigation on the crystal quality of the films was done using XRD and TEM characterization.

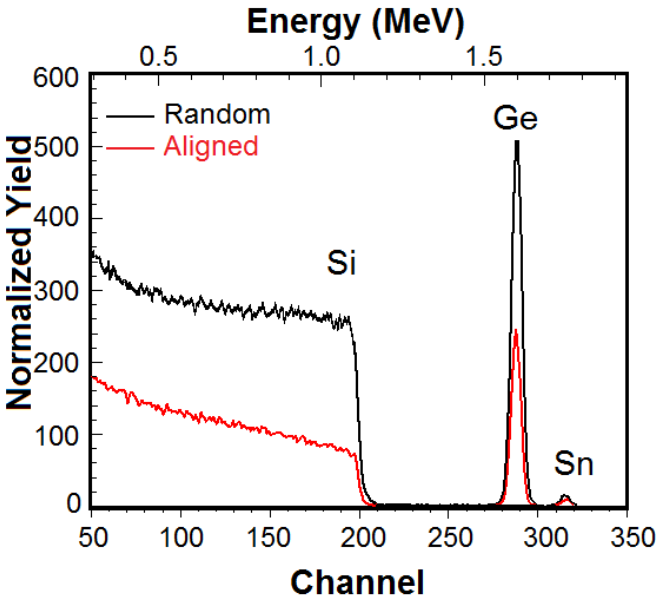

Figure 46. Random and aligned RBS spectra for a 8 nm $Si_{0.03}Ge_{0.95}Sn_{0.02}$/Si film.

X-ray diffraction

The symmetric (004) 2Theta-Omega XRD scans of SiGeSn films with 4% Si and 3% Sn are shown in Figure 47a. The SiGe and GeSn alloys are also shown as benchmark samples for

comparison. The higher-angle peak of the Si substrate was recorded at ~69° while the peak at lower angles of 64-65° shows the SiGe, SiGeSn, and GeSn films. Due to the smaller lattice constant of Si (a^{Si} = 5.431 Å) and the larger lattice constant of α-Sn (a^{Sn} = 6.491 Å) compared to Ge (a^{Ge} = 5.658 Å), the peaks for SiGe are shifted towards higher angles and the peak for GeSn is at lower angles with respect to the Ge (004) peak. Depending on the incorporation percentage of Si and Sn, the peak of SiGeSn film is located between these two peaks when the films have equal strain.

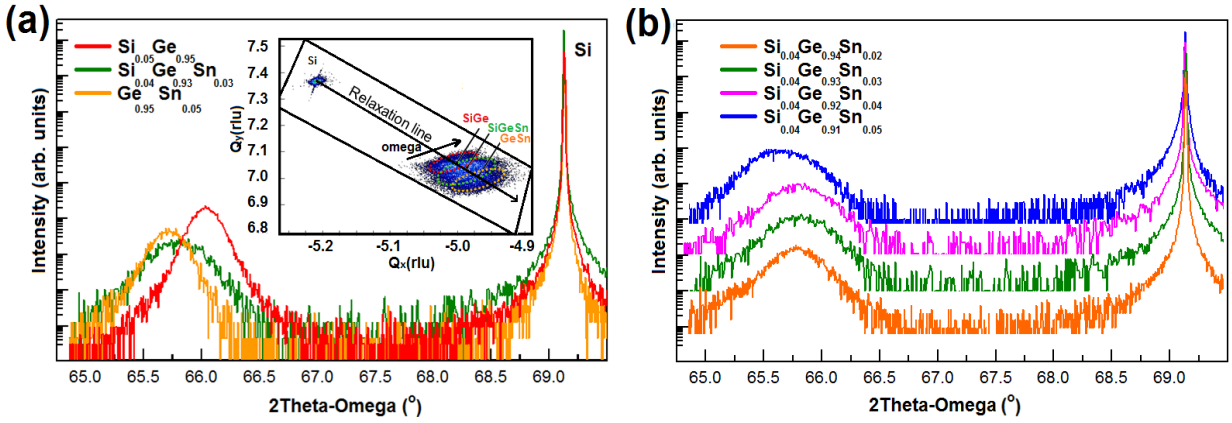

Figure 47. The XRD characterization of SiGe, GeSn, and SiGeSn films. (a) The XRD pattern of SiGe, SiGeSn, and GeSn films from (004) planse and the superposition of the RSMs grown on Si substrate from (-2 -2 4) plane. (b) The XRD pattern of different composition SiGeSn films.

In order to calculate the lattice constant of the films, an RSM from an asymmetric plane was measured to extract in-plane ($a_{\parallel}$) and out-of-plane ($a_{\perp}$) lattice constants. The superposition of RSM of the SiGe, GeSn, and SiGeSn samples from the (-2 -2 4) plane is shown in the inset of Figure 47(a). The x- and y-axis (Qy) shows the in-plane and out-of-plane lattice constants in the reciprocal lattice unit (rlu), respectively. The spread of the RSM in the omega direction shows the presence of threading dislocations as the film was relaxed due to large lattice mismatch between Si and the SiGeSn films. The RSM scans did not show compositional

gradient in the samples. Calculation of the strain in the films showed that the samples were fully strain relaxed. The out-of-plane lattice constant, measured from 2Theta-Omega scans, was used to calculate the total lattice constant based on Vegard's law explained in Chapter 2 (Equation 2). The 2Theta-Omega XRD scans of the samples with Sn composition ranging from 2% to 5% are given in Figure 47b. With the same Si incorporation, the peak shifted towards lower angles as the Sn incorporation increased. The lattice constant of the samples are summarized in Table VI.

Table VI. Composition, lattice constant and thickness of the SiGeSn samples.

Sample #	Si%	Ge%	Sn%	*a* (nm)	Thickness(nm)
1	3.1	95.0	1.9	5.665	8
2	3.9	93.8	2.3	5.666	16
3	3.9	93.3	2.8	5.671	16
4	4.8	92.3	2.9	5.669	29
5	3.9	92.0	4.1	5.681	61
6	4.1	91.0	4.9	5.687	88

Scanning electron microscopy

Surface morphology investigated through SEM/EDX showed uniform composition across the 4% Si, 3% Sn sample (Figure 48). The SEM micrographs in Figure 48a show continuous film growth without any crystalline patches or grains, indicating uniform material growth. Figure 48b, c, and d show the Si, Ge, and Sn EDX maps of the $Si_{0.04}Ge_{0.93}Sn_{0.03}$ sample, respectively. Composition uniformity was observed for all grown samples.

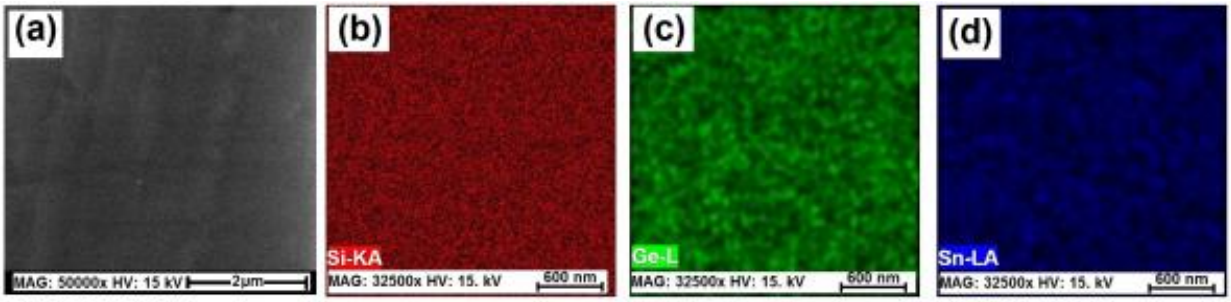

Figure 48. The SEM micrograph and EDX maps of the $Si_{0.04}Ge_{0.93}Sn_{0.03}$ sample. (a) SEM micrograph, (b) Si EDX map, (c), Ge EDX map, and (d) Sn EDX map.

Transmission electron microscopy

The SiGeSn film thicknesses were investigated using high-resolution TEM. Figure 49(a) shows the cross-sectional view of a $Si_{0.04}Ge_{0.91}Sn_{0.05}$ layer on a Si substrate. Formation of misfit dislocations at the SiGeSn/Si interface relaxed the epitaxial layer and no pseudomorphic growth was observed in any part of the sample. The Fourier reciprocal lattice of the image using a fast Fourier transform (FFT) image processing technique was used to inspect the quality of the films. Circular filtering masks were applied to different diffraction point pairs of (-200, 200), (-3-1-1, 311) and (0-2-2, 022) to maximize image intensity and remove the background signals. Selecting different diffraction point pairs enabled study of growth quality in different planes and defect formation at the interface. The applied filtering mask to the (200, -200) diffraction point pairs is shown in Figure 49b. The direct image of the diffraction plane was reconstructed by inverting the FFT. The main reason to choose a filter for the (200, -200) pair plane was to see the reconstructed image in the growth direction of the film.

Figure 49c is the inverse FFT of SiGeSn layer on top of Si substrate. The top part of the image shows SiGeSn layer and the bottom part of the image shows the Si substrate. The arrow shows formation of a misfit dislocation at the SiGeSn/Si interface leading to a slight tilt in the

SiGeSn layer. Inverse FFT of (-3-1-1, 311) and (0-2-2, 022) diffraction point pairs also revealed formation of misfit dislocations at the interface as well as high growth quality.

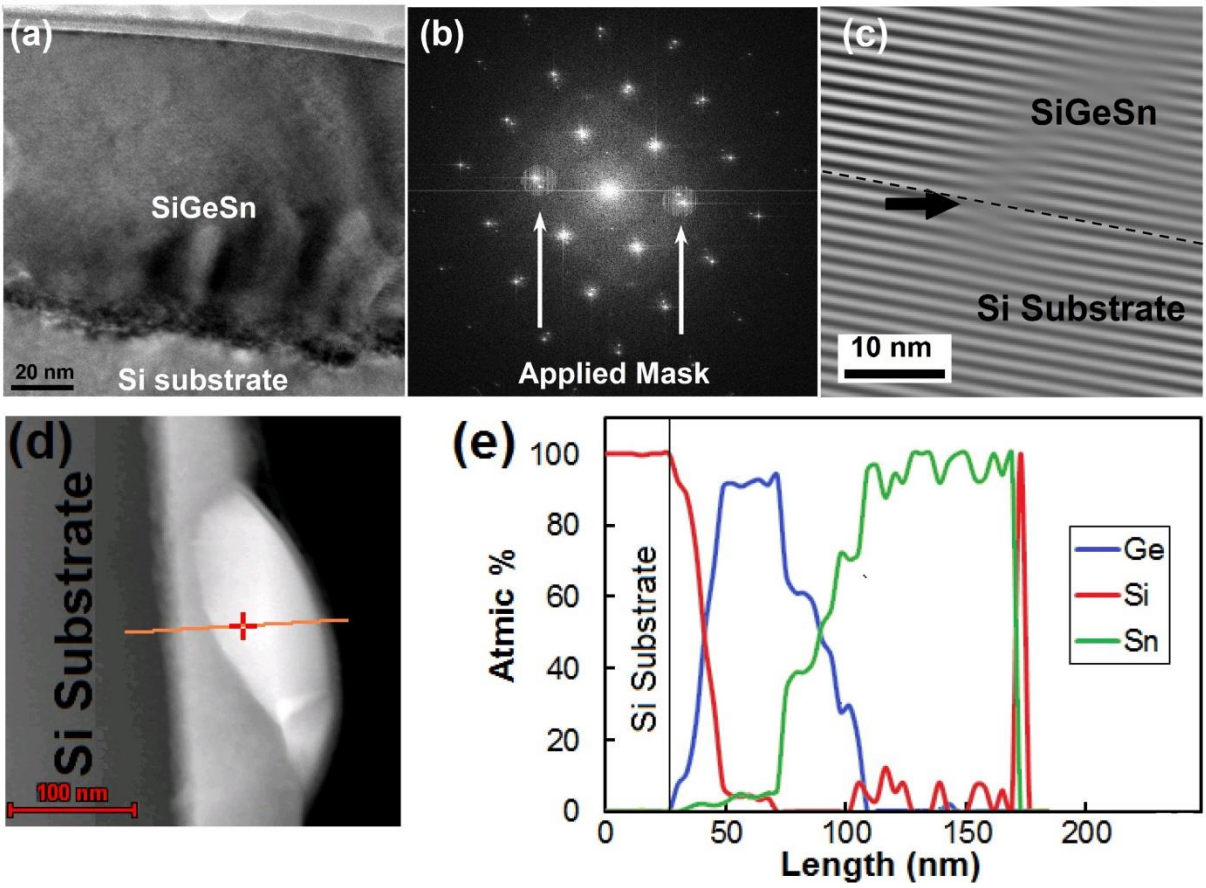

Figure 49. TEM characterization of $Si_{0.05}Ge_{0.90}Sn_{0.05}$ sample. (a) The cross-sectional TEM images of $Si_{0.05}Ge_{0.90}Sn_{0.05}$ samples. (b) FFT image processing by applying a circular mask at the (200, -200) diffraction point pairs. (c) Reconstructed image of the sample achieved by inverse FFT of (b). (d) Scanning TEM micrograph of $Si_{0.04}Ge_{0.91}Sn_{0.05}$. (e) The EDX line scan showing the atomic percentage of Si, Ge and Sn along the scanned area in (d).

Analysis of the film composition by cross-sectional SEM/EDX was done on different parts of the TEM sample and showed uniform Si and Sn incorporation. Tin precipitation from the SiGeSn lattice was observed at some points as seen in the cross-sectional SEM micrograph (Figure 49d). A line EDX scan of the segregated area showed the material composition of the film and the droplet. Figure 49e shows that the composition of the film was $Si_{0.04}Ge_{0.91}Sn_{0.05}$

while the droplet was $Si_{0.05}Sn_{0.95}$. Due to the low solubility of Si in Sn, some of the Si had precipitated on the $Si_{0.05}Sn_{0.95}$ droplet.

4.3.3. Growth mechanism

Different flow rates of the precursors at various chamber pressures were studied to understand the growth mechanism of SiGeSn films, as was shown in Table V. The etching mechanism was studied by changing the $SnCl_4$ flow rate at fixed SiH_4/GeH_4 flow ratios. The results showed that films were etched off when the $SnCl_4$ flow rate was above 1 sccm. No film growth was achieved at any SiH_4/GeH_4 flow ratio when the $SnCl_4$ flow rate was more than 1 sccm, which was attributed to the increase in HCl byproduct as a result of increase in the $SnCl_4$ flow rate. In deposition of a Si or Ge atom, 2 molecules of H_2 are released. The available H_2 could produce HCl (Equation 6) which is an etchant of Si and Ge.

$$2H_2 + SnCl_4 \rightarrow Sn + 4HCl \qquad \text{(Equation 6)}$$

The epitaxial growth of SiGeSn films was investigated by varying the SiH_4/GeH_4 flow ratio. The $SnCl_4$ flow rate and the chamber pressure were fixed at 1 sccm and 0.1 torr, respectively. Figure 50a shows the Si and Sn incorporations and film thickness as a function of the SiH_4/GeH_4 flow ratio. It is clear that as the SiH_4/GeH_4 flow ratio increased, the incorporation of Si and Sn increased until the ratio reached 0.4, after which the SiGeSn film became amorphous. This can be explained as the increase in Si ad-atoms, associated with high SiH_4 flow rates, reduced the surface mobility of the ad-atoms, resulting in a crystalline-amorphous transition. On the other hand, increasing SiH_4/GeH_4 flow ratio increased Sn incorporation. This is in agreement with the notion that higher incorporation of smaller size Si

atoms would facilitate higher incorporation of the larger atomic size Sn into Ge without causing undue strain. Furthermore, thicker films were achieved as the partial pressure of SiH_4 was increased, as shown in Figure 50a.

The effect of deposition pressure on the Si and Sn incorporation was also studied. Precursor flow ratios were fixed at 1:2:10 for $SnCl_4$:SiH_4:GeH_4. Figure 50b shows the Si and Sn incorporation as a function of chamber pressure. As the pressure was increased, the Sn incorporation increased from 2.8% to 4.9%, while the Si incorporation slightly changed from 3.9% to 4.1%. A similar trend on the increase in Sn incorporation was observed in the GeSn growth presented in Section 4.1.3.

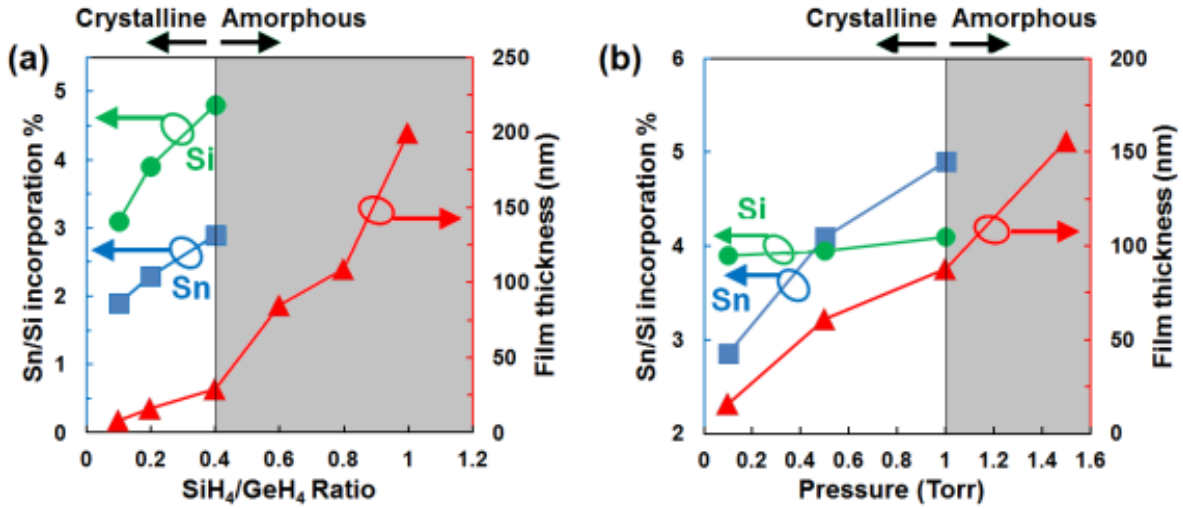

Figure 50. Growth mechanism of SiGeSn films on Si at different precursor flow rates and depostion pressures. (a) Increase in the Si (solid green circles) and Sn (solid blue squares) incorporation and increase in the film thickness (solid red triangles) as a result of SiH_4/GeH_4 flow ratios. (b) Similar trend was observed by increasing the deposition pressure.

This was attributed to the residence time of the precursors which increased from 1.9 s at 0.1 torr to 19 s at 1 torr deposition pressure. Increased collision frequency of the atoms at higher pressure gave rise to the possibility of inelastic collision which caused the breakdown of the molecular bonds. However, more Sn was incorporated as the bond energy of $SnCl_4$ was

lower than SiH_4 [20]. The film thickness kept increasing as the pressure rose but amorphous growth of SiGeSn film was observed at pressures greater than 1 torr. This was due to further reduction of Si ad-atom surface mobility that also resulted in a concomitant sharp increase in deposition rate.

4.3.4. Optical characterization

Photoluminescence

Figure 51a shows room temperature PL spectra for SiGeSn films with 3, 4, and 5% Sn and 4% Si mole fractions. A shorter wavelength main peak and a longer wavelength shoulder were observed for each sample, corresponding to direct and indirect bandgap transitions, respectively. As Sn composition increased, both direct and indirect peaks shifted towards longer wavelength, which agrees with theoretical study. The direct and indirect bandgap energies were extracted by fitting the PL spectra with Gaussian curves [14] as illustrated in Figure 51a. Figure 51b shows the bandgap energies as a function of Sn compositions. The data were obtained from Figure 51a and the lines were calculated from Equation 1 in Section 1.2.1. (The bandgap of GeSn is also shown for comparison.)

Since incorporation of Sn shifts the PL peak towards longer wavelength while the incorporation of Si shifts the PL towards shorter wavelength, the PL peak position of SiGeSn was determined by both Si and Sn compositions. The experimental data were in agreement with theoretical calculations. Compared with GeSn material, the bandgap of SiGeSn was always wider with the same Sn composition, revealing that the SiGeSn film could be a good candidate for a barrier layer in SiGeSn/GeSn/SiGeSn double heterostructure or quantum well structures.

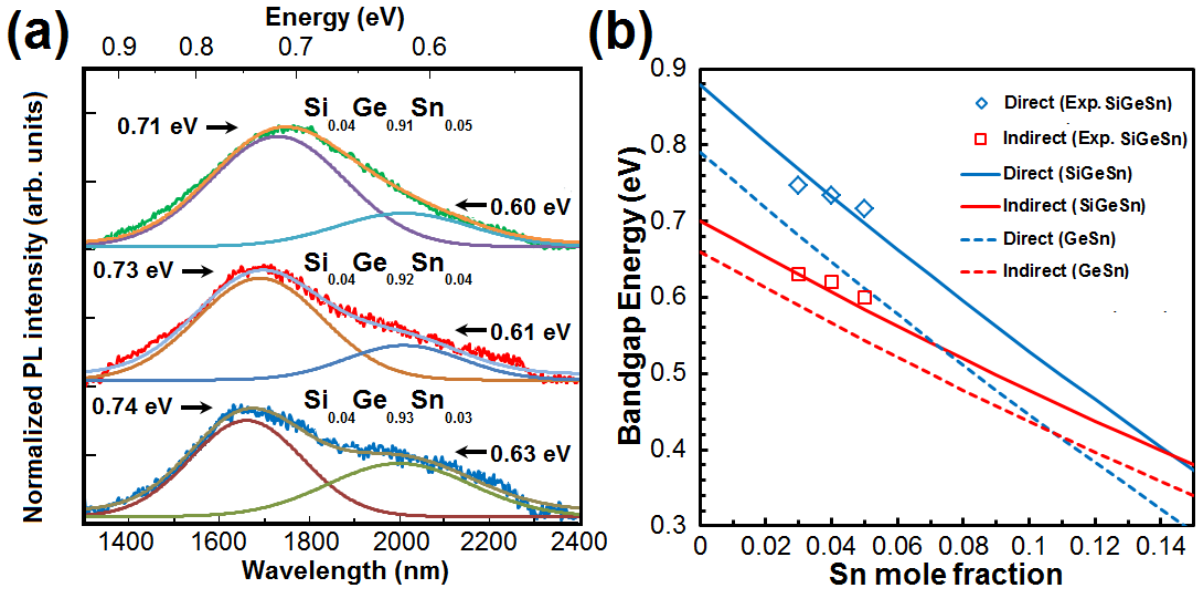

Figure 51. Optical characterization of the SiGeSn samples using PL spectroscopy. (a) PL spectra of the SiGeSn films with 3, 4, and 5% Sn and 4% Si mole fractions. (b) Theoretical calculation of change in the direct (blue) and indirect (red) bandgap edges for $Ge_{1-x}Sn_x$ (dashed line) and $Si_{0.04}Ge_{0.96-x}Sn_x$ (solid line) as a function of Sn incorporation (x).

Chapter 5. GeSn and SiGeSn growth using SnD_4 precursor

Growth of GeSn and SiGeSn alloys using SnD_4 precursor in CVD systems have shown a robust growth method and high material quality [26]. However, usage of compound chemistries of higher order silanes and germanes or even more compound hetero-nuclear Si-Ge molecules has kept the growth from being commercially applicable. [25]. Additionally, handling and delivery of SnD_4 requires design of new systems. Extended storage time of this gas is only successful at liquid nitrogen temperature (~ -200 °C) and the gas needs to be used after warming up the bottle to dry ice temperature (-80 °C).

Moreover, due to rapid decomposition and deposition of Sn in the delivery line, highly diluted SnD_4 gas (1% in H_2) has been inevitable for more accurate readings of mass flow controllers as described in 1.2.2. Therefore, SnD_4 either has to be diluted before delivery, which requires a complicated delivery system, or the bottles must be purchased with diluted gas which limits the amount of gas available for deposition. The other solution for deposition of the material is preparing the desired mixture in small bottles (~3 liters) containing SnD_4 and higher order silanes and germanes and then using the mixture for deposition of the film [38]. The gases in those mixtures are mostly in-situ produced and mixed. Each of the above methods of SnD_4 delivery may be used for research but are not up to the industrial use standard.

In this chapter, the growth of low Sn content GeSn and SiGeSn films using in-situ gas mixing of SnD_4 and low cost Si and Ge precursors (silane and germane) via a UHV-CVD system is presented.

5.1. Growth method

Silane, germane, and deuterated stannane were used as the precursors for (Si)GeSn deposition and argon was used as the carrier gas. The deposition pressure was in the range of

0.1 to 1 torr. The films were grown at the temperature range of 300 to 450 °C. The deposition time for the samples was 15 minutes. The typical SnD_4 pressure percentage in the chamber was 4% and GeH_4 was 96%. The study of the growth mechanism was performed in terms of the gas flow rate and pressure, as listed in Table VII.

Table VII. Mechanism study of GeSn, SiGeSn growth.

Alloy	SiH_4 (mtorr)	GeH_4 (mtorr)	SnD_4 (mtorr)	Deposition Pressure (torr)	Temperature (°C)
GeSn	---	10	0.5 - 1	0.1 - 1	300 - 450
SiGeSn	1 - 2	10	0.5 - 1	0.1 - 1	300 - 450

5.2. Material characterization

5.2.1. X-ray diffraction

The 2Theta-Omega XRD scan of the GeSn samples from (004) plane is shown in Figure 52a. The Si (001) substrate peak was observed at 69° and the GeSn layers were at different angles from 65 to 66°. The out-of-plane lattice constants of the layers were directly calculated from the peaks observed in Figure 52a. The total lattice constants of the films were calculated from the RSM as observed in the inset of Figure 52a. Additionally, the RSMs show that the films were relaxed with a spread in the omega direction that showed mosaicity of the films. This is because of the high density of defects in the film due to large lattice mismatch between GeSn and Si (more than 4.2%).

The Sn composition of the GeSn samples were calculated using Vegard's law as explained in Section 1.2.1. The XRD peaks showed that the films grown at higher temperatures incorporated less Sn in the Ge lattice. The sample grown at 300 °C had 2% Sn incorporation while the one grown at 450 °C had only 0.5% Sn incorporation. On the contrary, higher growth

temperatures resulted in higher material quality. This could be seen by comparing the GeSn peak intensities. The growth at 300 °C had one order of magnitude lower peak counts compared with the one grown at 450 °C. The XRD patterns shown in Figure 52 are for the samples that were grown at a constant growth pressure of 1 torr with a fixed SnD_4 partial pressure of 0.5 mtorr. Reduction of the growth pressure from 1 torr to 0.1 torr gave similar XRD patterns. Increasing the partial pressure of SnD_4 from 0.5 mtorr to 1 mtorr resulted in poor quality films.

Introduction of SiH_4 in the chamber resulted in the incorporation of Si in the GeSn lattice. Figure 52b shows the 2Theta-Omega scan of the SiGeSn films grown at 0.5 torr deposition pressure. The peak at higher diffracted angle shows the growth at 450 °C with 2 mtorr partial pressure of SnD_4 and the lower count peak shows the sample grown at 400 °C with 1 mtorr partial pressure of SiD_4. The RSM scan of the samples show that the films were strain relaxed; however, a larger spread was observed along the omega direction compared with the GeSn films. The inset of Figure 52b shows the RSM for the $Si_{0.17}Ge_{0.91}Sn_{0.02}$ film which was grown at 450 °C with 2 mTorr SiH_4 partial pressure. The spread in the SiGeSn films could be attributed to the incorporation of Si which has lower surface mobility in comparison with Ge. This resulted in a higher density of threading dislocations in the SiGeSn films and a larger spread in the RSM. The Si and Sn incorporation in the SiGeSn samples were measured using EDX as they could not be directly measured through XRD.

5.2.2. Energy-dispersive X-ray spectroscopy

In order to study the uniformity of incorporation of the elements in the film, the samples were examined using a scanning electron microscope equipped with EDX. The EDX maps showed that as the growth temperature exceeded 400 °C, the Sn started to precipitate to the surface.

Growth at these temperatures was away from non-equilibrium conditions. This characteristic of Sn was the main reason for low incorporation at high temperatures; therefore, low temperature growth was preferred for more Sn incorporation.

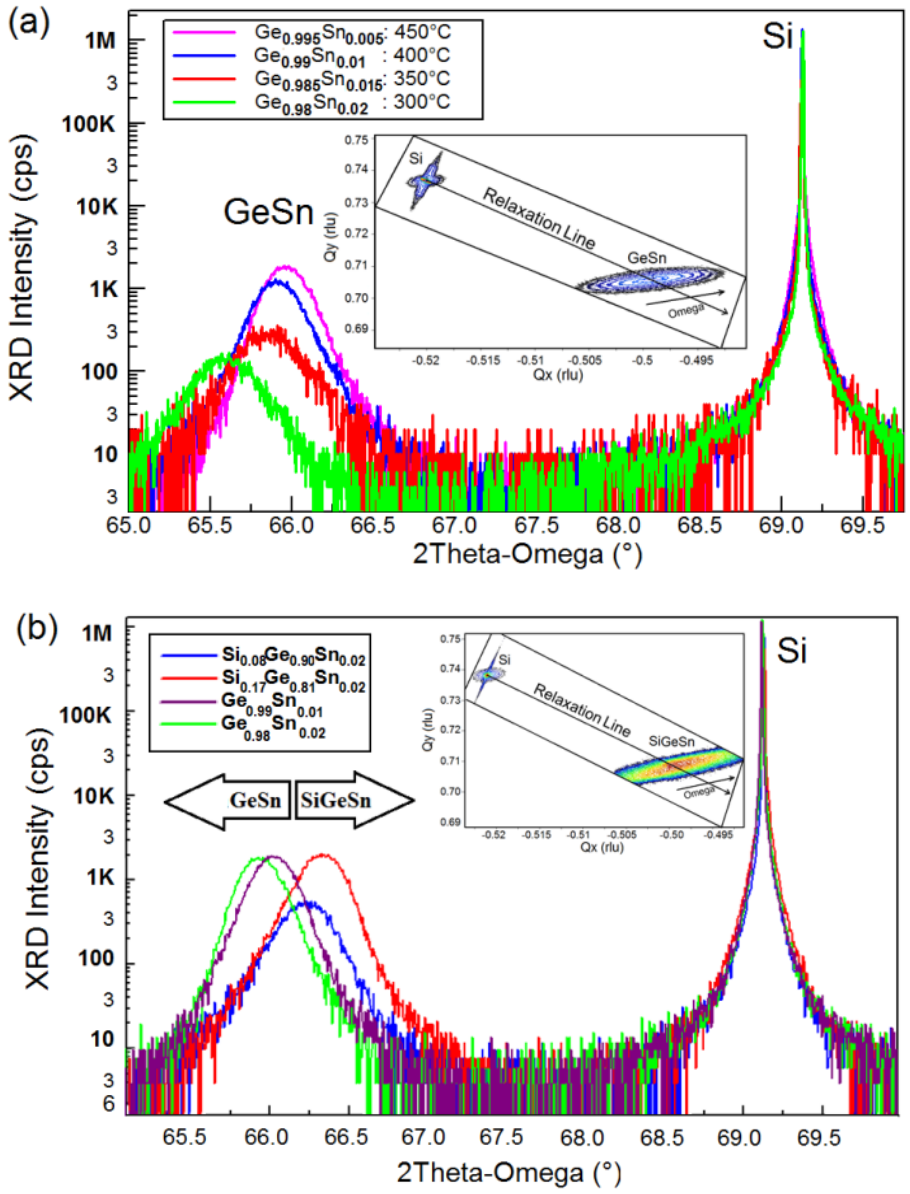

Figure 52. XRD characterization of GeSn and SiGeSn films grown on Si substrate. (a)The XRD pattern the GeSn peaks grown at different temperatures. Inset shows the RSM of the $Ge_{0.98}Sn_{0.02}$ sample grown at 450 °C. (b) The SiGeSn peaks are between 65-67º due to Si incorporation while the GeSn peaks are between 66-65º. The inset shows the RSM of $Si_{0.17}Ge_{0.81}Sn_{0.02}$.

Figure 53a, b, and c show the Si, Ge, and Sn EDX maps of the GeSn film grown at 450 °C, respectively. There was no Si incorporated in the sample but the Si substrate map was observed due to low film thickness. The Sn map showed that Sn precipitation occurred at some points. Figure 53d, e, and f show the Si, Ge and Sn EDX maps of the SiGeSn film grown at 400 °C, respectively. No Sn precipitation was observed for the samples grown below 400 °C. The Si map could be attributed to both the Si substrate and Si in the film. In order to confirm the Si incorporation in the film, a cross sectional EDX scan of the sample was performed using the TEM system.

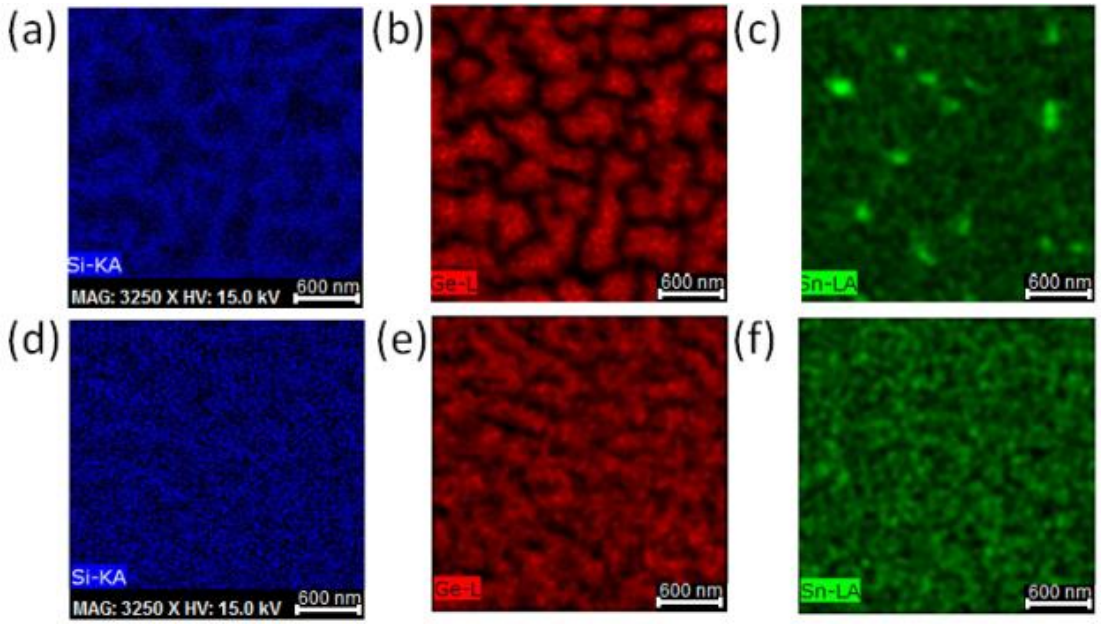

Figure 53. Energy dispersive X-ray (EDX) spectroscopy of the samples obtained from scanning electron microscope. GeSn: (a) Si EDX map, (b) Ge EDX map, and (c) Sn EDX map. SiGeSn: (d) Si EDX map, (e) Ge EDX map, and (f) Sn EDX map.

5.2.3. Transmission electron microscopy

The crystal quality and the thickness of the samples were characterized using TEM. The TEM images show that the films were grown epitaxially on Si substrate and were relaxed

through an array of misfit dislocations. Figure 54 is the TEM image of the $Ge_{0.99}Sn_{0.01}$. The film was relaxed by formation of two types of dislocations: threading dislocations and Lomer dislocations.

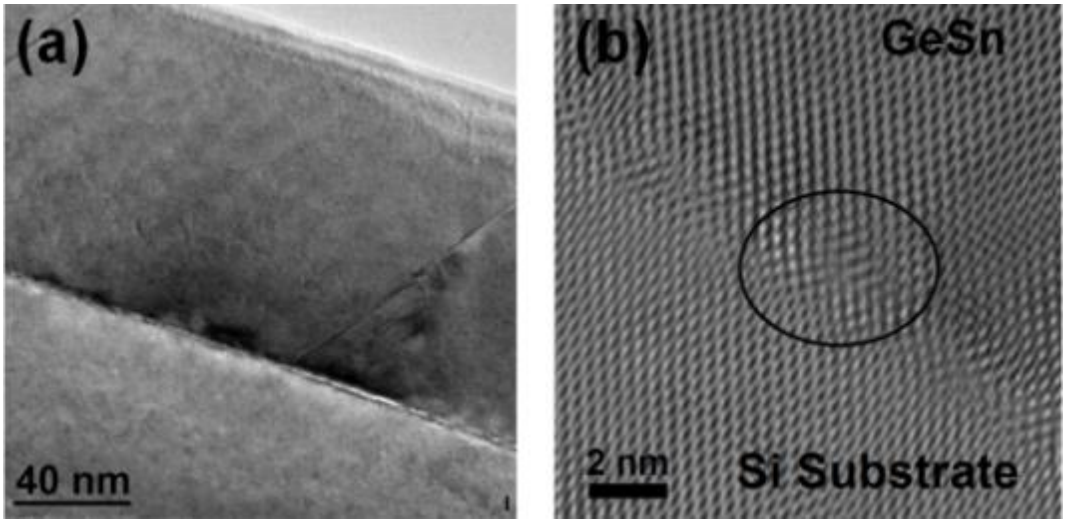

Figure 54. Transmission electron microscopy (TEM) image of the $Ge_{0.99}Sn_{0.01}$ film. (a) Low resolution TEM image. (b) Lomer misfit dislocation formed at the interface of GeSn/Si. The image was reconstructed from inverse FFT after applying a periodic mask to increase the contrast.

Figure 54a shows that misfit dislocation could screw through the film and form a threading dislocation. Such dislocations lower the film quality by formation of non-radiative recombinations centers across the film. Formation of Lomer misfit dislocations were also observed (Figure 54b). Figure 54b was generated by taking the fast Fourier transform (FFT) from the TEM image and applying a periodic circular mask. The reconstructed figure, by taking the inverse FFT, increased the contrast and showed the atoms more clearly. In Figure 54b it can be seen that a Lomer misfit dislocation was formed without a threading component that screws through the film. Formation of such dislocations at GeSn interfaces has been shown to have different 7-atom and 11-atom rings (will be further discussed in Section 6.2).

Figure 55a and b show the low resolution and high resolution TEM images of the SiGeSn film, respectively. A higher density of threading dislocations and stacking faults were observed due to the incorporation of Si in the GeSn lattice. This could be attributed to the low surface mobility of Si atoms on the surface at the low temperature of 400 °C.

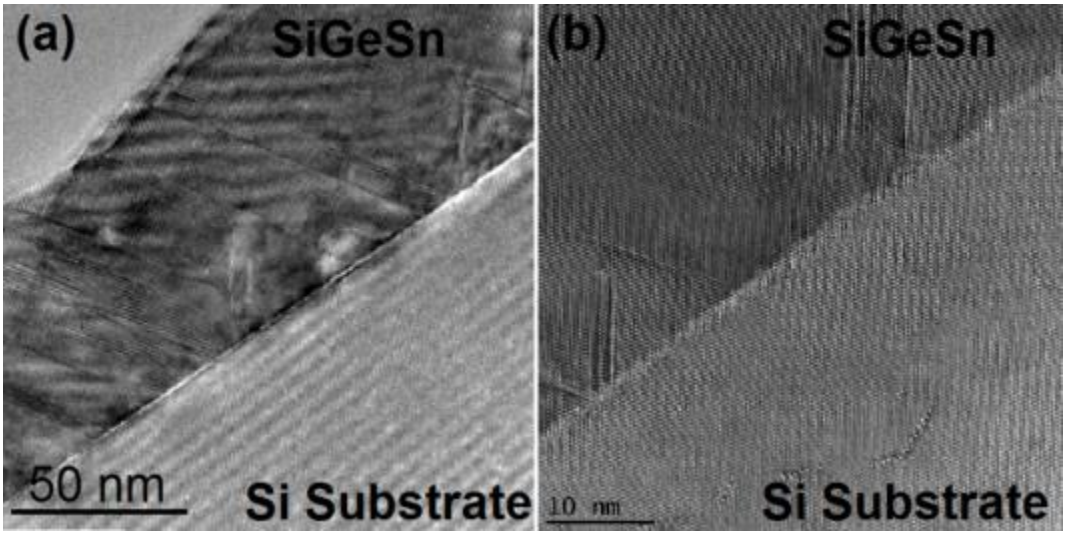

Figure 55. Transmission electron microscopy (TEM) image of the SiGeSn film. (a) Low resolution TEM image. (b) High magnification TEM image showing high density of threading dislocations at the interface of SiGeSn/Si.

High angle annular dark field (HAADF) scanning transmission electron microscopy (STEM) of the samples was performed to confirm Si incorporation in the SiGeSn films and measure the amount of Si and Sn. Figure 56a shows the HAADF image with the cross sectional Z-contrast map of the $Si_{0.08}Ge_{0.90}Sn_{0.02}$ film. The maps show uniform Si, Ge and Sn incorporation along the growth. An EDX line scan of the sample is shown in Figure 56b which shows the film was grown uniformly. Similar scans were done on other SiGeSn samples to confirm the composition. The results were in agreement with the lattice constant calculations using the Vegard's law and XRD data (Section 5.2.1) for SiGeSn films.

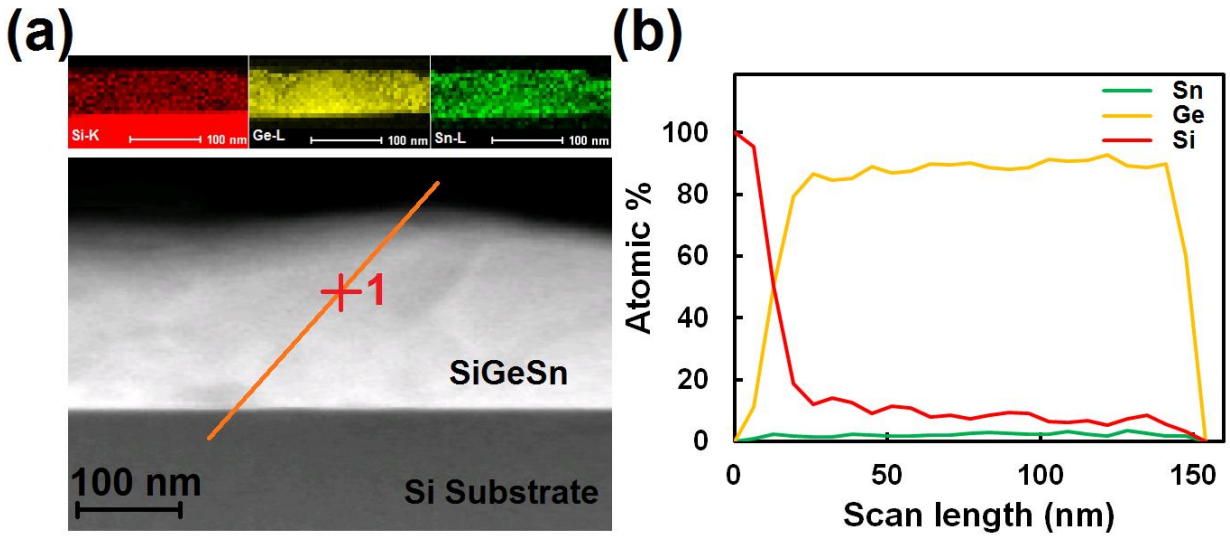

Figure 56. High angle annular dark field (HAADF) scanning TEM of the $Si_{0.08}Ge_{0.90}Sn_{0.02}$ film. (a) Scanning TEM along with EDX maps of Si, Ge and GeSn. (b) The EDX line scan of the $Si_{0.08}Ge_{0.90}Sn_{0.02}$ sample.

5.3. Optical characterization

5.3.1. Raman spectroscopy

The GeSn and SiGeSn films were characterized using Raman spectroscopy. Figure 57a shows the normalized Raman spectroscopy of GeSn samples with different Sn compositions. A shift was observed in the Raman peak for the Ge-Ge bond towards lower wavenumbers. This is due to incorporation of Sn in the Ge lattice which changes the bond energy of the Ge atoms in the lattice. The change in the Ge-Ge bond from 300.00 cm^{-1} for bulk Ge to ω=297.4 cm^{-1} for $Ge_{0.98}Sn_{0.02}$ showed that the films were strain relaxed [76]. The Ge-Sn peak at 259.8 cm^{-1} indicated incorporation of Sn in the $Ge_{0.98}Sn_{0.02}$ sample.

The results are in agreement with the theoretical calculations presented in Section 1.2.1. The Raman shift of the SiGeSn films showed the presence of Ge-Sn, Ge-Ge, Si-Ge, and Si-Si peaks (Figure 57b). The Ge-Ge peaks were shifted to lower wavenumber due to Si and Sn incorporation. The shift was measured to be 296.5 cm^{-1} for $Si_{0.17}Ge_{0.81}Sn_{0.02}$ and 294.3 cm^{-1} for

the $Si_{0.08}Ge_{0.9}Sn_{0.02}$. The Si-Ge peak was located at ~385 cm^{-1} and the Si-Si was at ~520 cm^{-1}. The shift in the Si-Si peak of the $Si_{0.17}Ge_{0.81}Sn_{0.02}$ from 520 cm^{-1} for bulk Si to 516 cm^{-1} showed that the peak was not from the Si substrate but from the incorporated Si in the film.

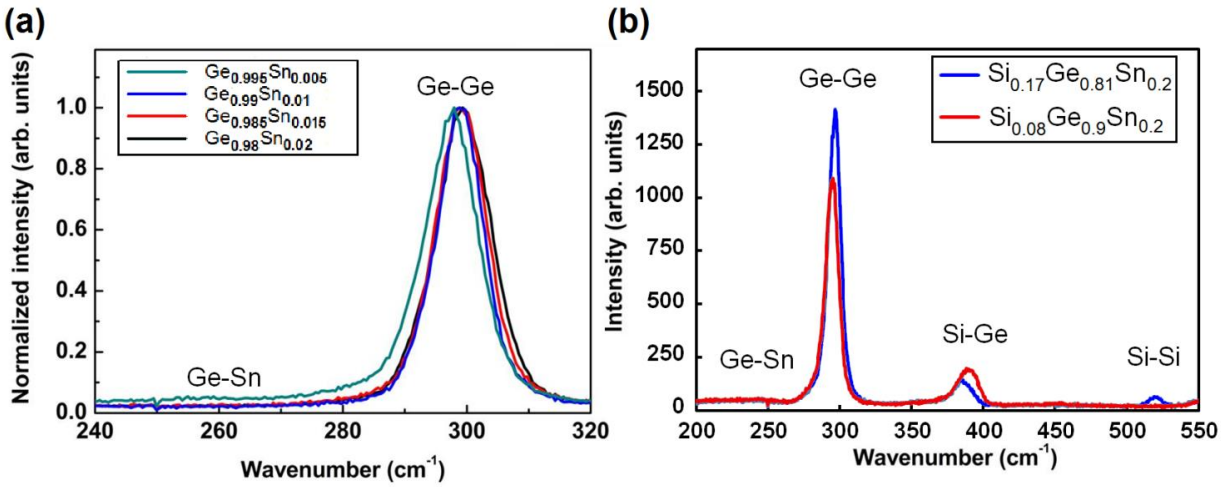

Figure 57. The Raman spectra of the (a) GeSn and (b) SiGeSn samples.

5.3.2. Photoluminescence

The PL characterization of the GeSn samples showed that incorporation of Sn in the Ge lattice resulted in an increase in the wavelength of emission spectra. Figure 58 shows the normalized PL intensity of the GeSn samples with 0.5 to 2% Sn incorporation measured at room temperature. The observed peak was attributed to the indirect bandgap (at L valley) of the samples that shifted from 1550 for pure Ge toward longer wavelength of 1650 for 2% Sn incorporation. The asymmetric shape of the peak was due to the presence of the direct emission of the films from the Γ-valley. The direct emission of pure Ge is at 1870 nm at room temperature. The PL emission of the samples could change due to strain or Sn incorporation; however, as the samples were shown to be relaxed by RSM measurements, the observed changes were attributed to the Sn incorporation in the films.

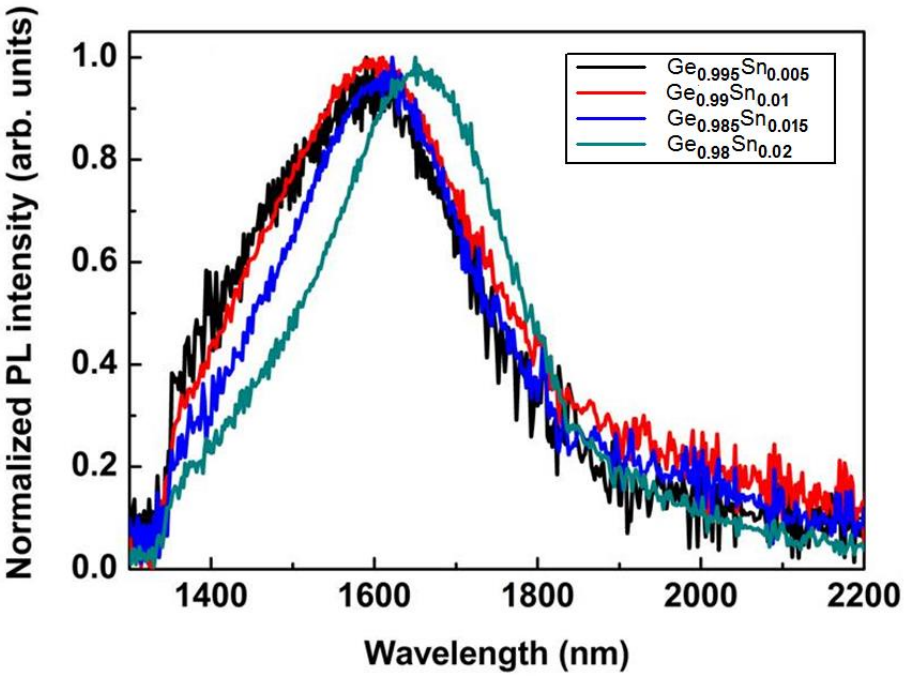

Figure 58. Photoluminescence spectra of the $Ge_{1-x}Sn_x$ films with 0.5 to 2% Sn mole fraction.

Chapter 6. Advanced GeSn material growth and characterization

Scalable and commercial growth of high quality materials requires high throughput systems such as ASM Epsilon® reduced-pressure CVD (RPCVD) reactors. In this chapter, characterization, defect formation analysis, and material quality enhancement of $Ge_{1-x}Sn_x$ alloys are discussed. The films were grown on 8" diameter Si substrates via a Ge buffer layer.

6.1. Germanium-tin growth on Ge buffer

The $Ge_{1-x}Sn_x$ alloys were grown in a single wafer RPCVD ASM Epsilon® reactor. A specialized growth approach was adopted to grow the $Ge_{1-x}Sn_x$ layers at temperatures of less than 450 °C. A relaxed buffer layer of Ge was on Si (001) as a virtual substrate prior to the growth of $Ge_{1-x}Sn_x$ alloys. Strain relaxed Ge buffer layers were grown *in situ* and require additional optimization. Table VIII shows the composition and film thickness of the grown samples. Tin concentration was measured using SIMS and randomly checked by RBS. The thickness of the samples was measured using TEM. Figure 59 shows the composition measurements of the 7.0% Sn sample which was performed by RBS and ion channeling.

Table VIII. Composition and thickness and doping of the GeSn films.

Sn% (*x*) (SIMS)	Sn% (*x*) (RBS)	Doping [B] (cm^{-3})	Thickness (nm)
0.9	-	-	327
1.4	-	3.0×10^{19}	287
2.6	3	-	257
2.7	-	5.2×10^{18}	173
3.2	3.5	-	76
3.2	-	-	134
6.0	-	-	49
7.0	7	-	240

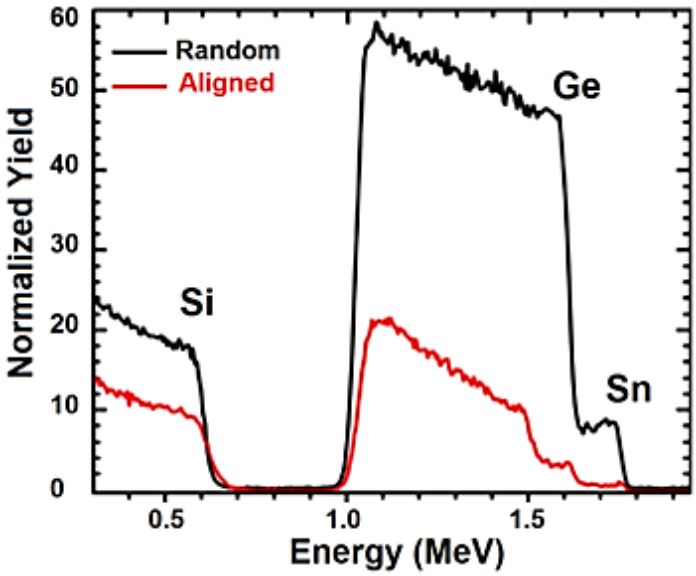

Figure 59. Random (black) and Si(001) aligned (red) RBS spectra of $Ge_{0.93}Sn_{0.07}$ with thickness of 240 nm on Ge buffer layer.

6.1.1. Material characterization

X-ray diffraction

XRD measurements were performed to investigate $Ge_{1-x}Sn_x$ lattice size and Sn composition for the samples. A symmetric 2Theta-Omega scan of the samples from (004) plane is shown in Figure 60. The Si (001) substrate peak satisfied Bragg's law at a higher angle of 69º (on the right) while peaks from Ge buffer layer and $Ge_{1-x}Sn_x$ layers were diffracted at lower angles of 66-64º due to higher lattice constant. The XRD data from (004) symmetric plane provided out-of-plane lattice constant of the layers. Therefore, an asymmetric RSM from (-2 -2 4) plane was utilized to precisely measure the in-plane and out-of-plane lattice constant of $Ge_{1-x}Sn_x$ alloys.

Figure 61 shows the (-2 -2 4) RSM sketch of the samples where perfect cubic Ge peak was set as the reference at H coordinate of -2 and L coordinate of 4, assuming in-plane strain was isotropic. The vertical line along H = -2 defines the pseudomorphic line where the $Ge_{1-x}Sn_x$

crystal was grown on top of Ge with the same in-plane lattice constant ($a_{\parallel}$). In-plane ($a_{\parallel}$) and out-of-plane ($a_{\perp}$) lattice constants of the $Ge_{1-x}Sn_x$ alloys were obtained from RSM images. Total lattice constant (a_0^{GeSn}) of $Ge_{1-x}Sn_x$ layer was calculated through

$$a_0^{GeSn} = \frac{(a_{\perp} + 2a_{\parallel}v)}{(1+2v)} \qquad \text{(Equation 10)}$$

where $a_{\perp}$, $a_{\parallel}$, and v are in-plane lattice constant, out-of-plane lattice constant, and elastic Poisson ratio of GeSn, respectively. Dependency of v to Sn composition percentage gives the corresponding value for $Ge_{1-x}Sn_x$ alloys as outlined in reference 71. The plotted Poisson line (purple) on the RSM shows how alloys with similar Sn%, but different strain, would lie on the H–L plane.

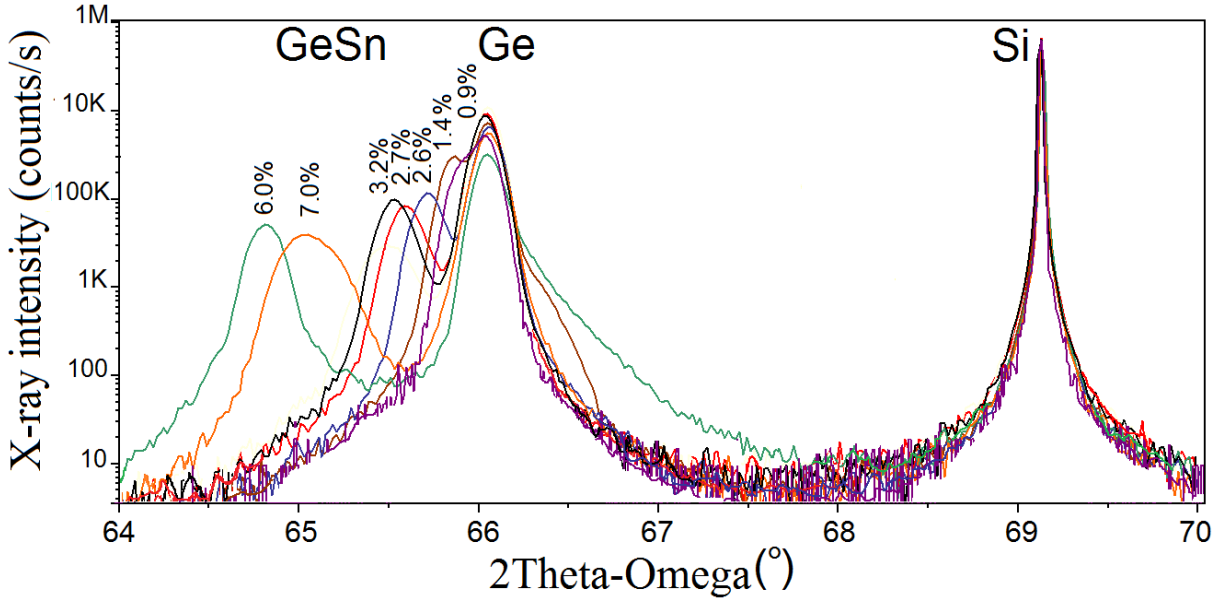

Figure 60. The XRD pattern of of $Ge_{1-x}Sn_x$/Ge films grown on Si substrate.

A 100% pseudomorphic film is achieved when the in-plane ($a_{\parallel}$) lattice constant of $Ge_{1-x}Sn_x$ equals that of relaxed Ge buffer layer. In this case, the out-of-plane ($a_{\perp}$) lattice constant is at its maximum height. In a relaxed film (where pseudomorphicity is 0%) , $a_{\parallel} = a_{\perp} = a_0^{GeSn}$.

XRD analyses in this work showed a range of 46% to 100% pseudomorphic growth for different Sn% and thicknesses.

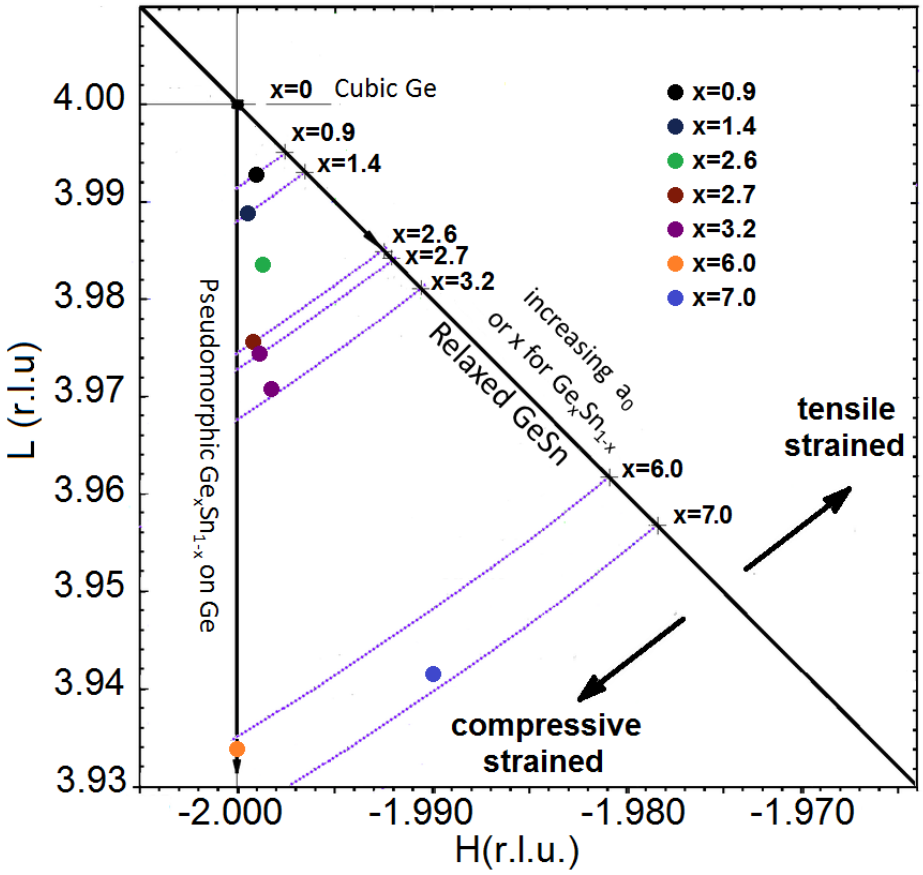

Figure 61. Sketch of RSM from assymetrical plane (-2 -2 4) for different $Ge_{1-x}Sn_x$ samples.

The RSMs revealed that $Ge_{1-x}Sn_x$ films were not relaxed; they were either fully or partially strained. Figure 62a and b compare the RSM of the alloys with 6.0% and 7.0% Sn. Increase in Sn% increased lattice mismatch which increased the compressive strain in the film. This allowed for a 6.0% Sn sample to be 100% pseudomorphic while the 7.0% Sn sample was only 49% pseudomorphic. Although higher Sn composition of the alloy pushed the structure to a more relaxed growth, it was not the only factor in pseudomorphic growth of the film. Thickness of the epi-layer can influence the strain condition of the grown film. Figure 62c and (d) compare the samples with similar Sn composition of 3.2% and different thicknesses of 76

nm and 134 nm. Pseudomorphicity of the former was measured to be 84% and the latter 72% (0.03% less in-plane strain w.r.t. 76 nm).

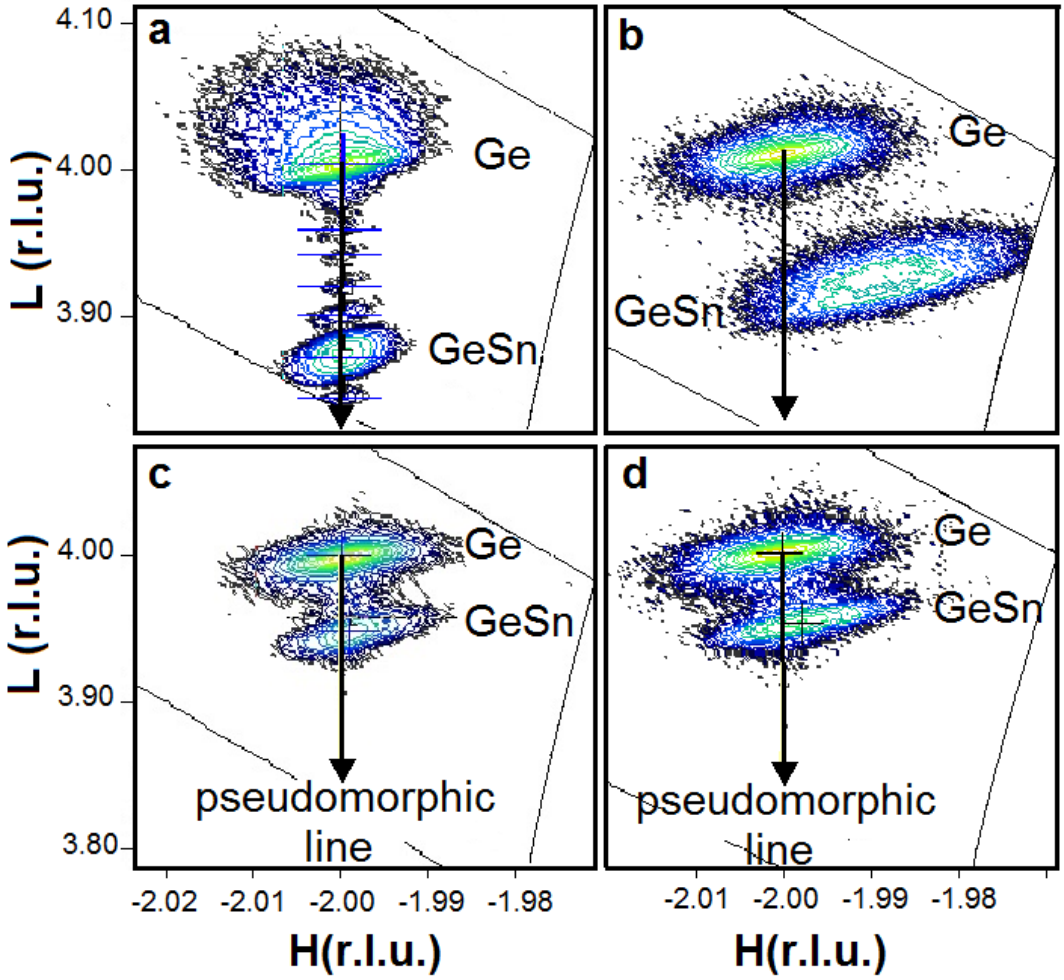

Figure 62. RSMs from (-2 -2 4) plane of GnSn film. (a) RSM of 6.0%, (b) 7.0% Sn. (c, d) The RSM of 3.2% Sn samples for two different thicknesses of 76 nm and 128 nm, respectively.

Compressively strained $Ge_{1-x}Sn_x$ layers can be grown on Ge to a certain thickness which is known as the critical thickness [79]. Lattice mismatch of the Ge and $Ge_{1-x}Sn_x$ causes strain in the $Ge_{1-x}Sn_x$ epi-layer but the film cannot accommodate such high strain beyond the critical thickness. Therefore, it relaxes through the formation of defects (threading or misfit dislocations located at the interface).

The critical thickness is calculated with different methods, such as Matthews-Blakeslee (M-B) model [79] and People-Bean (P-B) model [80]. Calculations for mismatched heteroepitaxial layers are based on the assumption that the material is grown at thermal equilibrium conditions. However, most growth techniques for $Ge_{1-x}Sn_x$ use non-equilibrium conditions. Therefore, finding the critical thickness (h_c) for different materials is difficult. Figure 63 shows two different theoretical calculations for critical thickness of $Ge_{1-x}Sn_x$ films on relaxed Ge for different Sn compositions. Measurements from samples in this work show that critical thickness calculated using the M-B model was more realistic for non-equilibrium growth conditions in comparison to the P-B model.

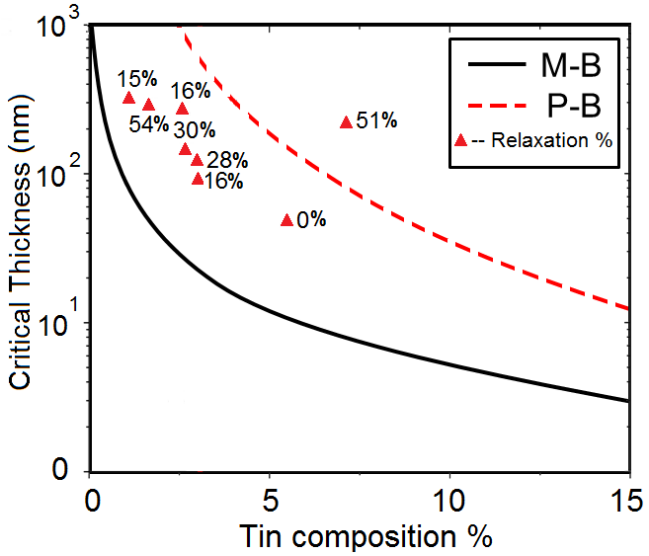

Figure 63. Theoretical calculations for critical thickness of $Ge_{1-x}Sn_x$ films on relaxed Ge buffer layer on Si using Matthew-Blakeslee (M-B) model (red dashed) and People-Bean (P-B) model (black solid).

Additionally, RSMs were used to analyze the quality and crystallinity of the grown films. Surfaces of samples grown with CVD were not as smooth as those grown with MBE, therefore, Kiessig fringes were not observed in the rocking curve or RSM images. However, Figure 62a shows that the $Ge_{.94}Sn_{.06}$ film had higher growth quality with Kiessig fringes. This

could be attributed to optimized Ge buffer growth with low defect densities. Moreover, mosaicity of the films calculated by measuring the broadening $Ge_{1-x}Sn_x$ peak also revealed higher crystal quality for the $Ge_{0.94}Sn_{0.06}$ sample.

Transmission electron microscopy

Crystallinity, defect formation, and defect propagation of $Ge_{1-x}Sn_x$ layers are better investigated using high resolution TEM. Transmission electron microscopy images revealed 100% crystallinity in Ge and $Ge_{1-x}Sn_x$ films. Germanium buffer layers were relaxed as their thicknesses were far above the critical thickness [79]. Consequently, lattice mismatch of Ge and Si caused the film to release the large accumulated energy and relieve the strain by formation of misfit dislocations at the Si/Ge interface (Figure 64). Some of the misfit dislocations were confined at the Si/Ge interface while some became nucleation sites for threading dislocations.

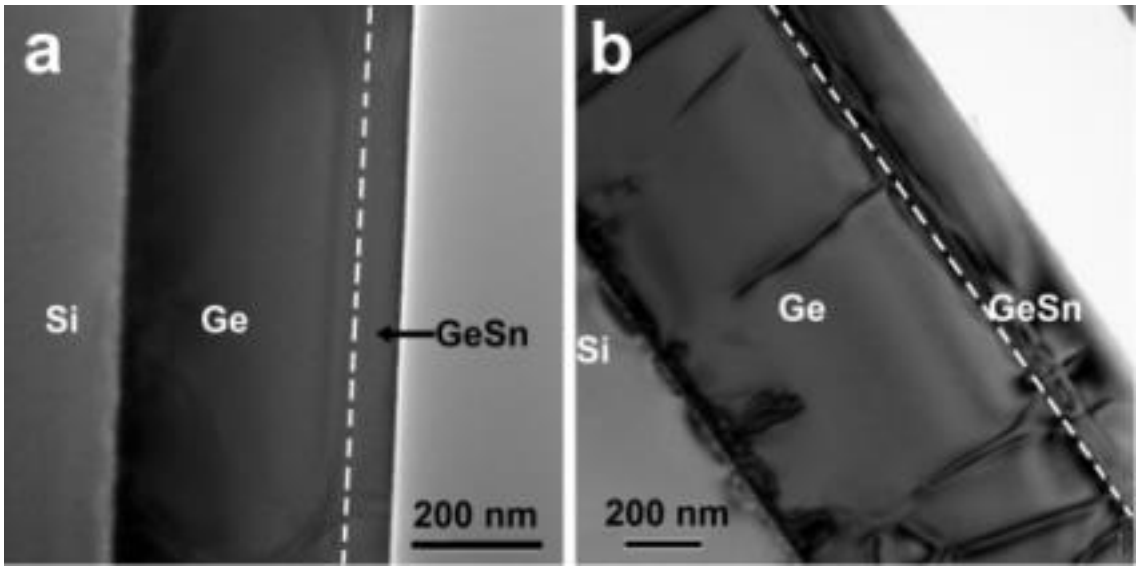

Figure 64. Cross sectional TEM image of 6.0% and 7.0% Sn samples. (a) TEM image of $Si/Ge/Ge_{.94}Sn_{.06}$ and (b) TEM image of $Si/Ge/Ge_{.93}Sn_{.07}$ films.

Germanium films showed a large number of threading dislocations that propagated through the film due to non-optimized growth conditions. This degradation of Ge growth quality (Figure 64b), offered the opportunity to study the propagation of these dislocations through $Ge_{1-x}Sn_x$ film. The average density of threading dislocations in the Ge buffer layer was measured to be 9.71×10^8 cm^2. In Figure 64a, the extracted thickness of the $Ge_{0.94}Sn_{0.06}$ layer was 49 nm. Although the thickness was larger than the critical thickness calculated by M-B model, it was still lower than the P-B model calculation (100 nm). The X-ray diffraction measurement showed that this film was 100% pseudomorphic. The TEM image also verified high material quality of the film as revealed by observation of Kiessig fringes in the RSM image. This was mainly due to optimized growth conditions for the Ge buffer layer in this sample. Figure 64b shows the 240 nm $Ge_{0.93}Sn_{0.07}$ epi-layer grown on 760 nm Ge strain-relaxed buffer. The calculated critical thickness for 7.0% Sn incorporation in Ge was 7 nm using the M-B model (80 nm using P-B model). Therefore, it is expected that $Ge_{1-x}Sn_x$ underwent the relaxation process through misfit dislocations at the Ge/GeSn interface as shown in Figure 65a. The X-ray diffraction analysis revealed that 51% of the strain was relieved which agreed with the observation of threading dislocations and cross-hatch pattern seen in the AFM image (Figure 65b) of the sample.

Investigation of TEM images showed that although misfit dislocations were a source for the generation of threading dislocations, $Ge_{1-x}Sn_x$ layers exhibited 80% fewer propagated threading dislocations than the Ge buffer layer. Figure 64b shows an area where threading dislocations stopped propagating in the $Ge_{0.93}Sn_{0.07}$ film. The density of threading dislocations in $Ge_{0.93}Sn_{0.07}$ films was found to be as low as $3.0\times10^7 cm^{-2}$, which indicated the high quality of the grown film.

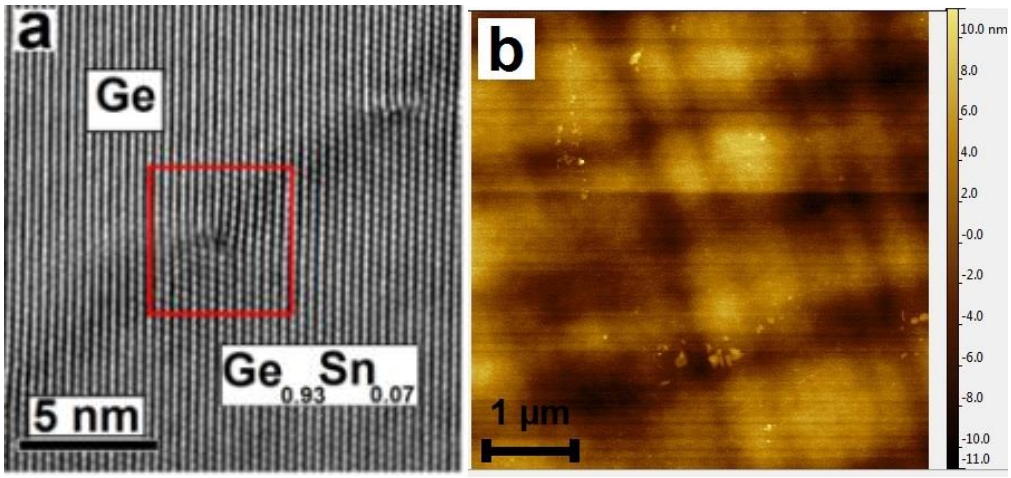

Figure 65. TEM and AFM analysis of 7.0% Sn sample. (a) High resolution TEM image delineation of a misfit dislocation at the interface of Ge/$Ge_{.93}Sn_{.07}$ film. (b) AFM image of the $Ge_{.93}Sn_{.07}$ sample.

6.1.2. Optical characterization

Raman spectroscopy

The comparison of the Raman shift for the Ge-Ge bond in bulk Ge and $Ge_{1-x}Sn_x$ is shown for different Sn% composition in Figure 66. The inset demonstrates the Raman spectrum of the sample with 7.0% Sn incorporation compared to bulk Ge. Increasing the Sn composition reduced the Raman shift from $\omega_0 = 300.00$ cm^{-1} for bulk Ge to $\omega = 296.11$ cm^{-1} for $Ge_{1-x}Sn_x$ alloy with 7.0% Sn composition. Also, there was an additional Raman peak due to the Ge-Sn bonds at 260.86 cm^{-1}. In samples with a lower percentage of Sn, this peak was hardly noticeable. The measured shifts revealed the effect of Sn composition on the $Ge_{1-x}Sn_x$ lattice. Tin incorporation applied a strain on the lattice constant and caused a change in the Raman shift position of $Ge_{1-x}Sn_x$ alloys.

Theoretical calculation of strain contribution on Raman shift of $Ge_{1-x}Sn_x$ alloys are explained in reference 76. The change in Raman shift due to the strain was calculated and compared with the experimental results in Figure 66. Except for p-doped samples, the

experimental and theoretical results were fairly comparable. The change in Raman shift was complicated for different Sn mole fractions and doping, therefore it is not presented here.

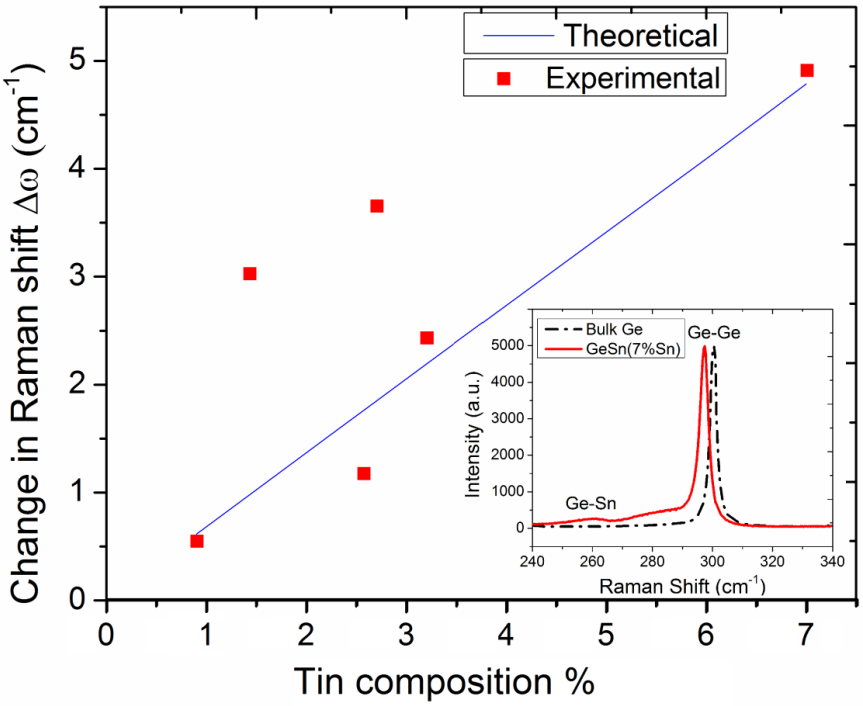

Figure 66. Theoretical calculation of the change in Raman shift for Ge-Ge bonds in strained $Ge_{1-x}Sn_x$ alloys along with measured experimental data. The inset shows Raman shift measurement of $Ge_{.93}Sn_{.07}$ sample.

Spectroscopic ellipsometry

Spectroscopic ellipsometry was employed to measure compositional dependent refractive index (*n*), extinction coefficient (*k*), and absorption coefficient for both bulk Ge and the $Ge_{0.93}Sn_{0.07}$ sample. Figure 67 shows the measured absorption coefficient for $Ge_{0.93}Sn_{0.07}$ compared to Ge from 0.5-2.5 eV.

The comparison shows an increased absorption coefficient below 0.5 eV which includes the wavelengths longer than 1550 nm. This enhanced absorption in the infrared would allow $Ge_{1-x}Sn_x$ active devices to operate at a longer wavelength than Ge. The inset of Figure 67

shows measured refractive index (*n*) and extinction coefficient (*k*) of 7.0% Sn sample and Ge bulk.

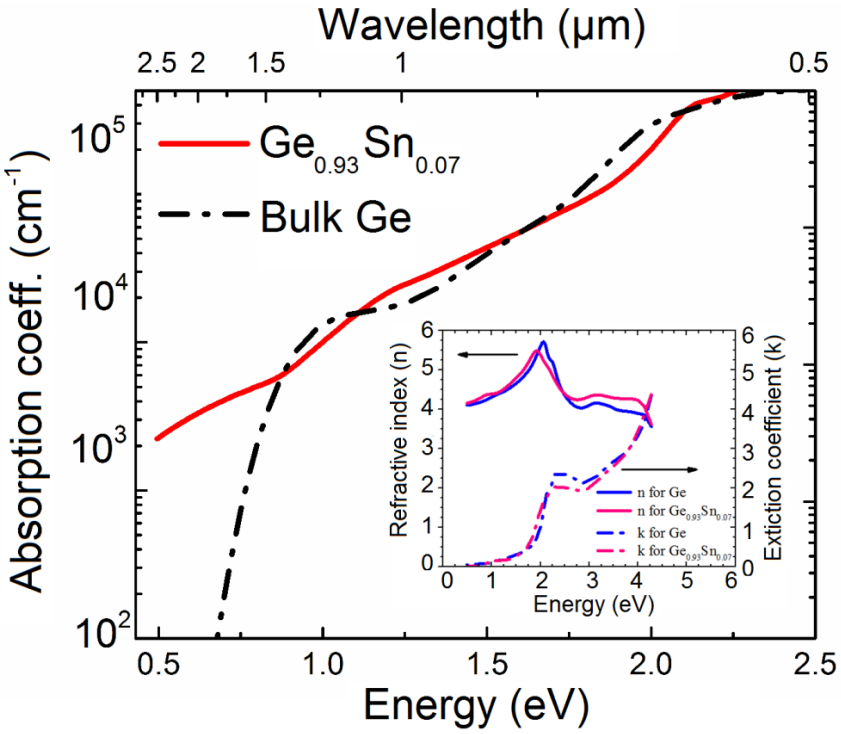

Figure 67. Absorption coefficient of $Ge_{0.93}Sn_{0.07}$ film measured using spectroscopic ellipsometry. The inset shows the refractive index (*n*) and extinction coefficient (*k*) of $Ge_{0.93}Sn_{0.07}$ film compared to bulk Ge.

Photoluminescence

Photoluminescence was used to measure the bandgap edge for the $Ge_{1-x}Sn_x$ samples with various Sn compositions. Figure 68 depicts normalized room temperature PL intensity versus energy for 0-7.0% Sn mole fraction in Ge layers. The measurements were used to analyze the bandgap for the various Sn compositions as well as growth quality. Due to high pumping power of the laser, both direct and indirect transitions were clearly observed. The black solid line shows the PL for Ge buffer grown on Si substrate with a peak around 0.78 eV for direct transition and 0.68 for indirect transition. The difference between PL peak position of Ge layer

bandgap and theoretical calculations of bulk Ge was due to the strain related effects and defects in the crystal structure of Ge buffer layer.

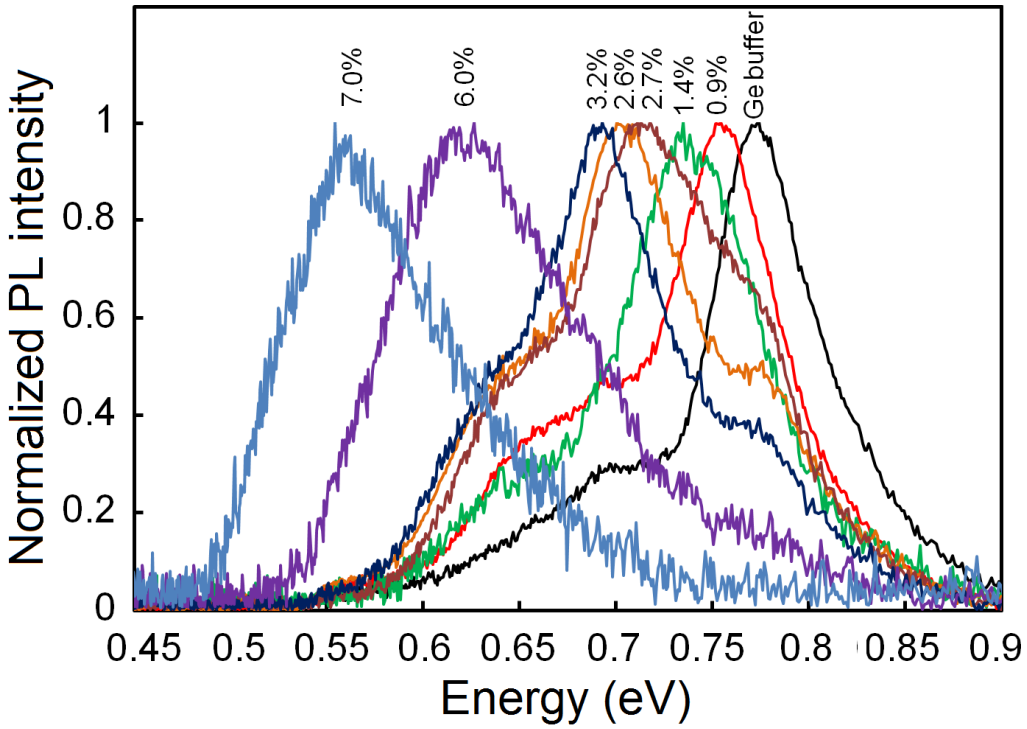

Figure 68. Normalized PL intensity of Ge buffer layer and $Ge_{1-x}Sn_x$ films at room temperature versus PL emission energy.

Incorporation of 0.9% Sn shifted both direct bandgap and indirect bandgap towards lower energies; however, the reduction of the direct bandgap was more than the indirect bandgap. For the 3.2% sample (134 nm thickness), it can be seen that the indirect peak and direct peak have almost overlapped and both can be seen at 0.7 eV. For higher concentrations of Sn, such as 6 and 7.0%, the indirect gap and direct gap were completely overlapped such that direct and indirect PL spectra were not distinguishable. The doped samples with 1.4 and 2.7% Sn samples do not follow the bandgap reduction trend that was observed in the undoped samples.

6.1.3. Discussion

Incorporation of Sn in Ge lattice in near equilibrium growth conditions was a challenging task as solubility of Sn in Ge is very low (0.05%) and the melting point of bulk Sn is 232 °C. Recent studies show that Sn nano-particles have an even lower melting point of 177 °C which exacerbates the conditions [81]. This confirms the creation of a two-phase mixture at growth temperatures above 177 °C. Instability of α-Sn allotrope above 13 °C and 15% larger lattice size increases the possibility of precipitation of Sn out of Ge lattice. Therefore, a non-equilibrium growth condition was needed to suppress the possible phase segregation on the growth surface or within the film. Incorporation of more than 0.5% Sn is considered a supersaturation that may trigger nucleation and accumulation of Sn. This breaks the GeSn matrix to Ge:Sn matrix and, upon continued growth, results in diffusion of the precipitated metal to the top surface thereby completing the phase segregation.

The characterization measurements and analysis quantitatively and qualitatively identify substitutional incorporation of Sn in Ge matrix. Germanium tin lattice constants (in-plane and out-of-plane) were determined by XRD using in-plane and out-of-plane lattice constant and Poisson ratio. Tin content of the $Ge_{1-x}Sn_x$ alloys was calculated using Vegard's law with a bowing factor of b_1^{GeSn} = 0. 468 nm [71] and b_2^{GeSn} = 0.166 nm [72]. Figure 69 depicts the plot of Sn% vs. lattice constant of $Ge_{1-x}Sn_x$ alloy. Composition measurements through SIMS and RBS are also presented in the plot. Calculation of $Ge_{1-x}Sn_x$ lattice constant using the most recent bowing factor, b_2^{GeSn} = 0.166 nm (red line), shows better agreement with experimental data from SIMS and RBS. One such comparison of XRD and SIMS measurement for the 3.2% Sn sample showed 0.21% less Sn incorporated in the lattice.

Although there was good consistency between the measurement methods, SIMS and RBS yielded higher Sn content in the films than XRD. This could have been an indication of Ge:Sn phase segregation on the surface in volume precipitates, or interstitial Sn in Ge matrix. Further investigation of film quality with AFM did not show any trace of Sn precipitation on the surface of the grown alloys. In addition, high resolution cross-sectional TEM images did not show formation of Sn nuclei in the film. This led to the conclusion that Sn was incorporated as interstitial defects or that further theoretical analysis of bowing factors and $Ge_{1-x}Sn_x$ film mechanics was still needed. In addition, this inconsistency was more observable in the doped samples (1.4% and 2.7.0% Sn). The lower size of boron atoms could affect the $Ge_{1-x}Sn_x$ films and result in smaller lattice size.

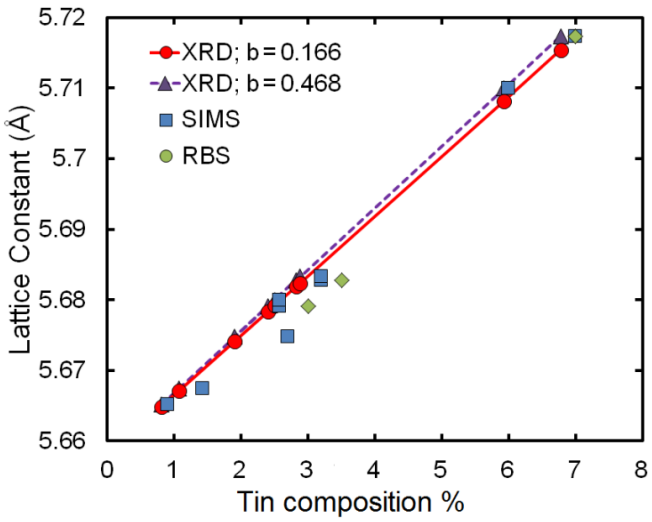

Figure 69. Germanium tin lattice constant of the films vs. Sn composition of $Ge_{1-x}Sn_x$ alloys measured by XRD, SIMS and RBS.

6.2. Defect formation and propagation in GeSn films

The difference in the lattice constant of Si, Ge, and Sn introduces a network of misfit dislocations to relax the biaxial strain in the film. Although a majority of the misfit dislocations

can be trapped, some will thread through the film causing threading dislocations which decreases the performance of the final device [82]. Plastic relaxation of higher lattice constant materials (SiGe, Ge, GeSn) on top of Si forces the layers to form 60^{o} misfit dislocations. These dislocations are caused by slip of (110) and (111) planes in the diamond lattice structure which has a screw component and will thread through the grown film. Growth of low temperature Ge or SiGe film followed by the high temperature growth can be a solution to confine the threading dislocations [83]. Formation of Lomer misfit dislocations can also prevent the propagation of threading dislocations into the top layer. The main reason behind this phenomenon is that the Burgers vector in a Lomer misfit dislocation, for a (001) substrate, lies parallel to the interface. Therefore, the substrate and film lattices can match while no perpendicular component exists. In this case, the film is grown relaxed without introducing structural imperfections such as threading dislocations which degrade the material quality.

Theory of Lomer dislocations was explained by Mader *et al*. [84] in 1974; thereafter, different models were proposed including a five-atom ring and seven-atom ring without dangling bonds [85]. These structural models are derived from high resolution electron microscope images along with image simulations. Available models show that Lomer dislocations can combine two lattices through symmetric and asymmetric loops [86, 87]. In this section, defect formation and propagation mechanism in $Ge_{1-x}Sn_x$ films and its properties of trapping defects on the interface are discussed.

6.2.1. Relaxation theory and TEM analysis

Formation and propagation of defects in the film is a direct consequence of lattice mismatch between the grown layer and the substrate layer. Initially, films could be grown defect- free under full compressive strain but as soon as the layers start to relax the strain,

defects form and propagate through the film. Measurements of strain in the films show that based on the Sn mole fraction and thickness, the samples were relaxed from 0 to 54% as discussed in Section 6.1.1.

Relaxation of the films starts at different thicknesses based on the lattice constant of the $Ge_{1-x}Sn_x$ layers. A higher Sn composition film would have a higher lattice constant and relaxation starts at lower thicknesses. The thickness beyond which the higher lattice constant layer cannot accommodate the strain is the critical thickness. The relaxation process starts by formation of defects, such as misfit dislocations, on the surface which will propagate through the film by threading dislocations.

Large lattice mismatch between Si and Ge (4.2%) causes the Ge buffer layer to release the strain by formation of misfit dislocations at the Ge/Si interface. The Matthews-Blakeslee calculation for critical thickness of Ge growth on Si shows that this process should start after a few nanometers of growth (Section 6.1.1). Figure 70a shows the schematic diagram of the samples with $Ge_{1-x}Sn_x$ layer grown on Ge buffer layer on Si substrate. Formation of 60^o misfit dislocations as a result of plastic relaxation of Ge on top of Si forced the (110) and (111) planes to slip in the diamond lattice structure. The screw component of misfit dislocation will thread through the grown film and form threading dislocations. A cross-hatch pattern is observable as a result of formation of misfit dislocations on the interface of Si/Ge and Ge/GeSn; however, not all the dislocations propagate through the second layer. Figure 70b shows the cross-hatch pattern observed by plan view TEM of the $Ge_{0.93}Sn_{0.07}$ sample. The cross-hatch patterns formed at GeSn/Ge interface overlapped with those of Ge/Si in the image. The denser pattern was attributed to the Ge/Si interface due to higher lattice mismatch. Figure 70c is a scanning electron microscopy image of decorated threading dislocations at the surface delineated using

cold Schimmel solution (CrO_3+HF) for 10 minutes. The density of pits (1.1×10^7 cm^{-2}) was in good agreement with TDD measured from TEM micrographs (3.0×10^7 cm^{-2}) [1]. It also confirms that the quality of GeSn material was better than Ge buffer layer (TDD: 9.71×10^8 cm^{-2}) by an order of magnitude.

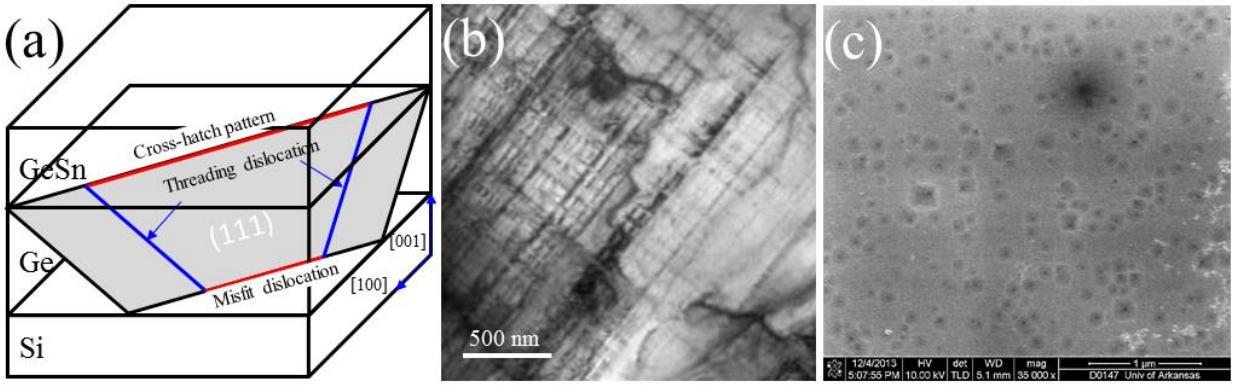

Figure 70. Threading dislocation propagation from Ge buffer to the GeSn top layer. (a) Schematic diagram of threading dislocation propagation (b) Plan view TEM image of $Ge_{0.93}Sn_{0.07}$/Ge/Si(c) SEM image of $Ge_{0.93}Sn_{0.07}$ film exposed to etch pit solution.

Propagation of threading dislocations was studied in Ge buffer and GeSn layer. A higher density of treading dislocations was seen in all the Ge buffer layers. However, localization of threading dislocations was observed on the interface of Ge/GeSn interfaces. Figure 71 shows that the defects had not passed through the GeSn film at several locations.

The TEM images in Figure 71 show the cross-section of Ge buffer layer as well as the $Ge_{0.968}Sn_{0.032}$ layer for two thicknesses of 76 nm (Figure 71a) and 128 nm (Figure 71b). Thinner $Ge_{0.968}Sn_{0.032}$ film (76 nm) in Figure 71a had less relaxation than the thicker $Ge_{0.968}Sn_{0.032}$ film (128 nm) in Figure 71b, nonetheless, no cross-hatch pattern was observed on the surface of either film. This indicated misfit dislocations were not propagated through the GeSn film.

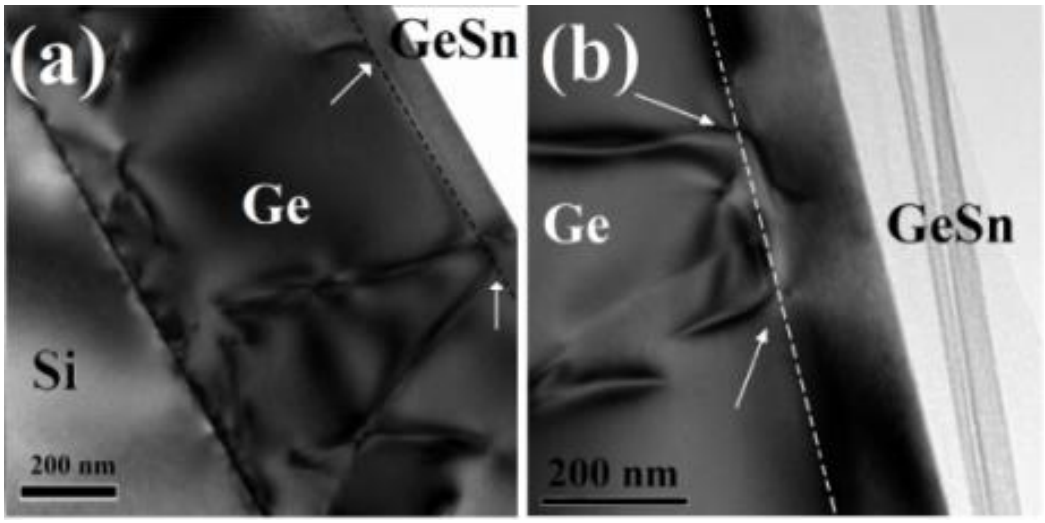

Figure 71. Transmission electron microscopy of $Ge_{.968}Sn_{.032}$/Ge films grown on Si substrate. (a) GeSn film with 76 nm thickness; (b) GeSn with 128 nm thickness.

Higher density of threading dislocations in the Ge buffer layer gave lower quality of the film, however, it had provided the opportunity to investigate defect propagation in the $Ge_{1-x}Sn_x$ film. The TEM image in Figure 71b shows that the $Ge_{1-x}Sn_x$ layer can lock the threading dislocations that are being propagated through the film at the GeSn/Ge interface. No threading dislocations were formed at the $Ge_{1-x}Sn_x$/Ge interface; however, some of the threading dislocations were able to pass through the $Ge_{1-x}Sn_x$ film. As a result of this phenomenon, the average density of threading dislocation in the $Ge_{1-x}Sn_x$ layer was far less than the Ge buffer layer. The measurements show that the density of threading dislocations in the Ge buffer layer was 7.1×10^{8} cm^{-2} while that of the $Ge_{1-x}Sn_x$ layer is 5.0×10^{7} cm^{-2}. This phenomenon was also seen in TEM images of different Sn mole fraction films.

6.2.2. Formation of Lomer misfit dislocations

Figure 72a shows the structure of $Ge_{0.93}Sn_{0.07}$ layer on Ge buffer. The thickness of this layer was 240 nm and the Ge buffer was 760 nm. The critical thickness of such GeSn structures

was calculated to be 7 nm by M-B model and 80 nm by P-B model. Therefore, the 240 nm $Ge_{0.93}Sn_{0.07}$ layer underwent a relaxation process through formation of a network of misfit dislocations on the surface and propagation of threading dislocations throughout the film.

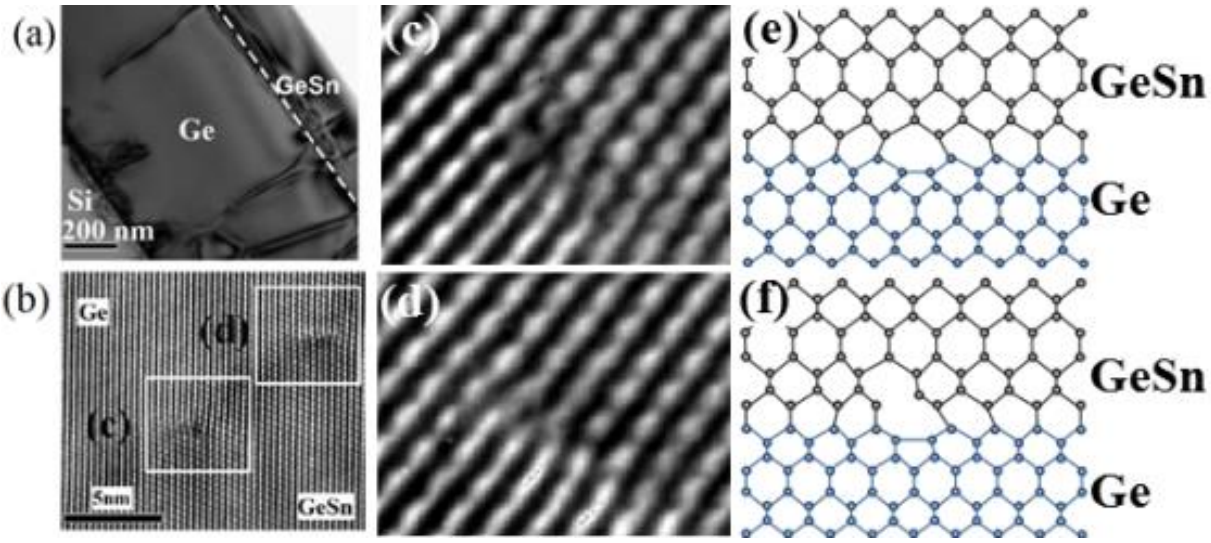

Figure 72. TEM image of $Ge_{.93}Sn_{.07}$/Ge/Si film and atomic models of GeSn and Ge. (a) Low resolution TEM of the $Ge_{.93}Sn_{.07}$/Ge/Si film. (b) High resolution TEM image of misfit dislocations at the interface of $Ge_{.93}Sn_{.07}$/Ge film. Symmetrical (c) and asymmetrical (d) misfit dislocation observed at the GeSn/Ge interface [the white boxes in (b) are rotated 45^o CCW]. (e ,f) The atomic models of (c) and (d).

Figure 72b shows misfit dislocations at two points. This is in agreement with the XRD analysis that showed 52% relaxation and a network of cross-hatch pattern that may be seen in the plan view TEM image (Figure 70b). Measurement of the TDD in Ge buffer layer and GeSn film showed that 80% of threading dislocations were trapped at the interface of Ge/GeSn (Figure 72a). The density of threading dislocations in $Ge_{1-x}Sn_x$ films was measured to be as low as 3.0×10^7 cm^{-2}, which indicated a higher quality of the grown film with respect to the Ge buffer layer.

Misfit dislocations can also form Lomer dislocations [88] on the surface by forming closed loops at the GeSn/Ge interface. Formation of such dislocations stops propagation of defects along the growth direction. A Lomer misfit dislocation is a 90^o misfit dislocation that does not have a screw component in contrast to the regular 60^o misfit dislocation. Formation of his kind of misfit dislocation at the GeSn/Ge interface leads to less threading dislocations in the $Ge_{1-x}Sn_x$ films. Figure 72c (rotated 45^o CCW) shows the higher magnification of Lomer dislocations that formed a symmetrical Lomer dislocation. Other kinds of Lomer misfit dislocations are also observable at the interface as shown in Figure 72d (rotated 45^o CCW) ─ an asymmetrical Lomer dislocation. Different models may be fit to the Lomer dislocations to show how the atoms are placed to relieve the stress and keep the top surface defect free. The most recurrent Lomer dislocations are presented in Figure 72 (e, f). Figure 72e and f show a seven-atom-ring symmetrical and an eleven-atom-ring asymmetrical Lomer dislocation, respectively.

6.3. Thermal annealing of GeSn samples for strain relaxation

Incorporation of Sn into the Ge lattice reduces the height of the Γ valley at a faster rate than that of the L valley. Indirect-direct crossover is achieved with ~8% Sn incorporation [28]; however, strain in the lattice changes the predicted bandgap [89]. Germanium tin layers are grown compressively strained due to a lattice constant of GeSn higher than that of Ge and Si. This compressive strain requires more Sn for a direct bandgap, while tensile strained GeSn films can achieve direct bandgap at lower Sn compositions. Several studies have been performed for this purpose but due to the variety of structures and film thicknesses, the results are not complete yet [41, 90, 91]. Roucka *et al.* investigated rapid thermal annealing of GeSn/Si structures [90]. In another recent study, post growth annealing was performed on a 30 nm

$Ge_{0.9}Sn_{0.1}$/Ge/Si sample for only one composition [41]. Li *et al*. reported on strain relaxation of a $Ge_{0.9218}Sn_{0.0782}$ film in the range of 440-540 °C [91]. In this section, studies of strain relaxation and material quality enhancement of GeSn layers through cyclic annealing at temperatures between 450 - 500 °C are presented.

6.3.1. Experimental setup

The annealing process was conducted after growth in a rapid thermal annealing (RTA) system. The samples were kept in nitrogen ambient during the process to avoid thermal oxidization. The temperature was controlled through a feedback loop pyrometer and a thermocouple.

6.3.2. Results and discussion

The as-grown samples measured 51-100% compressive strain. Samples were then annealed at 450-500 °C for 1-4 cycles. Figure 73 shows the out-of-plane lattice constant of the annealed samples measured by an XRD 2Theta-Omega rocking curve. Change in the out-of plane lattice constant was attributed to either strain relaxation, or to Sn precipitation on the surface of the film. Relaxation of compressively strained samples resulted in reduction of the out-of-plane lattice constant. The results in Figure 73 indicate that higher temperature and more cycles gave a greater reduction in the out-of-plane lattice constant.

The as-grown $Ge_{0.94}Sn_{0.06}$ sample had 76 nm thickness and was 100% pseudomorphic before annealing. The RSM technique shows both in-plane and out-of-plane lattice constants of the GeSn layers. Figure 74a shows the effect annealing had on the of out-of-plane lattice constant of the $Ge_{0.93}Sn_{007}$ sample that was initially 49% compressively strained and had a thickness of 240 nm. Examination of Figure 74a shows that annealing at 500 °C reduced the

out of plane lattice constant as well as the FWHM of the GeSn XRD peak. This indicates that the material quality improved. The RSM scan of the as-grown $Ge_{0.93}Sn_{007}$ sample in Figure 47 b shows that the GeSn peak was between the vertical pseudomorphic line and relaxation line. Figure 47c shows that annealing the sample for three cycles of 30 s duration at 500 ^{o}C pushed the GeSn peak towards the relaxation line and reduced the FWHM.

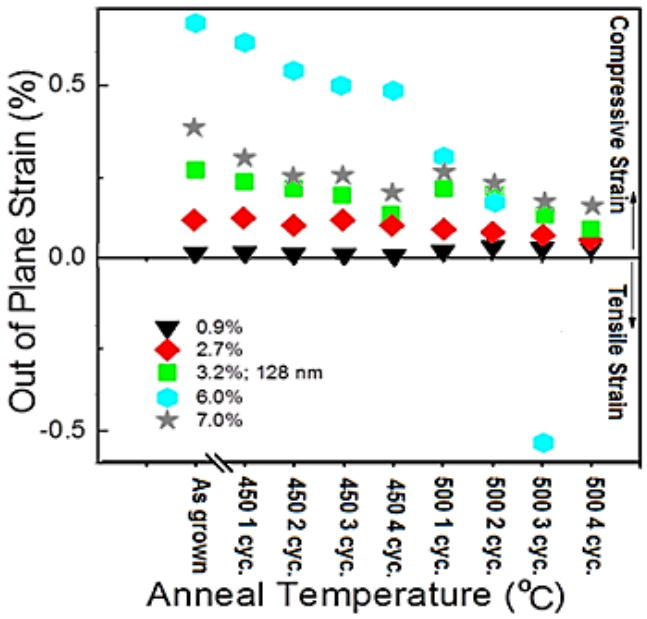

Figure 73. Out-of-plane strain of GeSn film annealed for 1-4 cycles at 450-500 °C for 30 sec.

The PL spectra of the samples were collected by an off-axis set-up using a 690 nm femto second pulsed laser source. The PL spectra in Figure 75a shows that annealing at 450 °C for 2 cycles reduced the FWHM of the as-grown film from 0.33 to 0.27 eV. The peak position of the PL spectrum for the annealed sample at 450 °C and 2 cycles red shifted which indicates a reduction in the band gap as expected for less strained films [89]. It can be seen that annealing at 500 °C was detrimental to the film quality. Figure 75b-d show the RSM scans of the as grown and annealed samples at 500 °C for one cycle and three cycles, respectively. Movement of the GeSn peak towards the relaxation line showed a reduction in compressive strain, but the

increase in the XRD FWHM of the GeSn peak indicated material degradation. Additionally, the total lattice constant of the film was reduced which indicated Sn segregation out of the GeSn lattice.

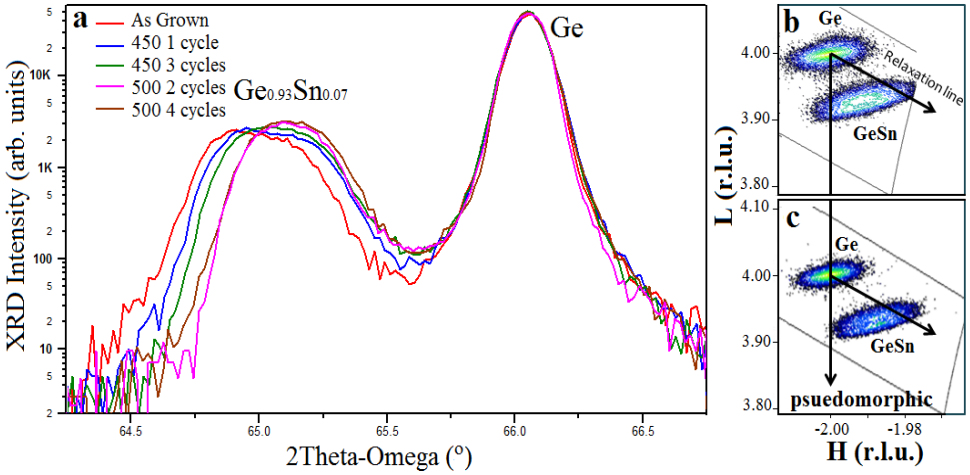

Figure 74. XRD analysis of the $Ge_{0.93}Sn_{0.07}$ sample treated with cyclic anealing. (a) The XRD 2Theta-Omega rocking curve of $Ge_{0.93}Sn_{0.07}$ annealed for 30 s at 450 °C for 1 and 3 cycles and at 500 °C for 2 and 4 cycles. (b) RSM of the as-grown film and (c) annealed sample for 4 cycles of 30 s at 500 °C.

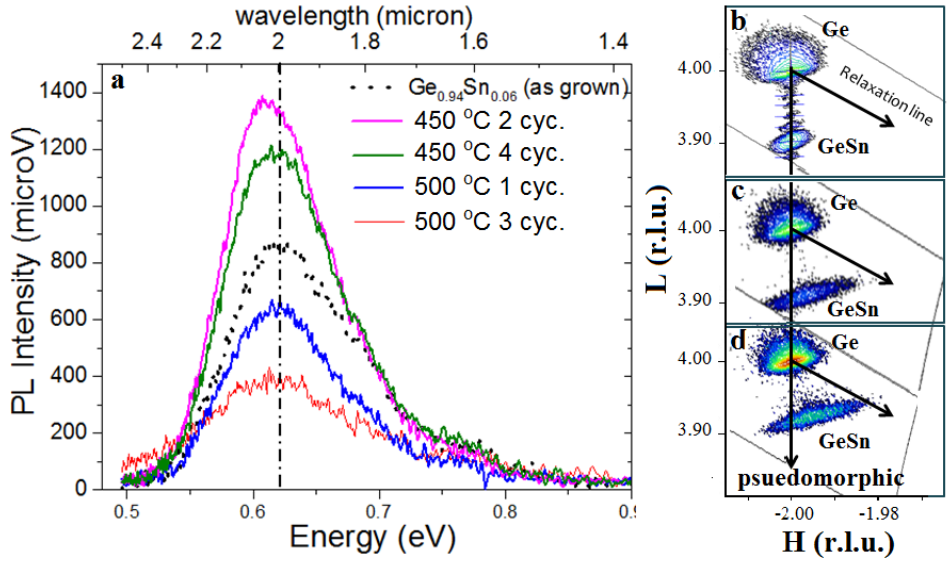

Figure 75. Optical and material characterization of $Ge_{0.94}Sn_{0.06}$ sample treated with cyclic annealing. (a) PL spectra for the $Ge_{0.94}Sn_{0.06}$ as grown and annealed films at 450 °C for 2 and 4, and at 500 °C for 1 and 3 cycles of 30 s. (b) RSM of the as grown sample, (c) annealed at 500 °C for 1 cycle of 30 s, and (d) 3 cycles of 30 s.

Chapter 7. Summary and future work

7.1. Summary

In this research, low temperature growth of Si-Ge-Sn alloys was studied. A systematic study was done in order to use commercially available gases of silane and germane for the growth of the Si-Ge-Sn materials. A plasma-enhanced CVD process was employed as the method to lower the growth temperature of Si from 1000 °C to 250 °C. Achievement of high quality Si homoepitaxy showed the effectiveness of using this method for low temperature Si Epitaxy. In the growth of Ge and SiGe films, an RPCVD method was used and the effect of higher pressure growth was studied for higher material quality and higher Si incorporation at lower temperatures. The results show that increasing the growth pressure from 0.1 torr to 1 torr resulted in higher film quality and doubling the Si incorporation in the films. Characterizations using XRD showed Si incorporation as much as 17% at the growth temperature of 450 °C. These results were used for benchmarking the GeSn and SiGeSn growth using the RPCVD method. In addition, the effect of different carrier gases (Ar, H_2 and N_2) in the growth of Ge films was studied and showed that higher quality films were achieved using Ar.

Direct growth of GeSn and SiGeSn films on Si substrates was achieved using an RPCVD method. The films were grown using two different methods of Sn delivery for the stannic chloride and deuterated stannane precursors. Characterization showed successful incorporation of Sn up to 7% in the growth with stannic chloride without using a carrier gas. However, it was observed that usage of stannic chloride resulted in etching of the films as they were grown. This etching behavior was attributed to the production of HCl which is an etchant of Ge. Therefore, no growth was observed in high flow rates of stannic chloride. A similar trend was observed in the growth for SiGeSn films using stannic chloride. However, uniform

epitaxial $Si_yGe_{1-x-y}Sn_x$ films with different Si and Sn compositions ($0.02 \leq x \leq 0.05$, $0.03 \leq y \leq 0.05$) were achieved in the conditions away from the etching regime. In order to improve the film quality, Ar was used as a carrier gas with low flow rates of stannic chloride. Optical characterization of the samples showed that more than four times higher PL intensities were achievable by introduction of Ar as carrier gas and an increase in the temperature. The material characterization showed that an increase in the growth pressure from 0.1 torr to 0.5 torr resulted in higher Sn incorporation, PL intensity, and film thickness. In order to achieve more robust growth of GeSn and SiGeSn films, an innovative method of in-situ gas mixing silane and germane with deuterated stannane was adopted. Material characterizations showed incorporation of 2% Sn and up to 17% Si in the lattices.

Material characterization of the compressively strained GeSn films on Ge buffer showed that high quality films could be achieved using a commercially available large-area CVD system. Study of defect formation and propagation in these films showed that formation of symmetrical and asymmetrical Lomer misfit dislocations at the GeSn/Ge interface played a big role in the high quality GeSn film growth. Such a characteristic makes GeSn a unique candidate for a universal compliant layer on which different lattice mismatched films could be grown. Additionally, cyclic annealing of the GeSn epi-layers resulted in the reduction of compressive strain in the films as well as enhancement of material quality. However, the appropriate recipes were different depending on the Sn mole fraction and epi-layer thickness. Lower film thicknesses required lower temperatures to suppress segregation, while lower Sn content material needed more annealing cycles.

7.2. Future work

7.2.1. High pressure growth

Study of the effect of pressure on the growth of the films showed that higher material quality could be achieved by increasing the growth pressure. It was also observed that reduction of material quality and Si incorporation at low temperature growth could be compensated by increasing the growth pressure in Ge and SiGe films. Therefore, it is expected that growth of high quality GeSn and SiGeSn films could be achieved at high growth pressures.

7.2.2. Plasma enhancement

Increasing Sn composition and material quality of the Si-Ge-Sn alloys is a challenge for fabrication of efficient devices. There is a trade-off between these two since higher Sn is incorporated at lower temperature and higher quality is achieved at higher temperatures. In order to tackle this challenge, methods that promote growth away from thermal equilibrium conditions is required. In this regard, plasma enhanced growth of GeSn materials is of great importance. As was discussed in Chapter 3, low temperature and high quality Si growth is possible using plasma enhanced CVD. Therefore, growth of Si-Ge-Sn alloys needs to be studied using this method.

7.2.3. Atomic source

The second method that can serve the same purpose is using an atomic source for breaking the atomic bonds of the molecules and promoting lower temperature growth. Figure 76 shows the schematic of an atomic source that is composed of a gas inlet and a tungsten filament. The filament is covered with a stainless steel shield to keep the flow of the gas toward the filament. This method could be used to produce highly reactive radicals of hydrogen, silane,

and methane. Incorporation of Si and C at low temperature is more challenging due to higher stability of the molecules and this method will help by breaking silane and methane to their radicals of SiH_x and CH_x, respectively.

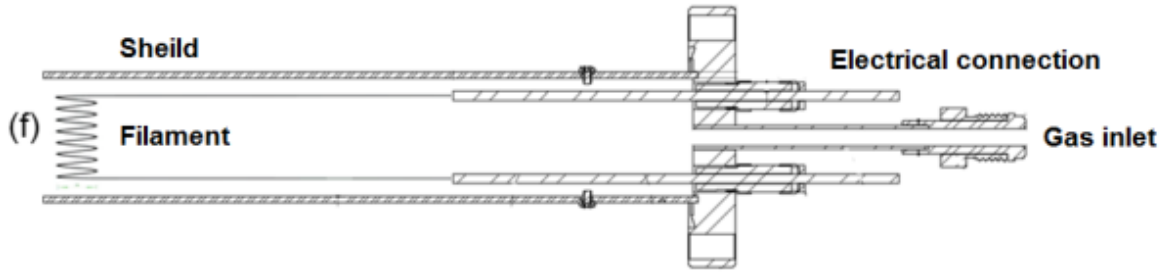

Figure 76. Atomic source for production of highly reactive radicals of gases.

7.2.4. Deuterated stannane gas mixing

Deposition of GeSn and SiGeSn materials using SnD_4 resulted in more robust growth and higher film quality; however, Sn incorporation higher than 2% was not achieved using in-situ gas mixing. Higher flow of pure SnD_4 resulted in poor film quality; therefore, diluting gas with the proper carrier gas is a potential solution to overcome this problem. Figure 77 shows the design of a SnD_4 gas mixing system. A pressure based system is proposed in order to dilute the SnD_4 gas with a diluent gas. The SnD_4 gas would be stored at liquid nitrogen temperature (-200 °C) to be safe from decomposition and warmed up to dry ice temperature (-80 °C) to increase the vapor pressure.

The mixing bottle would be pressurized to the required pressure and the pressure monitored with the pressure gauge. The diluent gas (Ar, H_2 or N_2) would be used to raise the total pressure to reach the planned dilution ratio. A ferromagnetic stirring motor would be used at the bottom of the bottle in order to reduce the time needed to mix the gases. The presence of SnD_4 would be tested by a residual gas analyzer prior to entering the gas manifold. The bottle

would be pumped down every day after finishing the runs. This would reduce the possibility of Sn deposition in the mixing bottle as presence of solid Sn promotes decomposition of the SnD_4 gas.

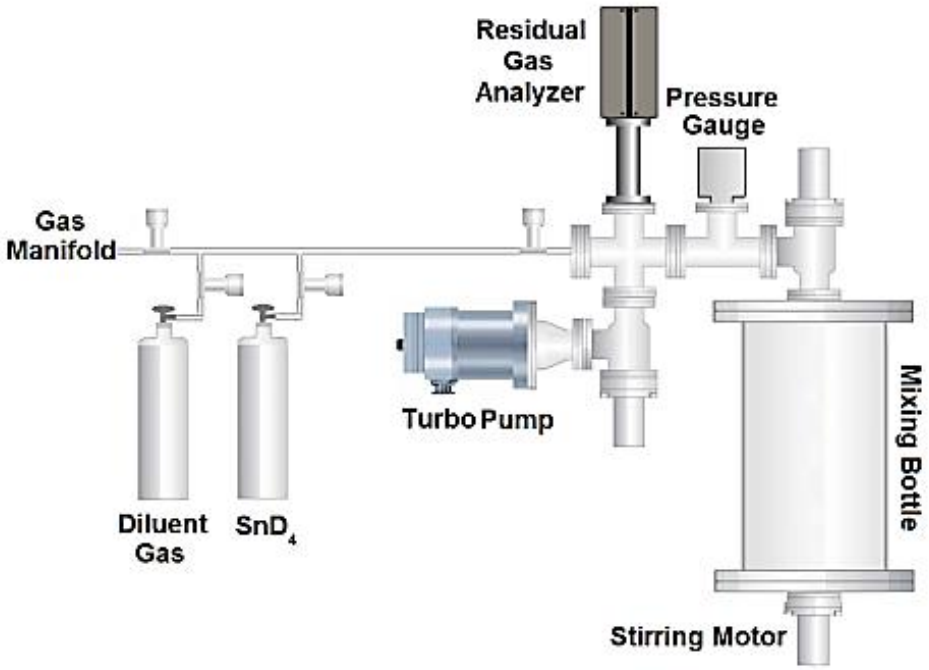

Figure 77. Design of SnD_4 gas mixing system. The system is composed of a mixing bottle, a stirring motor, a vacuum gauge, a residual gas analyzer, and a turbo pump.

References

[1] D. A. Miller, "Physical reasons for optical interconnection," *Int. J. Optoelectron.,* vol. 11, pp. 155-168, 1997.

[2] D. A. Miller, "Rationale and challenges for optical interconnects to electronic chips," *Proc IEEE,* vol. 88, pp. 728-749, 2000.

[3] D. A. Miller, "Device requirements for optical interconnects to silicon chips," *Proc IEEE,* vol. 97, pp. 1166-1185, 2009.

[4] D. A. Miller, "Energy consumption in optical modulators for interconnects," *Optics Express,* vol. 20, pp. A293-A308, 2012.

[5] C. Debaes, A. Bhatnagar, D. Agarwal, R. Chen, G. Keeler, N. C. Helman, H. Thienpont and D. A. Miller, "Receiver-less optical clock injection for clock distribution networks," *Selected Topics in Quantum Electronics, IEEE Journal of,* vol. 9, pp. 400-409, 2003.

[6] S. A. Ghetmiri, W. Du, Y. Zhou, J. Margetis, T. Pham, A. Mosleh, B. Conley, A. Nazzal, G. Sun and R. Soref, "Temperature-dependent characterization of $G_{0.94}Sn_{0.06}$ light-emitting diode grown on si via CVD," in *CLEO: Applications and Technology,* 2015, pp. ATu1J. 6.

[7] W. Du, Y. Zhou, S. A. Ghetmiri, A. Mosleh, B. R. Conley, A. Nazzal, R. A. Soref, G. Sun, J. Tolle and J. Margetis, "Room-temperature electroluminescence from $Ge/Ge_{1-x}Sn_x/Ge$ diodes on Si substrates," *Appl. Phys. Lett.,* vol. 104, pp. 241110, 2014.

[8] J. Kouvetakis, J. Menendez and R. A. Soref, "Strain-engineered direct-gap Ge/Sn_xGe_{1-x} heterodiode and multi-quantum-well photodetectors, laser, emitters and modulators grown on SnySizGe1-yz-buffered silicon," Patent publication #: US6897471 B1, 2005.

[9] M. E. Groenert, C. W. Leitz, A. J. Pitera, V. Yang, H. Lee, R. J. Ram and E. A. Fitzgerald, "Monolithic integration of room-temperature cw GaAs/AlGaAs lasers on Si substrates via relaxed graded GeSi buffer layers," *J. Appl. Phys.,* vol. 93, pp. 362-367, 2003.

[10] R. E. Camacho-Aguilera, Y. Cai, N. Patel, J. T. Bessette, M. Romagnoli, L. C. Kimerling and J. Michel, "An electrically pumped germanium laser," *Optics Express,* vol. 20, pp. 11316-11320, 2012.

[11] O. Jambois, F. Gourbilleau, A. J. Kenyon, J. Montserrat, R. Rizk and B. Garrido, "Towards population inversion of electrically pumped Er ions sensitized by Si nanoclusters," *Optics Express,* vol. 18, pp. 2230-2235, 2010.

[12] R. A. Soref and C. H. Perry, "Predicted band gap of the new semiconductor SiGeSn," *J. Appl. Phys.,* vol. 69, pp. 539-541, 1991.

[13] S. A. Ghetmiri, W. Du, J. Margetis, A. Mosleh, L. Couser, B. R. Conley, L. Domulevicz, A. Nazzal, G. Sun, R. A. Soref, J. Tolle, B. Li, H. A. Naseem and S. Yu, "Direct-bandgap GeSn grown on Silicon with 2230 nm photoluminescence," *Applied Physics Letters,* vol. 105, pp. 151109, 2014.

[14] S. A. Ghetmiri, W. Du, B. R. Conley, A. Mosleh, A. Nazzal, G. Sun, R. A. Soref, J. Margetis, J. Tolle, H. A. Naseem and S. Yu, "Shortwave-infrared photoluminescence from $Ge_{1-x}Sn_x$ thin films on silicon," *Journal of Vacuum Science & Technology B,* vol. 32, pp. 060601, 2014.

[15] V. D'Costa, Y. Fang, J. Tolle, J. Kouvetakis and J. Menéndez, "Ternary GeSiSn alloys: New opportunities for strain and band gap engineering using group-IV semiconductors," *Thin Solid Films,* vol. 518, pp. 2531-2537, 2010.

[16] P. Moontragoon, R. Soref and Z. Ikonic, "The direct and indirect bandgaps of unstrained SixGe1− x− ySny and their photonic device applications," *J. Appl. Phys.,* vol. 112, pp. 073106, 2012.

[17] G. Sun, R. Soref and H. Cheng, "Design of an electrically pumped SiGeSn/GeSn/SiGeSn double-heterostructure midinfrared laser," *J. Appl. Phys.,* vol. 108, pp. 033107-033107-6, 2010.

[18] G. Sun, R. Soref and H. Cheng, "Design of a Si-based lattice-matched room-temperature GeSn/GeSiSn multi-quantum-well mid-infrared laser diode," *Optics Express,* vol. 18, pp. 19957-19965, 2010.

[19] H. Baker and H. Okamoto, "ASM handbook," *Alloy Phase Diagrams,* vol. 3, pp. 965, 1992.

[20] Y. Luo, *Comprehensive Handbook of Chemical Bond Energies.* CRC press, 2010.

[21] A. Harwit, P. Pukite, J. Angilello and S. Iyer, "Properties of diamond structure SnGe films grown by molecular beam epitaxy," *Thin Solid Films,* vol. 184, pp. 395-401, 1990.

[22] T. Maruyama and H. Akagi, "Thin Films of Amorphous Germanium-Tin Alloys Prepared by Radio-Frequency Magnetron Sputtering," *J. Electrochem. Soc.,* vol. 145, pp. 1303-1305, 1998.

[23] R. Lieten, S. Decoster, M. Menghini, J. W. Seo, A. Vantomme and J. P. Locquet, "Single crystalline GeSn on silicon by solid phase crystallization," in *ECS transaction,* pp. 3219-3219, 2012.

[24] H. Li, J. Brouillet, A. Salas, I. Chaffin, X. Wang and J. Liu, "Low Temperature Geometrically Confined Growth of Pseudo Single Crystalline GeSn on Amorphous Layers for Advanced Optoelectronics," *ECS Transactions,* vol. 64, pp. 819-827, 2014.

[25] J. Tolle, A. Chizmeshya, Y. Fang, J. Kouvetakis, V. D'Costa, C. Hu, J. Menendez and I. Tsong, "Low temperature chemical vapor deposition of Si-based compounds via SiHSiHSiH: Metastable SiSn⁄GeSn⁄Si (100) heteroepitaxial structures," *Appl. Phys. Lett.,* vol. 89, pp. 231924, 2006.

[26] J. Kouvetakis, J. Mathews, R. Roucka, A. V. G. Chizmeshya, J. Tolle and J. Menendez, "Practical Materials Chemistry Approaches for Tuning Optical and Structural Properties of Group IV Semiconductors and Prototype Photonic Devices," *Photonics Journal, IEEE,* vol. 2, pp. 924-941, 2010.

[27] J. Werner, M. Oehme, M. Schmid, M. Kaschel, A. Schirmer, E. Kasper and J. Schulze, "Germanium-tin pin photodetectors integrated on silicon grown by molecular beam epitaxy," *Appl. Phys. Lett.,* vol. 98, pp. 061108-061108-3, 2011.

[28] R. Chen, H. Lin, Y. Huo, C. Hitzman, T. I. Kamins and J. S. Harris, "Increased photoluminescence of strain-reduced, high-Sn composition $Ge_{1-x}Sn_x$ alloys grown by molecular beam epitaxy," *Appl. Phys. Lett.,* vol. 99, pp. 181125, 2011.

[29] M. Oehme, D. Buca, K. Kostecki, S. Wirths, B. Holländer, E. Kasper and J. Schulze, "Epitaxial growth of highly compressively strained GeSn alloys up to 12.5% Sn," *J. Cryst. Growth,* vol. 384, pp. 71-76, 2013.

[30] S. Stefanov, J. Conde, A. Benedetti, C. Serra, J. Werner, M. Oehme, J. Schulze, D. Buca, B. Holländer and S. Mantl, "Laser synthesis of germanium tin alloys on virtual germanium," *Appl. Phys. Lett.,* vol. 100, pp. 104101, 2012.

[31] S. Takeuchi, A. Sakai, K. Yamamoto, O. Nakatsuka, M. Ogawa and S. Zaima, "Growth and structure evaluation of strain-relaxed $Ge_{1-x}Sn_x$ buffer layers grown on various types of substrates," *Semiconductor Science and Technology,* vol. 22, pp. S231, 2007.

[32] L. Wang, S. Su, W. Wang, X. Gong, Y. Yang, P. Guo, G. Zhang, C. Xue, B. Cheng and G. Han, "Strained germanium–tin (GeSn) p-channel metal-oxide-semiconductor field-effect-transistors (p-MOSFETs) with ammonium sulfide passivation," *Solid-State Electronics,* vol. 83, pp. 66-70, 2013.

[33] O. Gurdal, P. Desjardins, J. Carlsson, N. Taylor, H. Radamson, J. Sundgren and J. Greene, "Low-temperature growth and critical epitaxial thicknesses of fully strained metastable $Ge_{1-x}Sn_x$ ($x \lesssim 0.26$) alloys on Ge (001) 2× 1," *J. Appl. Phys.,* vol. 83, pp. 162-170, 1998.

[34] N. Bhargava, M. Coppinger, J. P. Gupta, L. Wielunski and J. Kolodzey, "Lattice constant and substitutional composition of GeSn alloys grown by molecular beam epitaxy," *Appl. Phys. Lett.,* vol. 103, pp. 041908, 2013.

[35] S. Kim, J. Gupta, N. Bhargava, M. Coppinger and J. Kolodzey, "Current–Voltage Characteristics of GeSn/Ge Heterojunction Diodes Grown by Molecular Beam Epitaxy," *Electron Device Letters, IEEE,* vol. 34, pp. 1217-1219, 2013.

[36] Y. Soo, T. Wu, Y. Chen, Y. Shiu, H. Peng, Y. Tsai, P. Liao, Y. Zheng, S. Chang and T. Chan, "Substitutional incorporation of Sn in compressively strained thin films of heavily-alloyed $Ge_{1-x}Sn_x$/Ge semiconductor probed by x-ray absorption and diffraction methods," *Semiconductor Science and Technology,* vol. 29, pp. 115008, 2014.

[37] S. Shao-Jian, H. Gen-Quan, Z. Dong-Liang, Z. Guang-Ze, X. Chun-Lai, W. Qi-Ming and C. Bu-Wen, "Strained Germanium-Tin pMOSFET Fabricated on a Silicon-on-Insulator Substrate with Relaxed Ge Buffer," *Chinese Physics Letters,* vol. 30, pp. 118501, 2013.

[38] L. Jiang, C. Xu, J. D. Gallagher, R. Favaro, T. Aoki, J. Menéndez and J. Kouvetakis, "Development of Light Emitting Group IV Ternary Alloys on Si Platforms for Long Wavelength Optoelectronic Applications," *Chemistry of Materials,* vol. 26, pp. 2522-2531, 2014.

[39] M. Bauer, C. Ritter, P. Crozier, J. Ren, J. Menendez, G. Wolf and J. Kouvetakis, "Synthesis of ternary SiGeSn semiconductors on Si (100) via Sn_xGe_{1-x} buffer layers," *Appl. Phys. Lett.,* vol. 83, pp. 2163-2165, 2003.

[40] B. Vincent, F. Gencarelli, H. Bender, C. Merckling, B. Douhard, D. H. Petersen, O. Hansen, H. Henrichsen, J. Meersschaut and W. Vandervorst, "Undoped and in-situ B doped GeSn epitaxial growth on Ge by atmospheric pressure-chemical vapor deposition," *Appl. Phys. Lett.,* vol. 99, pp. 152103-152103-3, 2011.

[41] R. Chen, Y. Huang, S. Gupta, A. C. Lin, E. Sanchez, Y. Kim, K. C. Saraswat, T. I. Kamins and J. S. Harris, "Material characterization of high Sn-content, compressively-strained GeSn epitaxial films after rapid thermal processing," *J. Cryst. Growth,* vol. 365, pp. 29-34, 2013.

[42] S. Wirths, D. Buca, G. Mussler, A. Tiedemann, B. Holländer, P. Bernardy, T. Stoica, D. Grützmacher and S. Mantl, "Reduced Pressure CVD Growth of Ge and $Ge_{1-x}Sn_x$ Alloys," *ECS Journal of Solid State Science and Technology,* vol. 2, pp. N99-N102, 2013.

[43] S. Wirths, D. Buca, Z. Ikonic, P. Harrison, A. Tiedemann, B. Holländer, T. Stoica, G. Mussler, U. Breuer and J. Hartmann, "SiGeSn growth studies using reduced pressure chemical vapor deposition towards optoelectronic applications," *Thin Solid Films,* vol. 557, pp. 183-187, 2014.

[44] J. Tolle, "Methods of forming films including germanium tin and structures and devices including the films," US Patent App. 13/966,782, 2013.

[45] Y. J. Cho, C. H. Kim, H. S. Im, Y. Myung, H. S. Kim, S. H. Back, Y. R. Lim, C. S. Jung, D. M. Jang, J. Park, S. H. Lim, E. H. Cha, K. Y. Bae, M. S. Song and W. I. Cho, "Germanium-tin alloy nanocrystals for high-performance lithium ion batteries," *Phys. Chem. Chem. Phys.,* vol. 15, pp. 11691-11695, 2013.

[46] R. F. Spohn and C. B. Richenberg, "Tin Deuteride (SnD_4) Stabilization," *ECS Transactions,* vol. 50, pp. 921-927, 2013.

[47] K. Annamalai, I. K. Puri and M. A. Jog, *Advanced Thermodynamics Engineering.* CRC Press, 2010.

[48] B. R. Munson, D. F. Young and T. H. Okiishi, *Fundamentals of Fluid Mechanics.* New York, 1990.

[49] *Epsilon 2000 RPCVD reactor*. Available: http://www.asm.com/solutions/products/epitaxy-products/epsilon-epitaxy. Date accessed: 10/02/2015

[50] K. Rim, J. L. Hoyt and J. F. Gibbons, "Fabrication and analysis of deep submicron strained-Si n-MOSFET's," *Electron Devices, IEEE Transactions on,* vol. 47, pp. 1406-1415, 2000.

[51] R. Shimokawa, M. Yamanaka and I. Sakata, "Very low temperature epitaxial growth of silicon films for solar cells," *Japanese Journal of Applied Physics,* vol. 46, pp. 7612, 2007.

[52] M. Labrune, X. Bril, G. Patriarche, L. Largeau, O. Mauguin and P. R. i Cabarrocas, "Epitaxial growth of silicon and germanium on (100)-oriented crystalline substrates by RF PECVD at 175° C," *EPJ Photovoltaics,* vol. 3, pp. 30303, 2012.

[53] A. Matsuda, "Plasma CVD Processes for Thin Film Silicon Solar Cells," *Advanced Plasma Technology,* pp. 197-210, 2008.

[54] K. R. Bray, A. Gupta and G. N. Parsons, "Effect of hydrogen on adsorbed precursor diffusion kinetics during hydrogenated amorphous silicon deposition," *Appl. Phys. Lett.,* vol. 80, pp. 2356, 2002.

[55] C. Rosenblad, H. Deller, A. Dommann, T. Meyer, P. Schroeter and H. Von Kaenel, "Silicon epitaxy by low-energy plasma enhanced chemical vapor deposition," *Journal of Vacuum Science & Technology A: Vacuum, Surfaces, and Films,* vol. 16, pp. 2785, 1998.

[56] P. Gupta, V. Colvin and S. George, "Hydrogen desorption kinetics from monohydride and dihydride species on silicon surfaces," *Physical Review B,* vol. 37, pp. 8234-8243, 1988.

[57] M. C. Flowers, N. B. H. Jonathan, Y. Liu and A. Morris, "Temperature programmed desorption of molecular hydrogen from a Si (100)-2× 1 surface: Theory and experiment," *J. Chem. Phys.,* vol. 99, pp. 7038, 1993.

[58] Y. Chabal and K. Raghavachari, "New ordered structure for the H-saturated Si (100) surface: the (3× 1) phase," *Phys. Rev. Lett.,* vol. 54, pp. 1055-1058, 1985.

[59] A. Gupta, H. Yang and G. Parsons, "Ab initio analysis of silyl precursor physisorption and hydrogen abstraction during low temperature silicon deposition," *Surf. Sci.,* vol. 496, pp. 307-317, 2002.

[60] C. Tsai, G. Anderson, R. Thompson and B. Wacker, "Control of silicon network structure in plasma deposition," *J. Non Cryst. Solids,* vol. 114, pp. 151-153, 1989.

[61] S. Cereda, F. Zipoli, M. Bernasconi, L. Miglio and F. Montalenti, "Thermal-hydrogen promoted selective desorption and enhanced mobility of adsorbed radicals in silicon film growth," *Phys. Rev. Lett.,* vol. 100, pp. 46105, 2008.

[62] S. Heun, J. Falta and M. Henzler, "The initial stages of epitaxial growth of silicon on Si (100)− 2× 1," *Surf. Sci.,* vol. 243, pp. 132-140, 1991.

[63] C. W. Teplin, E. Iwaniczko, B. To, H. Moutinho, P. Stradins and H. M. Branz, "Breakdown physics of low-temperature silicon epitaxy grown from silane radicals," *Physical Review B,* vol. 74, pp. 235428, 2006.

[64] Y. S. Kim and K. Chang, "Structural transformation in the formation of H-induced (111) platelets in Si," *Phys. Rev. Lett.,* vol. 86, pp. 1773-1776, 2001.

[65] G. G. DeLeo, M. J. Dorogi and W. B. Fowler, "Bond-centered interstitial hydrogen in silicon: Semiempirical electronic-structure calculations," *Physical Review B,* vol. 38, pp. 7520, 1988.

[66] R. Lieten, J. McCallum and B. Johnson, "Single crystalline SiGe layers on Si by solid phase epitaxy," *J. Cryst. Growth,* vol. 416, pp. 34-40, 2015.

[67] V. Sivadasan, M. Myronov, S. Rhead, J. Halpin and D. Leadley, "Reverse terrace graded $Si_{1-x}Ge_x$/Ge/Si (001) virtual substrates grown using RP-CVD on on-axis and 6° off-axis substrates for future developments in III-V materials integration," in *Ultimate Integration on Silicon (EUROSOI-ULIS), 2015 Joint International EUROSOI Workshop and International Conference,* pp. 173-176, 2015.

[68] K. W. Shin, S. H. Park, Y. Park and E. Yoon, "Growth of High Quality Ge Layer on Silica Nano-Spheres Integrated Ge/Si Template Using UHV-CVD," *ECS Journal of Solid State Science and Technology,* vol. 4, pp. P83-P85, 2015.

[69] J. Werner, K. Lyutovich and C. Parry, "Defect imaging in ultra-thin SiGe (100) strain relaxed buffers," *The European Physical Journal Applied Physics,* vol. 27, pp. 367-370, 2004.

[70] J. Kouvetakis and A. V. G. Chizmeshya, "New classes of Si-based photonic materials and device architectures via designer molecular routes," *Journal of Materials Chemistry,* vol. 17, pp. 1649-1655, 2007.

[71] R. Beeler, R. Roucka, A. Chizmeshya, J. Kouvetakis and J. Menéndez, "Nonlinear structure-composition relationships in the $Ge_{1-y}Sn_y$ /Si (100)($y< 0.15$) system," *Physical Review B,* vol. 84, pp. 035204, 2011.

[72] P. Moontragoon, R. Soref and Z. Ikonic, "The direct and indirect bandgaps of unstrained $Si_xGe_{1-x-y}Sn_y$ and their photonic device applications," *J. Appl. Phys.*, vol. 112, pp. 073106-073106-8, 2012.

[73] A. Mosleh, S. A. Ghetmiri, B. R. Conley, M. Hawkridge, M. Benamara, A. Nazzal, J. Tolle, S. Yu and H. A. Naseem, "Material Characterization of $Ge_{1-x}Sn_x$ Alloys Grown by a Commercial CVD System for Optoelectronic Device Applications," *J Electron Mater*, vol. 43, pp. 938-946, 2014.

[74] B. R. Conley, A. Mosleh, S. A. Ghetmiri, W. Du, R. A. Soref, G. Sun, J. Margetis, J. Tolle, H. A. Naseem and S. Yu, "Temperature dependent spectral response and detectivity of GeSn photoconductors on silicon for short wave infrared detection," *Optics Express*, vol. 22, pp. 15639-15652, 2014.

[75] Y Bogumilowicz, J M Hartmann, R Truche, Y Campidelli, G Rolland and T.Billon, "Chemical vapour etching of Si, SiGe and Ge with HCl; applications to the formation of thin relaxed SiGe buffers and to the revelation of threading dislocations," *Semiconductor Science and Technology*, vol. 20, pp. 127, 2005.

[76] R. Cheng, W. Wang, X. Gong, L. Sun, P. Guo, H. Hu, Z. Shen, G. Han and Y. Yeo, "Relaxed and Strained Patterned Germanium-Tin Structures: A Raman Scattering Study," *ECS Journal of Solid State Science and Technology*, vol. 2, pp. P138-P145, 2013.

[77] J. Margetis, S. A. Ghetmiri, W. Du, B. R. Conley, A. Mosleh, R. Soref, G. Sun, L. Domulevicz, H. A. Naseem and S. Yu, "Growth and characterization of epitaxial $Ge_{1-X}Sn_x$ alloys and heterostructures using a commercial CVD system," in *ECS transaction*, pp. 1830-1830, 2014.

[78] B. R. Conley, A. Mosleh, S. A. Ghetmiri, W. Du, G. Sun, R. Soref, J. Margetis, J. Tolle, H. A. Naseem and S. Yu, "Stability of pseudomorphic and compressively strained $Ge_{1-X}Sn_x$ thin films under rapid thermal annealing," in *ECS transaction*, pp. 1844-1844, 2014.

[79] J. Matthews and A. Blakeslee, "Defects in epitaxial multilayers: I. Misfit dislocations," *J. Cryst. Growth*, vol. 27, pp. 118-125, 1974.

[80] R. People and J. Bean, "Calculation of critical layer thickness versus lattice mismatch for GeSi/Si strained-layer heterostructures," *Appl. Phys. Lett.*, vol. 47, pp. 322, 1985.

[81] Y. H. Jo, I. Jung, C. S. Choi, I. Kim and H. M. Lee, "Synthesis and characterization of low temperature Sn nanoparticles for the fabrication of highly conductive ink," *Nanotechnology*, vol. 22, pp. 225701, 2011.

[82] L. M. Giovane, H. Luan, A. M. Agarwal and L. C. Kimerling, "Correlation between leakage current density and threading dislocation density in SiGe pin diodes grown on relaxed graded buffer layers," *Appl. Phys. Lett.*, vol. 78, pp. 541-543, 2001.

[83] J. Hartmann, J. Damlencourt, Y. Bogumilowicz, P. Holliger, G. Rolland and T. Billon, "Reduced pressure-chemical vapor deposition of intrinsic and doped Ge layers on Si (001) for microelectronics and optoelectronics purposes," *J. Cryst. Growth,* vol. 274, pp. 90-99, 2005.

[84] S. Mader, A. Blakeslee and J. Angilello, "The interpretation of dislocation contrast in x-ray topographs of $GaAs_{1-x}P_x$," *J. Appl. Phys.*, vol. 45, pp. 4730-4734, 1974.

[85] J. Hornstra, "Dislocations in the diamond lattice," *Journal of Physics and Chemistry of Solids,* vol. 5, pp. 129-141, 1958.

[86] A. Bourret, J. Desseaux and A. Renault, "Core structure of the Lomer dislocation in germanium and silicon," *Philos. Mag. A,* vol. 45, pp. 1-20, 1982.

[87] A. Nandedkar and J. Narayan, "Atomic structure of dislocations in silicon, germanium and diamond," *Philos. Mag. A,* vol. 61, pp. 873-891, 1990.

[88] J. Kouvetakis and A. V. G. Chizmeshya, "New classes of Si-based photonic materials and device architectures via designer molecular routes," *Journal of Materials Chemistry,* vol. 17, pp. 1649-1655, 2007.

[89] S. Gupta, B. Magyari-Köpe, Y. Nishi and K. C. Saraswat, "Achieving direct band gap in germanium through integration of Sn alloying and external strain," *J. Appl. Phys.,* vol. 113, pp. 073707, 2013.

[90] R. Roucka, Y. Fang, J. Kouvetakis, A. Chizmeshya and J. Menéndez, "Thermal expansivity of $Ge_{1-y}Sn_y$ alloys," *Physical Review B,* vol. 81, pp. 245214, 2010.

[91] H. Li, Y. Cui, K. Wu, W. Tseng, H. Cheng and H. Chen, "Strain relaxation and Sn segregation in GeSn epi-layer s under thermal treatment," *Appl. Phys. Lett.,* vol. 102, pp. 251907, 2013.

[92] D. Eaglesham, G. Higashi and M. Cerullo, "370° C clean for Si molecular beam epitaxy using a HF dip," *Appl. Phys. Lett.,* vol. 59, pp. 685-687, 1991.

Appendix A: Description of Research for Popular Publication

We are living in the information age in which computers and digital devices have changed all aspects of traditional life such as communication. Microelectronics companies have tried to make their devices available to all the people by reducing their production costs and increasing the efficiency of the devices. This effort has resulted in a digital revolution in the world where people's needs are met largely by using electronic devices. Additionally, ccommunication in the modern world is almost impossible without using current digital technology. In order to enhance the communication speed, new materials need to be developed for a data communication in the computer systems.

Currently, optical communication is well established for long distance data transfer but the same technology should be incorporated inside the computer chips to increase the data transfer speed. Wire connection is still in use for connecting the devices on the chip which limits the speed and volume of the transferred data. Optical interconnects are designed to be used as superhighways that can replace long connections on the chip. Increasing the data transfer speed on the chip results in achieving lower data processing time and, subsequently, smaller and cheaper devices. In order to be able to transfer data on the chip, electronic signals need to be transformed to optical by using modulators, then sent through lasers, transferred by waveguides, and received by photodetectors. Developing a material that can be used for all these devices and still be compatible with silicon CMOS technology is challenging. Additionally, the material should be low cost so that it could win the price competition in industry.

Silicon-germanium-tin is a material system that enables fabrication of lasers, detectors, and waveguides needed for sending and receiving data on a chip. However, low cost production

of Si-Ge-Sn alloys is a challenge due to instability of Sn precursors. Researchers at the University of Arkansas have developed new methods for low cost production of these materials that are industrially scalable. A custom designed chemical vapor deposition system was built that can use low cost commercially available gases for the growth of Si-Ge-Sn alloys. Despite the challenges for incorporation of Sn in Ge and SiGe films, Mosleh et al. have been able to grow films that have up to 7% Sn and 17% Si. "This is the first time GeSn and SiGeSn was deposited directly on Si using all commercial gas precursors," said Mr. Mosleh. These results are very promising for the growth of device structures such as lasers and photo detectors. Dr. Naseem and Mr. Mosleh have patented their exceptional results which could lead to a big change in the future of Si technology. In the next stage of the research, higher Sn incorporation as well as higher material quality are targeted.

Appendix B: Executive Summary of Newly Created Intellectual Property

1. Low temperature growth of Si at 250 °C
2. Direct growth of GeSn and SiGeSn films on Si substrates using commercially available gases of silane, germane, and stannic chloride
3. Buffer-free growth of GeSn and SiGeSn films using in-situ gas mixing of deuterated stannane with commercial precursors.

Appendix C: Potential Patent and Commercialization Aspects of Listed Intellectual Property Items

C. 1 Patentability of Intellectual Property (Could Each Item be Patented)

The three items listed were considered first from the perspective of whether or not the item could be patented.

1. The measured value for the low temperature Si growth could not be patented
2. The method for growing GeSn and SiGeSn directly on Si without buffer layer is patentable.
3. The method for growing GeSn and SiGeSn using SnD_4 is patentable

C. 2 Commercialization Prospects (Should Each Item Be Patented)

The three items listed were then considered from the perspective of whether or not the item should be patented.

1. Not applicable
2. A provisional patent has been filed on Dec. 30, 2014 for this patent: Application number: 62097914.
3. An invention disclosure was filed with the technology licence office but the inventors decided to withdraw as the intellectual merit for this invention was not satisfying.

C. 3 Possible Prior Disclosure of IP

The following items were discussed in a public forum or have published information that could impact the patentability of the listed IP.

1. Not applicable
2. Not applicable
3. Not applicable

Appendix D: Broader Impact of Research

D. 1 Applicability of Research Methods to Other Problems

The methods that were used for the growth of Si-Ge-Sn materials could be applied for different gas precursors and films. Handling of each gas might be different but the delivery methods are similar and could be applied in different research areas. Growth methods that were used in this research are similar to the current growth methods that are used in industry and other research groups. Therefore, different composition of materials that have a gaseous precursor could be grown on different substrates. However, the process for each deposition needs optimization of precursors and carrier gases flow rates and deposition temperature.

D. 2 Impact of Research Results on U.S. and Global Society

Currently, optical data transfer technology is being used for data transfer between computer racks in data centers in the US and globally. This technology needs further enhancement by having data transfer between the chips and on the chip. This is possible using materials that can efficiently emit and detect light. The method proposed for the growth of Si-Ge-Sn can significantly change the industry to move towards low cost production of the material and subsequently fabrication of the required devices.

D. 3 Impact of Research Results on the Environment

Incorporation of GeSn alloys in Si technology increases the efficiency of the electronic devices. Such increase in the efficiency reduces the power consumption which directly affects the usage of fossil fuels that pollute the environment. Therefore, this research could have a

positive impact on saving the environment from excessive use of fossil fuels which causes global warming.

Appendix E: Microsoft Project for MS MicroEP Degree Plan

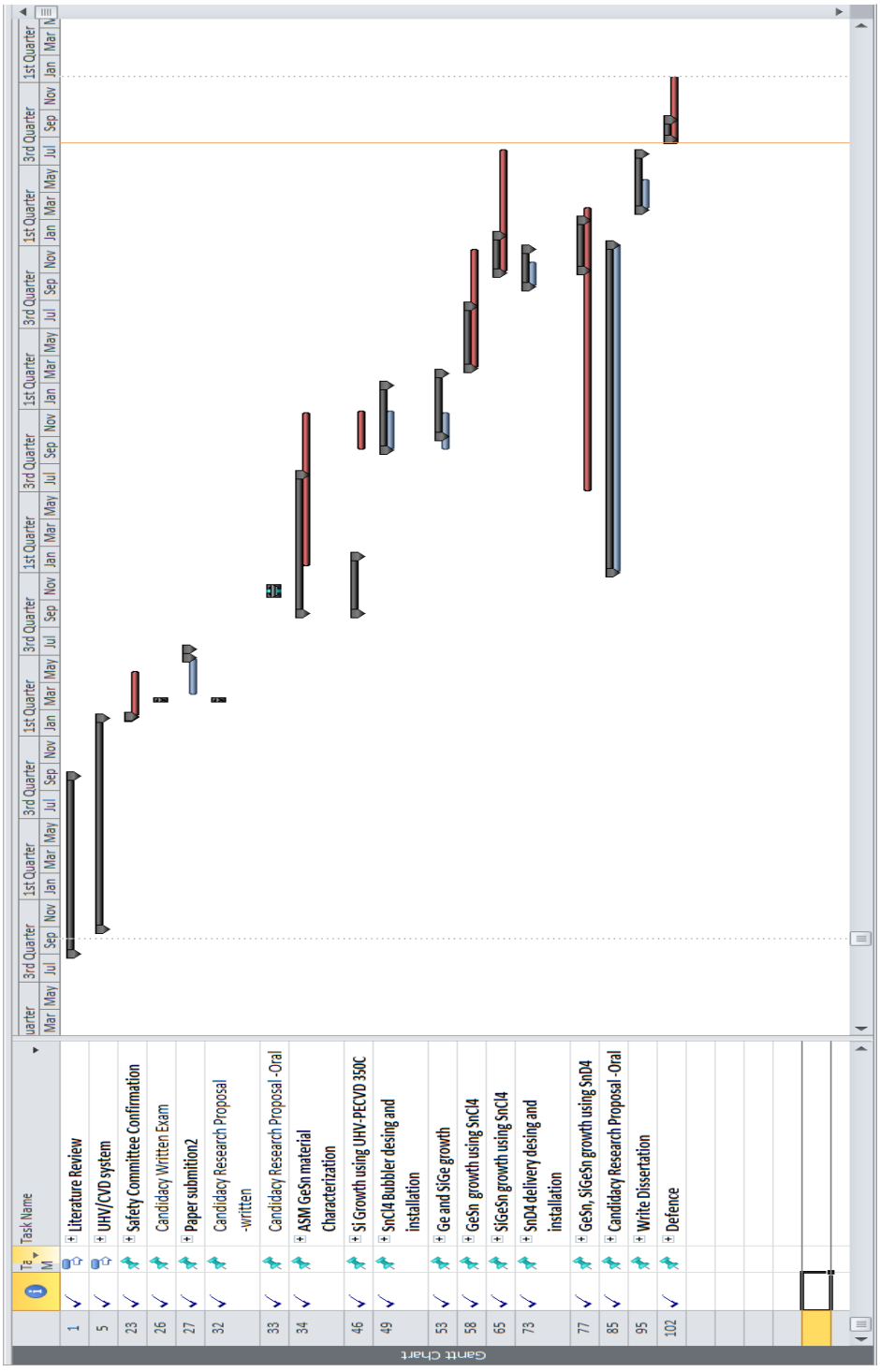

Appendix F: Identification of All Software Used in Research and Dissertation Generation

Computer #1:
- Model Number: Vaio SVS131
- Serial Number: 535148950700037
- Location: Personal laptop
- Owner: Aboozar Mosleh

Software #1:
- Name: Microsoft Office 2010
- Purchased by: Aboozar Mosleh

Software #2:
- Name: Microsoft Project 2010
- Purchased by: MSDN Academy Alliance through Engineering

Software #3:
- Name: Write-N-Cite III
- Purchased by: Free download available from RefWorks.com, activated by uark student account

Computer #2:
- Model Number: Corsair
- Serial Number: Gigabyte – 1/H/CGC22900355
- Location: ENRC Room 2993
- Owner: Dr. Shui-Qing Yu

Software #1:
- Name: OriginLab 9
- Purchased by: Dr. Shui-Qing Yu

Appendix G: All Publications Published, Submitted and Planned

G. 1 List of peer reviewed published works

1) "Enhancement of Material Quality of (Si)GeSn Films Grown By $SnCl_4$ Precursor," **A. Mosleh**, M. Alher, L. Cousar, H. Abu-safe, W. Dou, P. C. Grant, S. Al-Kabi, S.A. Ghetmiri, B. Alharthi, H. Tran, W. Du, M. Benamara, B. Lid, M. Mortazavi, S.-Q. Yu, H. Naseem, ECS Transactions, 2015. (in press)

2) "CMOS Compatible Growth of High Quality Ge, SiGe and SiGeSn for Photonic Device Applications," M. Alher, **A. Mosleh**, L. Cousar, W. Dou, P. C. Grant, S.A. Ghetmiri, S. Al-Kabi, W. Du, M. Benamara, B. Li, M. Mortazavi, S.-Q. Yu, H. A. Naseem, ECS Transactions, 2015. (in press)

3) "Direct growth of $Ge_{1-x}Sn_x$ films on Si using a cold-wall ultra-high vacuum chemical vapor deposition system," **A. Mosleh**, M. A. Alher, L. Cousar, W. Du, S.A. Ghetmiri, T. Pham, G. Sun, R.A. Soref, B. Li, , H.A. Naseem, S. Yu, , Frontiers in Materials, 2, 30, 2015.

4) "Si based GeSn photoconductors with a 1.63 A/W peak responsivity and a 2.4 μm long-wavelength cutoff," B. R. Conley, J Margetis, W. Du, H. Tran, **A. Mosleh**, S. A. Ghetmiri, J. Tolle, G. Sun, R. Soref, B. Li, H. A. Naseem, and S.-Q. Yu, Applied Physics Letters, 105, 221117, 2014.

5) "Direct-bandgap GeSn grown on Silicon with 2230 nm photoluminescence," S.A. Ghetmiri, W. Du, J. Margetis, **A. Mosleh**, L. Cousar, B.R. Conley, L. Domulevicz, A. Nazzal, G. Sun, R.A. Soref, J. Tolle, B. Li, H.A. Naseem, S. Yu, , Applied Physics Letters, 105, 151109, 2014.

6) "Shortwave-infrared photoluminescence from $Ge_{1-x}Sn_x$ thin films on silicon," S.A. Ghetmiri, W. Du, B.R. Conley, **A. Mosleh**, A. Nazzal, G. Sun, R.A. Soref, J. Margetis, J. Tolle, H.A. Naseem, S. Yu, Journal of Vacuum Science & Technology B. 32, 06060, 2014.

7) "Temperature dependent spectral response and detectivity of GeSn photoconductors on silicon for short wave infrared detection," B. R. Conley, **A. Mosleh**, S. A. Ghetmiri, W. Du, R. A. Soref, G. Sun, J Margetis, J. Tolle, H. A. Naseem, and S.-Q. Yu. Optics Express 22, no. 13, 15639-15652, 2014.

8) "Growth and Characterization of Epitaxial $Ge_{1-x}Sn_x$ Alloys and Heterostructures Using a Commercial CVD System," J. Margetis, S. A. Ghetmiri, W. Du, B. R. Conley, **A. Mosleh**, R. A. Soref, G. Sun, L. Domulevicz, H. A. Naseem, S.-Q. Yu, and J. Tolle, ECS Transactions, 64 (6), 711-720, 2014.

9) "Stability of Pseudomorphic and Compressively Strained $Ge_{1-x}Sn_x$ Thin Films under Rapid Thermal Annealing," B. R. Conley, **A. Mosleh**, S. A. Ghetmiri, W. Du, G. Sun, R. A. Soref, J Margetis, J. Tolle, H. A. Naseem and S.-Q. Yu, ECS Transactions, 64 (6) 881-893, 2014.

10) "Investigation of Growth Mechanism and Role of H_2 in Very Low Temperature Si Epitaxy," **A. Mosleh**, S. A. Ghetmiri, B. R. Conley, H. Abu-safe, M. Benamara, Z. Waqar, S.-Q. Yu, H. A. Naseem, ECS Transactions, 64 (6), 967-975, 2014.

11) "Investigation on Formation and Propagation of Defects in Ge_{1-x} Sn_x Thin Films," **A. Mosleh**, M. Benamara, S. A. Ghetmiri, B. R. Conley, M. A. Alher, W. Du, G. Sun, R. A. Soref, J. Margetis, J. Tolle, S.-Q. Yu, and H. A. Naseem, ECS Transactions. 64, 895-901, 2014.

12) "Room-temperature electroluminescence from $Ge/Ge_{1-x}Sn_x/Ge$ diodes on Si substrates," Du, W., Yiyin Zhou, Seyed A. Ghetmiri, **A. Mosleh**, B. R. Conley, A. Nazzal, R. A. Soref et al. Applied Physics Letters 104, no. 24, 241110, 2014.

13) "Material characterization of $Ge_{1-x}Sn_x$ alloys using a commercial CVD system for Optoelectronic Device Applications," **A. Mosleh**, S. A. Ghetmiri, B. R. Conley, M. Hawkridge, M. Benamara, A. Nazzal, J. Tolle, S.-Q. (Fisher) Yu, H. A. Naseem, Conference on Lasers and electro-optics, J. Electronic Materials, 43.4 (2014): 938-946.

G. 2 List of conference proceedings and publications

14) "Temperature-dependent Characterization of G 0.94 Sn 0.06 Light-Emitting Diode Grown on Si via CVD," S.A. Ghetmiri, W. Du, Y. Zhou, J. Margetis, T. Pham, **A. Mosleh**, B. Conley, A. Nazzal, G. Sun, R. Soref, J. Tolle, H. Naseem, B. Li, S.-Q. Yu, CLEO: Applications and Technology, ATu1J. 6, 2015.

15) "Enhanced Responsivity up to 2.85 A/W of Si-based Ge 0.9 Sn 0.1 Photoconductors by Integration of Interdigitated Electrodes," T. Pham, B. Conley, J. Margetis, H. Tran, S. A. Ghetmiri, **A. Mosleh**, W. Du, G. Sun, R. Soref, J. Tolle, H. Naseem, B. Li, S.-Q. Yu, CLEO: Science and Innovations, STh1I. 7, 2015.

16) "Si based GeSn light emitter: mid-infrared device in Si photonics," S.-Q. Yu, S. A. Ghetmiri, W. Du, J. Margetis, Y. Zhou, **A. Mosleh**, A. Nazzal, G. Sun, R.A. Soref, J. Tolle, B. Li, and H. A. Naseem, SPIE Photonics West, February 7-12 , 2015.

17) "Temperature dependent study of Si based GeSn photoconductor," T. Pham, W. Du, J Margetis, S. A. Ghetmiri, **A. Mosleh**, G. Sun, R. A. Soref, J. Tolle, H. A. Naseem, B. Li, and S.-Q. Yu, SPIE Photonics West, February 7-12, 2015.

18) "Extended Infrared Absorption to 2.2 μm with $Ge_{1-x}Sn_x$ Photodetectors Grown on Silicon," B. R. Conley, Liang Huang, Sayed A. Ghetmiri, **A. Mosleh**, W. Du, G. Sun, R. Soref, J.

Tolle, H. A. Naseem, and S.-Q. Yu. In CLEO: Science and Innovations, SM2H-5. Optical Society of America, 2014.

19) "Investigation of Photoluminescence from $Ge_{1-x}Sn_x$: A CMOS-Compatible Material Grown on Si via CVD," W. Du, , Sayed A. Ghetmiri, **A. Mosleh**, B. R. Conley, Liang Huang, A. Nazzal, R. Soref et al. In CLEO: QELS_Fundamental Science, JW2A-57. Optical Society of America, 2014.

20) "Photoluminescence from GeSn/Ge Heterostructure Microdisks with 6% Sn Grown on Si via CVD," S. A. Ghetmiri, B. R. Conley, **A. Mosleh**, Liang Huang, W. Du, A. Nazzal, G. Sun et al. In CLEO: Applications and Technology, pp. AW1H-2. Optical Society of America, 2014.

21) "Strain Relaxation and Material Quality Improvement of Compressively Strained GeSn Epitaxial Films through a Cyclic Rapid Thermal Annealing Process,"**A. Mosleh**, S. A. Ghetmiri, B. R. Conley, W. Du; S.-Q. Yu, H. A. Naseem, R. A. Soref, G. Sun, J. Tolle, J. Margetis, Photonics Society Summer Topical Meeting Series, 2014 IEEE , vol., no., pp.221,222, 14-16 July 2014

22) "Temperature Dependent Spectral Response and Responsivity of GeSn Photoconductor on Si," B.R Conley, **A. Mosleh**, S.A. Ghetmiri, W. Du, H. A. Naseem, S.-Q. Yu, R.A Soref, G. Sun., J. Tolle, J Margetis, Photonics Society Summer Topical Meeting Series, 2014 IEEE , vol., no., pp.219,220, 14-16 July 2014

23) "Nucleation-step study of silicon homoepitaxy for low-temperature fabrication of solar cells," **A. Mosleh**, Z. Waqar, S.-Q. (Fisher) Yu, H. Abu-safe, S. A. Ghetmiri, B. R. Conley, M. Benamara, H. A. Naseem, Photovoltaic Specialists Conference (PVSC), *2013 IEEE 39th* , pp.2646,2650, 16-21 June 2013

24) Strain engineering of high quality CVD grown GeSn film for optoelectronic devices," **A. Mosleh**, S. A. Ghetmiri, B. R. Conley, S.-Q. (Fisher) Yu, H. A. Naseem, M. Benamara, J. Tolle, "55th Conference on Lasers and electro-optics, EMC 2013.

25) "CVD growth GeSn using large scale Si process for higher efficient multi-junction solar cells," B. R. Conley, **A. Mosleh**, S. A. Ghetmiri, H. A. Naseem, J. Tolle, S.-Q. (Fisher) Yu. 39th IEEE Photovoltaic Specialists Conference, PVSC 2013.

26) "Safety Considerations in Building Ultra-High Vacuum Plasma Enhanced Chemical Vapor Deposition System for Low Temperature Group IV Epitaxy," H. Naseem, S.-Q. Yu, S. El-Ghazaly, Z. Waqar, H. Abu-Safe, S. Adcock, B. Conley, **A. Mosleh**, B. Hankton, A. Munasinghe, 19th Biennial University/Government/Industry, Micro/Nano Symposium (UGIM), 1, 1, 9-10 July 2012

G. 3 List of submitted works

27) "$Si_yGe_{1-x-y}Sn_x$ films grown on Si using a cold-wall ultra-high-vacuum chemical-vapor-deposition system," **Aboozar Mosleh**, Murtadha Alher, Wei Du, Larry C. Cousar, Seyed Amir Ghetmiri, Sattar Al-Kabi, Wei Dou, Perry C. Grant, Greg Sun, Richard A. Soref, Baohua Li, Hameed A. Naseem, Shui-Qing Yu, submitted to Journal of Vacuum Science and Technology B, 2015

28) "Buffer-free GeSn and SiGeSn growth on Si substrate using in-situ SnD_4 gas mixing," **Aboozar Mosleh**, Murtadha Alher, Wei Du, Larry C. Cousar, Seyed Amir Ghetmiri, Sattar Al-Kabi, Wei Dou, Perry C. Grant, Greg Sun, Richard A. Soref, Baohua Li, Hameed A. Naseem, Shui-Qing Yu, submitted to Journal of Electronic Materials, 2015

29) "Optical characterization of Si-based $Ge_{1-x}Sn_x$ alloys with Sn compositions up to 12%," Sattar Al-Kabi, Seyed Amir Ghetmiri, Joe Margetis, Wei Du, **Aboozar Mosleh**, Murtadha Alher, Wei Dou, Greg Sun, Richard A. Soref, John Tolle, Baohua Li, Mansour Mortazavi, Hameed A. Naseem, Shui-Qing Yu, submitted to Journal of Electronic Materials, 2015

G. 4 List of applied patent

30) "Heteroepitaxial growth of Ge-Sn alloys," **A. Mosleh**, S-Q Yu, H. A. Naseem, M. A. Alher and L. Cousar, US patent application number: 62097914, Dec 2014.

Appendix H: Sample preparation procedure

Germanium-tin films were grown on 4" (001) p-type Si substrates with 5-10 Ω·cm resistivity. Prior to loading the samples, they were cleaned in a two-step process: 1. piranha etch solution [H_2SO_4:H_2O_2 (1:1)], 2. oxide strip HF dipping [H_2O:HF (10:1) using 48% pure HF] followed by nitrogen blow drying. The final oxide strip step was not followed by a water rinse as it reduces the life-time of hydrogen passivation and exposes the surface to ambient oxygen.

Silicon crystallizes in the diamond lattice structure where each atom has four nearest neighbors. For a clean (unpassivated) (100) silicon surface, the surface silicon atoms are left with two dangling bonds. The surface reconstructs itself into a lower energy structure which is different from the bulk. Reconstruction changes the position of the atoms up to five layers and the surface forms what is called a 2×1 periodic structure (Figure H.1). In this reconstruction, two surface atoms with two dangling bonds come closer to form a bond and leave the other bond dangling. This process is called dimerization. Hydrogen terminates these dimers and makes a monohydride surface.

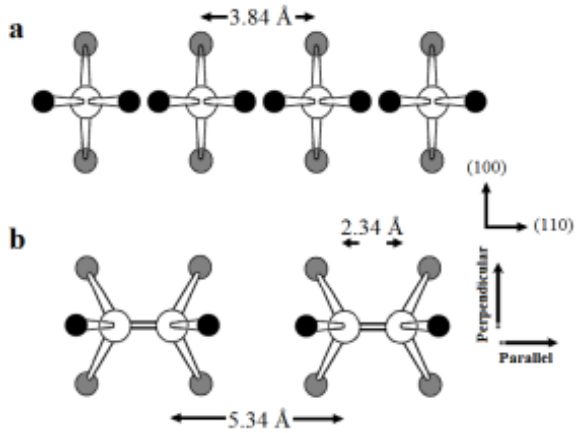

Figure H.1. Top view of Hydrogen passivated Si (100) surface. a) (1×1) surface (unreconstructed). (b) Dimers are formed on the surface to make a (2×1) reconstruction.

Surface reconstruction is different at different temperatures. At temperatures above 407 °C the surface is monohydride, while below this temperature it is partially dihydride. A 1×1 surface reconstruction allows two hydrogen atoms to be bonded to the surface Si atoms. It has been reported that epi-layer growth requires a temperature >370°C [92] as around 407°C most of the dihydride on HF dipped surfaces are converted to monohydride by H_2 desorption

Figure H.1 shows pathways of diffusion parallel and perpendicular to the dimer on a 2×1 Si (100) surface. The activation energy for diffusion parallel to the dimer is different from perpendicular diffusion. Activation energies for Si ad-atom diffusion on a bare Si (100) 2×1 surface are 0.6 eV and 1 eV for parallel and perpendicular to dimer rows, respectively. However, it is increased to 1.5 and 1.7 eV for parallel and perpendicular to dimer rows, respectively, for a monohydride surface.

The energy barrier caused by hydrogen passivation is of great importance as preparation plays a crucial role in the nucleation step needed for epitaxial growth. Therefore, capping Si dangling bonds with hydrogen (HF dipping) should be done with special care. Hydrogen passivated silicon surfaces can resist reaction with oxygen and water vapor for several minutes. However, it cannot resist this reaction for long as spectroscopic ellipsometry study of Si (100) shows 0.5 Å of oxide is grown on hydrogen-terminated Si (100) surface after 20 min. Also, having a hydrophobic surface is not a true indicator of an oxide-free surface because the oxidation mechanism starts with oxidizing the Si back bonds while keeping the surface hydrogen-terminated. This process accelerates in the presence of water. Therefore, rinsing a hydrogen passivated surface after HF dipping oxidizes the surface faster. This is the reason HF dipped hydrogen-passivated samples are blow-dried with nitrogen rather than rinsed in water.